EMPIRICAL MODELLING OF THE SOLAR WIND INFLUENCE ON PC3 PULSATION ACTIVITY

A thesis submitted in fulfilment of

the requirements for the degree of

DOCTOR OF PHILOSOPHY

---

of

RHODES UNIVERSITY

---

by

Stefanus Ignatius Lotz

March 2012

Abstract

Geomagnetic pulsations are ultra-low frequency (ULF) oscillations of the geomagnetic field that have been observed in the magnetosphere and on the Earth since the 1800's. In the 1960's in situ observations of the solar wind suggested that the source of pulsation activity must lie beyond the magnetosphere. In this work the influence of several solar wind plasma and interplanetary magnetic field (IMF) parameters on Pc3 pulsations are studied. Pc3 pulsations are a class of geomagnetic pulsations with frequency ranging between 22 and 100 mHz. A large dataset of solar wind and pulsation measurements is employed to develop two empirical models capable of predicting the Pc3 index (an indication of Pc3 intensity) at one hour and five minute time resolution, respectively. The models are based on artificial neural networks, due to their ability to model highly non-linear interactions between dependent and independent variables. A robust, iterative process is followed to find and rank the set of solar wind input parameters that optimally predict Pc3 activity. According to the parameter selection process the input parameters to the low resolution model (1 hour data) are, in order of importance, solar wind speed, a pair of time-based parameters, dynamic solar wind pressure, and the IMF orientation with respect to the Sun-Earth line (i.e. the cone angle). Input parameters to the high resolution model (5 minute data) are solar wind speed, cone angle, solar wind density and a pair of time-based parameters. Both models accurately predict Pc3 intensity from unseen solar wind data. It is observed that Pc3 activity ceases when the density in the solar wind is very low, even while other conditions are favourable for the generation and propagation of ULF waves. The influence that solar wind density has on Pc3 activity is studied by analysing six years of solar wind and Pc3 measurements at one minute resolution. It is suggested that the pause in Pc3 activity occurs due to two reasons: Firstly, the ULF waves that are generated in the region upstream of the bow shock does not grow efficiently if the solar wind density is very low; and secondly, waves that are generated cannot be convected into the magnetosphere because of the low Mach number of the solar wind plasma due to the decreased density.

Acknowledgements

I appreciate the guidance and patience of my supervisors, Dr. Lee-Anne McKinnell and Prof. Peter Sutcliffe. The useful discussions on data analysis with Dr. Andrew Collier and Dr. Pierre Cilliers is greatly appreciated.

Thank you to the entire South African National Space Agency (SANSA) staff in Hermanus. It was a pleasure to work with everyone.

Financial support from the National Astrophysics and Space Science Programme (NASSP), the National Research Foundation (NRF) and SANSA made my postgraduate studies possible. I am thankful for the financial support by the NRF and the Hungarian Space and Technology Foundation that enabled the collaboration with the Eötvös Loránd Geophysical Institute in Tihany, Hungary. I would like to thank Balázs Heilig for the useful collaboration, advice, and his hospitality in Tihany.

I am very grateful to Drs. Habarulema, Sibanda and Ndiitwani for the motivation, advice, and the example set to me and the rest of the SANSA students. To Chigo and Jean, my fellows in this marathon – thank you for the support and discussions on everything from politics to braai techniques over the years.

Thank you to my family and friends for all the support and prayer over the years. I am grateful to everyone for sticking it out with me. Gen. 17:1 "Ek is God die almagtige; lewe naby My en wees opreg."

Publications from this Thesis

One paper was published from the work contained in this thesis.

Empirically modelled Pc3 activity based on solar wind parameters **(2010), B. Heilig, S. Lotz, J. Verö, P. Sutcliffe, J. Reda, K. Pajunpaä, and T. Raita, Annales Geophysicae, 28, pg. 1703 – 1722.**

In this paper Pc3 pulsation activity was empirically modelled using measurements of solar wind plasma and the interplanetary magnetic field. The lead author is B. Heilig, from the Eötvös Loránd Geophysical Institute (ELGI), Hungary, and my co-supervisor, Prof. P. Sutcliffe is a co-author. In this paper a statistical analysis of Pc3 activity and solar wind parameters is made, and two empirical models (a multiple linear regression model and a neural network based model) are developed. My main contribution to this paper is contained in section 4.4 of this paper where the development of the neural network based model is discussed, but I was involved in the writing of most of the sections of this paper, and specifically the discussion (section 5) and conclusion (section 6).

Table of Contents

List of Tables

List of Figures

Chapter 1

Introduction

Geomagnetic pulsations are oscillations of the Earth's magnetic field that are observed on the surface of the Earth and in the magnetosphere. These oscillations occur in the ultra-low frequency (ULF) band, from about 1 mHz to 1 Hz. Two distinct classes of pulsations are identified, based on the shape of the oscillations, as either irregular (denoted Pi) or continuous (Pc). The two classes are further divided into characteristic frequency bands [Jacobs et al., 1964]. In this thesis the Pc3 class of geomagnetic pulsations, with frequency between 22 and 100 mHz, is studied.

The origin of Pc3 pulsations is believed to be in the region upstream of the Earth's magnetic field, where the solar wind plasma interacts with the bow shock wave created by the supersonic solar wind flow [e.g. McPherron, 2005]. Plasma instabilities are set up and ULF waves are generated upstream of the shock [e.g. Gary, 1991; Potapov and Mazur, 1994]. The ULF wave power is convected into the magnetosphere where coupling mechanisms transfer power to the ionosphere, perturbing the surface magnetic field, so that Pc3's are observed on the ground [e.g. McPherron, 2005]. Soon after in situ measurements of the solar wind became available in the 1960's, correlations between Pc3 pulsation activity and certain parameters of the solar wind plasma and the interplanetary magnetic field (IMF) were noticed. Saito [1964] first observed the positive correlation between the flow speed of the solar wind plasma and the amplitude of Pc3's in the magnetosphere. Soon after that a linear relationship between the frequency of the Pc3's and the magnitude of the IMF was noted by Bol'shakova and Troitskaya [1968]. Furthermore, it was noticed that Pc3's are preferentially observed if the orientation of the IMF is approximately aligned to the line connecting the Sun and the Earth [e.g. Kovner et al., 1976; Greenstadt and Olson, 1976]. Since then several studies of the solar wind influ-

ence on Pc3 activity confirmed these relationships [e.g. Wolfe et al., 1980; Le and Russell, 1992; Chi et al., 1998; Chugunova et al., 2007].

1.1 Problem Description and Goals

In this thesis a non-linear framework is employed to model the intensity of Pc3 pulsations on the ground, based solely on solar wind and time based input parameters (i.e. no internal magnetospheric parameters are used). Two regression models that are based on artificial neural networks (ANN's) are developed. This is the first time that neural networks are employed to predict Pc3 activity from solar wind data. Solar wind based parameters are the independent variables and the Pc3 pulsation index ($Pc3_{ind}$ – an indication of Pc3 intensity, defined in equation 4.6) is the dependent variable in the regression models. ANN's are non-linear information processing structures, capable of fault tolerance and generalisation to arbitrary values of input and output parameters [e.g. Müller and Reinhardt, 1996; Haykin, 1994]. The non-linear nature of ANN's enables the development of regression models that are capable of modelling the complex, non-linear relationships between extra-magnetospheric solar wind parameters and ground-based Pc3 activity.

ANN's are empirical models and the development of their predictive capability relies on the availability of large sets of historical input and output parameter measurements. Low resolution (1 hour averages) and high resolution (1 minute averages) measurements of solar wind data, collected by instruments on board several spacecraft located upstream of the Earth's magnetosphere, and geomagnetic field data are employed. Magnetometer measurements from Tihany, Hungary, are used to derive the pulsation index. The solar wind and Pc3 data sets employed span the interval from 2002 to 2007.

The specific goals of this study are to:

1. create a modelling framework capable of predicting pulsation activity from solar wind data;
2. determine which solar wind parameters drive pulsation activity;
3. infer the preferred generation mechanism of Pc3 pulsation activity.

1.2 Document Structure

This thesis consists of seven chapters. In the next chapter the mechanisms that give rise to the generation of Pc3 pulsations, from the formation of the solar wind to the perturbation of the geomagnetic field, are discussed. Chapter 3 describes neural networks and their application to regression problems. The structure of ANN's and the algorithms employed in the development of ANN based models are discussed. An example problem is presented to demonstrate the development of an ANN based regression model.

In this thesis two models that predict Pc3 pulsation activity, from parameters measured in the solar wind, are developed. A low resolution model, which employs hourly averaged data, is developed in Chapter 4. An iterative process is employed to select the set of solar wind based parameters that optimally reproduce the desired output (hourly $Pc3_{ind}$). In Chapter 5 a similar process is followed to select the solar wind parameters capable of predicting 5-minute running averages of 1-minute $Pc3_{ind}$ samples.

Chapter 6 specifically addresses the influence that solar wind density has on pulsation activity. A large dataset of one minute averages of solar wind and pulsation index measurements is employed to conduct a statistical analysis of the influence that the proton number density in the solar wind has on Pc3 activity. In the final section of Chapter 6 an analytical solution to the rate of wave growth upstream of the bow shock is used to explain the role that solar wind density plays in Pc3 generation. This thesis concludes with a summary of the work and a discussion of the outcomes and conclusions (Chapter 7).

Chapter 2

Pc3 Pulsations

Theoretical background information is presented in this chapter to aid the reader in following the analysis presented in this thesis. The main aim of the chapter is to provide a background setting on Pc3 pulsations that will aid clarity to this study. Although the explanations offered in this chapter are by no means complete, care has been taken to reference sources that provide ample material for further reading.

2.1 Introduction

> "The exertion of the disturbing force was thus of a throbbing or pulsatory character. The interval of time between two of these minute pulsations may be said to have varied from half a minute, or the smallest observable portion of time, up to four or five minutes."
>
> – Stewart [1861]

The paragraph above describes one of the first published observations of what is today known as geomagnetic ULF pulsations. These are oscillations of the geomagnetic field, observed in the magnetosphere and on the ground; they are the magnetic manifestations of magnetohydrodynamic (MHD) waves propagating in the magnetosphere. After the initial observations by Stewart [1861], as the practise of recording magnetic field measurements became widespread due to advances in observational techniques, different types of pulsations were identified. They were found to occur at discrete sets of frequencies, and were usually named after the first person to discover and characterise them [Hughes, 1994].

In 1963, an IAGA (International Association of Geomagnetism and Aeronomy) committee classified ULF pulsations into two classes according to waveform and further into subclasses by period. Table 2.1 lists the classification proposed by Jacobs et al. [1964]. Pulsations were classified as irregular (Pi) and continuous (Pc). The irregular class is defined by a broad-band power spectrum, i.e. significant power over a range of frequencies, whereas continuous pulsations exhibit fairly regular oscillations at a well-defined peak frequency [e.g.. Kivelson, 1995b]. Further divisions into frequency bands (Pi1, 2; Pc1–5) are based on the physical and morphological characteristics, but the authors [Jacobs et al., 1964] noted that their understanding is incomplete and that the division between classes may be adapted subject to new insight into pulsation activity becoming available. Although much progress in the study of pulsations and their generation mechanisms has subsequently been made – for example, it has been found that separate classes of pulsation may result from the same driving mechanism – the proposed terminology is still in use.

Table 2.1: Definitions of pulsations according to period, as proposed at the IAGA committee meeting in 1963 by Jacobs et al. [1964].

Name	Period [s]	Frequency [Hz]
Irregular		
Pi1	1 – 40	0.025 – 1
Pi2	40 – 150	0.002 – 0.025
Continuous		
Pc1	0.2 – 5	0.2 – 5
Pc2	5 – 10	0.1 – 0.2
Pc3	10 – 45	0.022 – 0.1
Pc4	45 – 150	0.007 – 0.022
Pc5	150 – 600	0.002 – 0.007

Pc3 pulsations are measured on the ground in the horizontal (H) component of the geomagnetic field. The H component forms part of the HDZ geomagnetic coordinate system. The H and D (declination) components are calculated from the X (positive geographic northward) and Y (positive geographic eastward) components, and Z is the vertical component pointing toward the centre of the Earth:

$$H = \sim X^2 + Y^2 \tag{2.1a}$$

$$D = \tan(X/Y) \tag{2.1b}$$

$$Z = Z. \tag{2.1c}$$

Figure 2.1 illustrates the difference between irregular and continuous pulsations. The upper panel shows a Pi2 event observed at Hermanus, South Africa (HER: 34.42^{0} S, 19.22^{0} E), on day 137 of 2002; in the lower panel a Pc3 event recorded at HER on day 49 of 2003 is plotted. In both cases, 1-second measurements of the horizontal (H) component of the geomagnetic field are used. The characteristics of these two types of pulsation are visible in the time series data: the irregular, impulsive nature of the Pi2 time series curve is clear compared to the regular, sinusoidal shape of the Pc3 curve. Pi2's are defined as irregular pulsations with characteristic period of 40 – 150 seconds, while Pc3's are continuous with 10 – 45 second periods (see Table 2.1). The higher frequency of the Pc3 oscillations, compared to the frequency of the Pi2 oscillations are clearly visible. The time at which the two events are observed reveal something about their respective generation mechanisms. The Pi2 event is observed near local midnight and the Pc3 event in the local afternoon sector (local time = UT + 2). Pi2's are related to substorm activity, are clear indicators of substorm onset [e.g.. Sutcliffe, 1997], and typically occur on the night side of the Earth, although they may be observed on the day side at low latitudes. Pc3 pulsations are usually observed on the day side and are driven by various processes related to the reaction of the day side magnetosphere to the incoming solar wind.

The generation of Pc3 pulsations may ultimately be traced back to the Sun and the solar wind. In the rest of this chapter the generation of Pc3 pulsations is presented by discussing the relevant physical processes from the Sun to the Earth.

2.2 The Sun and the Solar Wind

In astronomical terms the Sun is classified as a type G2V star, defining it as a "yellow dwarf" [e.g. Lang, 2001]. The Sun radiates energy through nuclear fusion reactions in its hot (1.56×10^{7} K), dense (1.513×10^{5} kg.m^{-3}) core where hydrogen is fused into helium. Lang [2001] provides an extensive overview of the Sun and most of the physical quantities listed in this section are found in this text. The core radiates energy outward through the radiative zone. At the outer edge of the radiative zone the temperature gradient – from $\sim 1.5 \times 10^{6}$ K at the edge to ~ 6000 K in the photosphere – is so large that a layer of turbulent convection is formed. The solar atmosphere consists of three layers – the photosphere, which is visible from Earth as the solar disc, the chromosphere and the corona. The temperature of the coronal gas ($\sim 10^{6}$ K) is several orders of magnitude higher than the other layers of the atmosphere ($\sim 10^{3}$ K). Coronal heating occurs primarily through the dissipation of energy released when oppositely

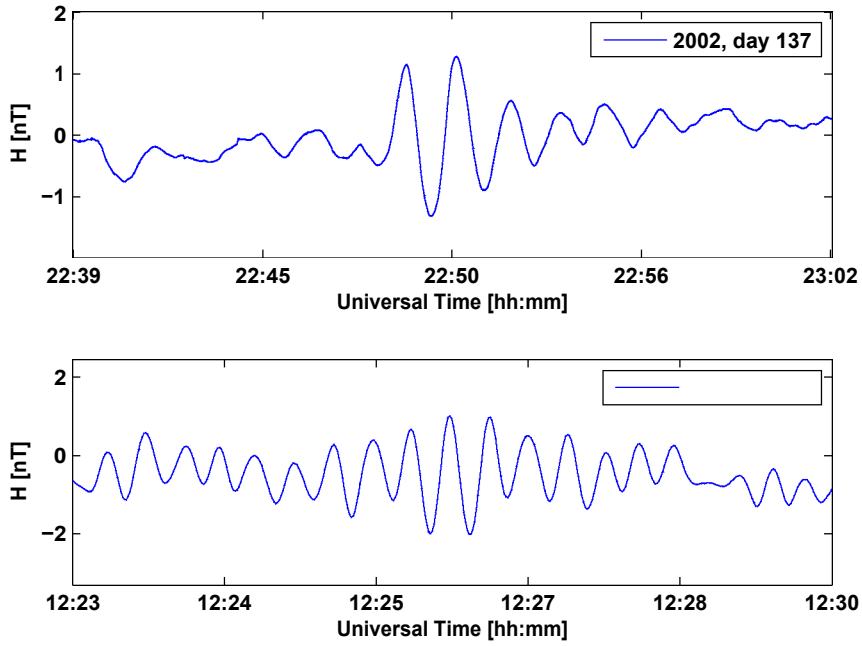

Figure 2.1: An irregular pulsation (Pi2) event observed on day 137 of 2002 and a continuous pulsation (Pc3) event observed on day 49 of 2003 at HER.

charged magnetic field lines in the corona break and reconnect [Lang, 2001]. Figure 2.2 is an illustrative diagram of the Sun, depicting the various solar phenomena discussed in the next paragraph.

Similar to the Earth, the Sun rotates in an anti-clockwise (west to east) direction about its axis. Its rotational period, however, is not constant. Due to its gaseous nature the Sun has a differential rotational period which increases with latitude from about 25.6 (Earth) days at 0° to about 33.4 days at 75°. The variation in rotational period and the conductive nature of the solar plasma enables the solar dynamo effect to amplify and sustain the solar magnetic field [Lang, 2001]. Due to differential rotation the Sun's dipole magnetic field is distorted as the highly conductive plasma in the equatorial region rotates faster than the plasma at higher latitudes. An initially poloidal (pole to pole orientation) configuration is displaced so that a toroidal component is created (see Figure 2.2). Field lines are stretched to form loops that extend beyond the photosphere into the corona, usually mirrored in the opposite (northern / southern) hemisphere due to the symmetry of the solar magnetic field (Figure 2.2). The regions on the photosphere where the field lines penetrate into the chromosphere and the

corona are cooler than the surrounding plasma and are visible as dark "sunspots" on the solar disk. The magnetic dynamo process that sustains the Sun's magnetic field is such that the field lines are wound up, as described, and relaxed in regular cycles of approximately 11 years. Increased magnetic activity around sunspots are known as active regions and are the location of massive outbursts of plasma and electromagnetic energy. The field line loops form flux tubes of plasma, releasing plasma and energy when field lines break and reconnect. The eruption of energy occurs throughout the electromagnetic spectrum and reaches the Earth in about 10 minutes, travelling at speed close to the speed of light. The distance from the Earth to the Sun is about 1.5×10^{8} km and is defined as 1 astronomical unit (1 AU). Along with the electromagnetic outburst, large volumes ($\sim 10^{13}$ kg [Hundhausen, 1995]) of hot coronal plasma are hurled from the active region. These coronal mass ejections (CME's) are not the only way the Sun ejects plasma into space. Due to the massive pressure difference between interplanetary space and the solar corona, $\sim 10^{-13}$ Pa in interplanetary space and $\sim 10^{-3}$ Pa in the corona [Hundhausen, 1995], the coronal gas is continuously emanating from the Sun in all directions, at an average speed of about 400 km.s^{-1}. The ambient outflow of the solar wind takes about four days to travel to the Earth's orbital path. Table 2.2 lists some characteristic solar quantities.

Table 2.2: Characteristic solar quantities. These numbers are also listed in Lang [2001] and Hundhausen [1995], as indicated.

Mass	$M_{\sim}$	$1.989 \times 10^{30}_{8}$ kg	[Lang, 2001]
Radius	$R_{\sim}$	$6.995 \times 10^{}_{11}$ m	[Lang, 2001]
Distance from Earth	1 AU	$1.495 \times 10^{}_{16}$ m	[Lang, 2001]
Pressure	centre	$2.334 \times 10^{}$ Pa	[Lang, 2001]
	photosphere	10 Pa	[Lang, 2001]
	corona	4×10^{-3} Pa	[Hundhausen, 1995]
	at 1 AU	30×10^{-12} Pa	[Hundhausen, 1995]
	interplanetary space	$\sim 10^{-13}$ Pa	[Hundhausen, 1995]

2.2.1 The Solar Wind

This natural, continuous outflow of the solar coronal plasma is known as the solar wind. The notion of a fast-flowing solar wind was not yet established in the 1950's; in fact, the outflow of coronal gas was believed to be transient – evidently only occurring in the time leading up to, and during, observable geomagnetic disturbances [Hundhausen, 1995]. Observations of zodiacal light scattering and the anti-sunward orientation of comet tails suggested the con-

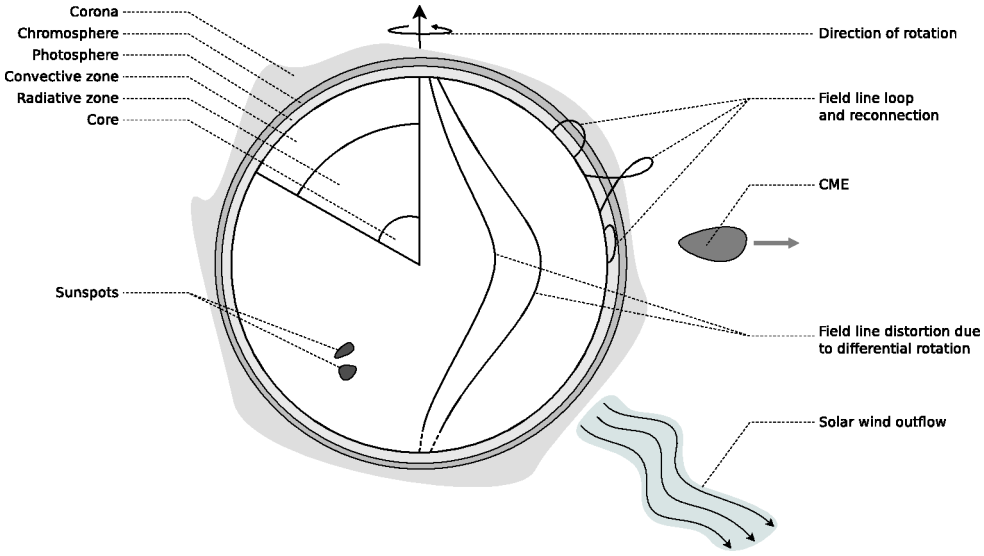

Figure 2.2: The Sun consists of a number of layers – from the core in the centre to the solar atmosphere (the corona). The dynamics of the solar magnetic activity drives several phenomena described in the text and depicted here.

tinuity of the solar wind [Lang, 2001]. It was Chapman [1957] who first studied the implications of the corona extending into interplanetary space [Hundhausen, 1972]. The model suggested that the corona should extend to large distances from the Sun, but the high densities estimated near Earth implied that the coronal plasma could not merge into the interstellar medium [Hundhausen, 1972]. Building on Chapman's work, Parker [1958] derived a model, from the fluid equation of motion, for the expansion of the corona into the supersonic solar wind at large distance r from the Sun. A so-called "structureless" solar wind is assumed, that is, a steady state (independent of time, $d/dt = 0$), spherically symmetric corona with radially outward flow, resulting in all parameters depending on radial distance from the Sun (r) but not on time. This yields the momentum equation

$$\rho u \frac{du}{dr} = \frac{dP}{dr} - \rho \frac{GM_\odot}{r^2} \tag{2.2}$$

with u the expansion speed, pressure P, mass density of the coronal plasma ρ, gravitational constant G and $M_\odot$ is the solar mass. Furthermore, the conservation of mass (i.e. the continuity equation)

$$\frac{1}{r^2}\frac{d}{dr}\left(r^2 \rho u\right) = 0 \tag{2.3}$$

is assumed. The model is simplified by assuming a neutral plasma (equal number n of electrons and protons) and constant temperature T, with $T - T_e = T_p$, yielding $\rho = n(m_e + m_p) \equiv n\,m$ and the ideal gas law $P = 2n\,k_B T$, with k_B Boltzmann's constant. These assumptions constitute an isothermal, static corona, and the momentum equation becomes

$$\frac{1}{u}\frac{du}{dr}\left(u^2 - \frac{2k_B T}{m}\right) = \frac{4k_B T}{m\,r} - \frac{GM_O}{r^2} \qquad (2.4)$$

Several solutions to this model indicate finite pressure at $r = \infty$, which would stop the coronal plasma from merging into the interplanetary background (which has pressure $P_{r\to\infty} \sim 10^{-14}$ Pa) [Hundhausen, 1995]. A solution with small u near the corona and $du/dr > 0$ yields zero pressure at $r = \infty$ and supersonic expansion at large r.

Parker's isothermal, supersonic solar wind model was vindicated by the early in situ observations that recorded supersonic solar wind flow near 1 AU. The first observations of the solar wind was made in the first decade of the space age by probes aboard the Luna 2 and 3 spacecraft, but it was during the Mariner 2 mission in 1962 that observations provided clear evidence of a supersonic solar wind – 124 days' of data yielded an average flow speed of 504 km.s^{-1}. The speed of sound waves ($V_s = \sqrt{\gamma P/\rho}$) in the solar wind near 1 AU is approximately 60 km.s^{-1} [Hundhausen, 1995], significantly smaller than the mean u observed by Mariner 2.

In the hydrodynamic approach followed by Parker [1958] the effect of the coronal magnetic field and the solar rotation is omitted. The high conductivity of the coronal plasma results in the coronal field embedded into the plasma and dragged out into space along with the expanding corona [Hundhausen, 1972]. The embedding of a magnetic field into a plasma parcel is understood through the "frozen-in flux" condition. Briefly, this concept dictates that magnetic flux through a parcel of plasma bounded by a surface remains constant even if that surface changes in shape and location with time, as would happen to a volume of solar wind plasma as it is transported through space by the coronal expansion. Walker [2005] and Kivelson [1995a], for example, provide more complete discussions of this concept. As the Sun rotates flux tubes of solar wind plasma defined by radial streamlines and cross-sectional area $A(r)$ spiral outward from the Sun. Due to the rotation the field emanating from the corona is

Table 2.3: Average solar wind quantities near 1 AU. These quantities are also listed in Hundhausen [1995].

Description	Symbol	Value
Proton density	N_p	6.6 cm^{-3}
Electron density	N_e	7.1 cm^{-3}
Flow speed	V_{sw}	450 $km.s^{-1}$
Proton temperature	T_p	1.2 x 10^5 K
Electron temperature	T_e	1.4 x 10^5 K
Magnetic field magnitude	B	7 nT

defined by radial (r) and azimuthal (ϕ) components [Hundhausen, 1995]

$$B_r = B_0 \left(\frac{R_O}{r}\right)^2 \tag{2.5a}$$

$$B_\phi = \frac{\omega_O r}{u} B_r \tag{2.5b}$$

where B_0 is the magnetic field magnitude at the solar radius and ω_O is the angular frequency of the solar rotation.

Due to its prevalence throughout interplanetary space the embedded field is known as the interplanetary magnetic field (IMF). As the coronal gas expands into space its characteristic properties change, as equations 2.5a and 2.5b demonstrate. The solar wind near the Earth is very different from the initially expanding coronal gas. Table 2.3 lists average properties of the solar wind near 1 AU [from Hundhausen, 1995]. The rotation of the Sun and the radial outflow of the solar wind shapes the frozen-in field lines into a spiral formation (the so-called Parker spiral). Under average solar wind conditions the radial and azimuthal components of the field are approximately equal, resulting in a nearly 45^0 angle between the IMF and the Sun-Earth line (at 1 AU).

2.3 Magnetohydrodynamics

Electromagnetic fields act on charged particles changing their motion and thus affecting the fluid properties of the plasma. Including electromagnetic effects in a hydrodynamic model forms the basis of magnetohydrodynamics (MHD) – the dynamics of a conductive fluid in the presence of electromagnetic fields [Walker, 2005]. Two interrelated forces exerted on the plasma are the force due to pressure gradients in the fluid and a magnetic force ($\mathbf{j} \times \mathbf{B}$, with $\mathbf{j}$ the current density) acting on a volume of current-carrying plasma in the presence of a magnetic

field **B**. Each force is related to a characteristic speed. The speed of sound waves in a plasma is determined by the pressure gradients and defined by

$$V_s = \sqrt{\frac{\gamma P}{\rho}} = \sqrt{\frac{\gamma k_B T}{m}} \tag{2.6}$$

with m the mass, γ polytropic index, and T the temperature. Waves propagating along the magnetic field, with perturbations perpendicular to the field, are known as transverse Alfvén waves [Walker, 2005, for example]. Analogous to the speed of sound, the speed at which these waves travel along field lines is

$$V_A = \sqrt{B^2/\mu_0 P} \tag{2.7}$$

with μ_0 the permeability of free space and B the magnetic field magnitude. Due to the relative motion of ions and electrons, the solar wind plasma will oscillate with a characteristic frequency. This is the plasma frequency (ω) and it is defined by

$$\omega = \frac{Ne^2}{\varepsilon_0 m_i} + \frac{Ne^2}{\varepsilon_0 m_e} \tag{2.8}$$

where ε_0 is the permittivity of free space, e is the elementary charge, and m_i and m_e are the ion and electron masses, respectively. Each of the terms above denotes the angular frequency of the harmonic motion generated by the restoring force when displacing the ions and electrons relative to each other. Since ions are heavier than electrons ($m_i \sim m_e$), the plasma frequency is largely determined by the electron term, i.e. $\omega \approx \frac{Ne^2}{\varepsilon_0 m_e}$.

In the presence of a magnetic field a force is exerted on charged particles causing rotational movement about the field line. The motion of a particle j with velocity $\mathbf{v}$ in the presence of a magnetic field **B** moving under the Lorentz force is determined by [e.g. Treumann and Baumjohann, 1997b]

$$m_j \frac{d}{dt}\mathbf{v} = q_j(\mathbf{v} \times \mathbf{B}) \tag{2.9}$$

with m_j and q_j the mass and (signed) charge of j. In an orthogonal coordinate system with $\mathbf{B} = B\hat{\mathbf{z}}$ the second order time derivatives of the velocity components yield

$$\frac{d^2}{dt^2} v_x = \left(\frac{q_j B}{m_j}\right)^2 v_x \tag{2.10}$$

$$\frac{d^2}{dt^2} v_y = \left(\frac{q_j B}{m_j}\right)^2 v_y. \tag{2.11}$$

Acceleration parallel to the field is constant, i.e. $d v_z/d t = 0$. The fraction is known as the gyro- or cyclotron frequency and is defined as [Treumann and Baumjohann, 1997b]

$$P_j = \frac{q_i B}{m_j}. \tag{2.12}$$

The particle j circles the field line with frequency P_j and the radius of the circular motion is $r_{c,j} = v_{\perp,j}/|P_j|$, with $v_{\perp,j}$ the speed perpendicular to the field. Ions and electrons gyrate in opposite directions and electrons have a smaller r_c due to their negative charge and smaller electron mass, respectively. In the next section the motion of reflected ions around IMF lines are discussed, and the cyclotron motion is illustrated (Figure 2.4).

Two assumptions are needed for an MHD treatment of a plasma: First, the time scale of interest (τ) must be much longer than the gyroperiod of the heaviest ions in the plasma. This implies that for the frequency $\omega_\tau = 2\pi/\tau$, $\omega_\tau/P_i \ll 1$. Secondly, it is assumed that the characteristic speeds V_s and V_A are both much smaller than the speed of light, i.e. $V_A/c \approx P_i/\omega \ll 1$, with ω the plasma frequency (equation 2.8). These two approximations imply that $\omega_\tau \ll P_i \ll \omega$. For a neutral plasma consisting of ions and electrons (i.e. plasma density $N = N_i = N_e$) the mass density is $\rho = N(m_i + m_e)$, fluid velocity is $\mathbf{v} = (m_i\mathbf{v}_i + m_e\mathbf{v}_e)/(m_i + m_e)$, and the current density is $\mathbf{j} = Ne(\mathbf{v}_i - \mathbf{v}_e)$. Now the continuity equation is

$$\frac{\partial \rho}{\partial t} + \nabla \cdot \rho\mathbf{v} = 0 \tag{2.13}$$

and the momentum equation, including the $\mathbf{j} \times \mathbf{B}$ force, is

$$\rho \frac{d\mathbf{v}}{dt} = \mathbf{j} \times \mathbf{B} - \nabla p. \tag{2.14}$$

If an adiabatic fluid is assumed, i.e. zero heat transfer to or from the plasma, then

$$\mathrm{d}p/\mathrm{d}\rho = \gamma p/\rho. \tag{2.15}$$

Furthermore, the j terms in Ohm's law are negligible, so that

$$\mathbf{E} + \mathbf{v} \times \mathbf{B} = 0. \tag{2.16}$$

Using the low-velocity approximations to Maxwell's curl equations yields

$$\nabla \times \mathbf{E} = -\frac{\partial \mathbf{B}}{\partial t} \quad (2.17)$$

$$\nabla \times \mathbf{B} = \mu_0 \mathbf{j} \quad (2.18)$$

The four MHD equations (2.14 – 2.16), with the requirement that $\nabla \cdot \mathbf{B} = 0$, describe the quantities $\mathbf{v}$, $\mathbf{j}$, $\mathbf{E}$, $\mathbf{B}$, P and ρ. This derivation may be followed in more detail in Walker [2005].

2.4 The Bow Shock Wave and the Ion Foreshock

The Earth's magnetic field obstructs the solar wind flow, carving out a region around the Earth known as the magnetosphere. The physical processes that eventually result in pulsations of the Earth's magnetic field occur at the interface of the solar wind and the magnetosphere. These processes and the environment where they occur are discussed in this section.

Equations 2.6 and 2.7 define the sound and Alfvén speeds – the speed at which sound and Alfvén waves can travel in the solar wind. For conditions near the Earth both V_s and V_A are near 60 km.s^{-1} whereas the average solar wind flow is around 450 km.s^{-1}; that makes the solar wind flow near the Earth supersonic. Flow in a medium is defined as supersonic if the Mach number – the ratio between the flow speed (V_{SW} in this case) and the speed of sound (or Alfvén) waves – is greater than 1. The ratio between flow and sound (Alfvén) waves is called the sonic (Alfvénic) Mach number and is defined by

$$M_s = \frac{V_{sw}}{V_s} \text{ (sonic Mach number)} \quad (2.19)$$

$$M_A = \frac{V_{sw}}{V_A} \text{ (Alfvénic Mach number)} \quad (2.20)$$

For $V_s = 60$ km.s^{-1} and $V_{sw} = 450$ km.s^{-1} the sonic Mach number is $M_s = V_{sw}/V_S = 7.5$. The result of the supersonic solar wind flow is that the perturbative effect that the Earth's field has on the medium cannot be "communicated" effectively into the upstream direction by sound or Alfvén waves [Burgess, 1995]. Instead, the perturbations propagate a short distance upstream where they coalesce into a thin viscous layer that forms a standing shock wave upstream of the Earth and is known as the bow shock [Quest, 1988]. The disturbed region downstream of the shock and upstream of the geomagnetic field is known as the magnetosheath; upstream of the bow shock the plasma is undisturbed. The near-Earth environment including the bow

shock and the upstream region is illustrated in Figure 2.3. The location of the shock wave is approximately determined by the balance in the pressure gradient forces due to the incoming solar wind and the outward pressure of the Earth's dipole field. At the stagnation point, where the flow becomes tangential to the dipole field a current sheet is set up and the associated magnetic field cancels the geomagnetic field upstream of the sheet while enhancing the downstream field [Burgess, 1995]. The surface traced out by the current sheet, beyond which the effect of the geomagnetic field is not observed is known as the magnetopause. As solar wind particles approach the magnetosphere, they undergo gyration motion due to the Lorentz force ($\mathbf{J} \times \mathbf{B}$) generated by the current and the geomagnetic field [e.g. Hughes, 1995]. After only half a gyration the electron (or proton) returns to the solar wind plasma in the opposite direction; this motion serves to separate the solar wind plasma from the magnetosphere. The electron (proton) motion the opposite (same) direction as the current due to the radial motion forms the current J. Assuming that the solar wind plasma is perfectly reflected, the momentum flux into the current sheet is $2\rho_{sw} u_{sw}^2$, where ρ is the density and u_{sw} is the solar wind speed. The pressure-balance across the boundary dictates that the magnetic and dynamic pressures must be equal, yielding $B^2/\mu_0 = 2\rho_{sw} u_{sw}$ [e.g. Hughes, 1995]. The cavity enclosed by the magnetopause – the region in which the Earth's field is observed – is the magnetosphere. The shape of the magnetosphere is that of the dipole field distorted by the solar wind – compressed on the day side and stretched into the elongated magnetotail region on the night side. The plasma is slowed and altered by the shock wave, dissipating energy from the solar wind so that subsonic flow around the magnetosphere is possible [e.g. Burgess, 1995]. Plasma parameters upstream and downstream of the shock are related by the shock jump (or Rankine-Hugoniot) conditions [Burgess, 1995]:

$$U_u - U_d + \left(\frac{1}{\rho_u} - \frac{1}{\rho_d}\right) p_u + p_d + \frac{1}{2\mu_0} B_{u,t} - B_{d,t}^2 = 0 \qquad (2.21)$$

$$\left(\rho U_n\right)^2 \left(B_{u,t}/\rho_u - B_{d,t}/\rho_d\right) = \frac{B_n^2}{\mu_0}\left(B_{u,t} - B_{d,t}\right) \qquad (2.22)$$

$$\left(\frac{1}{\rho_u} - \frac{1}{\rho_d}\right)\left(\rho U_n\right)^2 = p_u - p_d + \frac{1}{2\mu_0}\left(B_{u,t}^2 - B_{d,t}^2\right) \qquad (2.23)$$

$$U_{u,t} - U_{d,t} = \frac{B_n}{\mu_0 \rho U_n}\left(B_{u,t} - B_{d,t}\right) \qquad (2.24)$$

Quantities upstream and downstream of the shock are indicated by u and d subscripts, U is flow speed, ρ is mass density, p is pressure and the subscripts t and n denote components tangential and normal to the shock, respectively. The shape of the shock wave is approxi-

mately parabolic [Cairns and Lyon, 1995]:

$$x = R_{bs} - a(y^2 + z^2) \tag{2.25}$$

with $R_{bs} = \Delta_{sh} + R_{mp}$ the stand-off distance from the Earth (Δ_{sh} is the width of the sheath and R_{mp} the distance from the Earth to the magnetopause) and a determines the flaring of the shock from the nose. The pressure at the stagnation point p_s is determined by [e.g. Spreiter et al., 1966; Walker and Russell, 1995]

$$K = \frac{p_s}{\rho_{sw} u_{sw}^2} = \left(\frac{\gamma+1}{2}\right)^{(\gamma+1)/(\gamma-1)} \left(\frac{\gamma+1}{\gamma-1}\right)^{1} / 2M_s^{2\,-\,1/(\gamma-1)}. \tag{2.26}$$

The density and speed just upstream of the bow shock in the solar wind are ρ_{sw} and u_{sw}, and γ is the polytropic index. M_s is the sonic Mach number at the shock. The pressure balance in terms of K is [Walker and Russell, 1995]

$$K\rho_{sw} u_{sw}^2 = \left(\frac{aB}{2\mu_0 R_{mp}^6}\right)^2. \tag{2.27}$$

Solving for the distance from the Earth to the nose of the magnetopause yields

$$R_{mp} = \left(\frac{B^2}{2\mu_0 \rho_{sw} u_{sw}^2} \frac{a^2}{K}\right)^{\frac{1}{6}}, \tag{2.28}$$

first derived by Spreiter et al. [1966]. Here, K is the stagnation pressure ratio (equation 2.26), B is the geomagnetic field magnitude in the equatorial plane and a is a compression factor to be determined empirically. For average solar wind conditions equation 2.28 may be written in terms of measurable solar wind parameters – density N_{sw} and flow speed V_{sw} [e.g. Walker and Russell, 1995; Heilig et al., 2010]:

$$R_{mp} = 110.2(N_{sw} V_{sw}^2)^{-1/6}. \tag{2.29}$$

Spacecraft measurements show that the bow shock is located about 13 R_E from the Earth, 2 R_E upstream from the magnetosheath under average solar wind conditions (see Figure 5.5(b) in Chapter 5.2, for example).

The Mach number of the shock is an indication of the amount of energy dissipated by the

shock as the solar wind plasma crosses the shock and flows around the geomagnetic field. In collisional media the energy dissipation across the shock is provided by the collisions between particles as they cross the shock. In the solar wind plasma, however, the scale length of the shock is smaller than the mean free path between particles so the dissipation is affected by the interaction of the charged particles with the electromagnetic fields and currents near the shock [Burgess, 1995]. Hence the bow shock is classified as collisionless. Two mechanisms of energy dissipation are at work in the shock. At low Mach numbers ions are thermalised and scattered downstream of the shock by Joule heating due to the currents set up at the shock. At higher Mach numbers ion reflection from the shock provides the necessary downstream heating and entropy increase [Burgess, 1995]. Ions and electrons propagate upstream along the penetrating IMF lines under guiding centre and cyclotron motion.

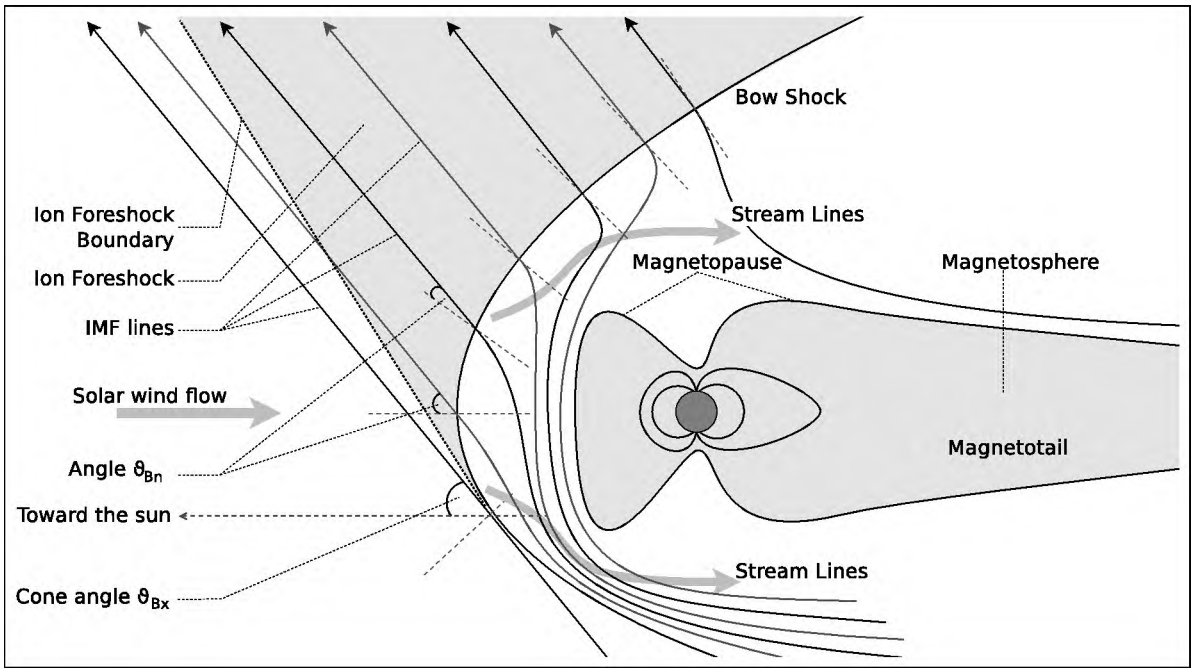

Figure 2.3: The foreshock / bow shock / magnetosphere environment. A northward IMF configuration defines the foreshock region, with the ion foreshock depicted by the shaded area. Field lines bend away from the shock normal (dashed lines on the bow shock) and are draped over the magnetopause as described by Spreiter et al. [1966]. The solar wind flow and stream lines are indicated with thick arrows and the Earth and its distorted dipole field is indicated inside the shaded magnetosphere.

2.4.1 Particle and Wave Populations in the Ion Foreshock

Due to the oblique angle of IMF lines with respect to the Sun-Earth line some field lines penetrate the shock wave while others are not connected to the shock. The connected and disconnected upstream regions are separated by a tangential field line (see Figure 2.3). Observations made aboard early spacecraft indicated that the plasma in the connected region of upstream space was more turbulent and contained more energetic particles than the ambient solar wind plasma observed in the disconnected region [e.g. Fuselier, 1994]. Ions and electrons propagate upstream from the bow shock with velocity $\mathbf{v}_B$ along the IMF lines and a component $\mathbf{v}_W$ due to downstream convection with the solar wind. Since the more energetic electrons travel further upstream than the ions, i.e. $\mathbf{v}_{B,e} > \mathbf{v}_{B,i}$, the ions are convected further downstream than the electrons. The region with abundant electrons is traced out just downstream of the tangential field line, and is known as the electron foreshock. The ion foreshock is the region downstream of the electron foreshock, where abundant populations of ions are found. The ion foreshock is important for the generation of Pc3's since it serves as the habitat for various ULF wave species that drive the downstream perturbations responsible for exciting ULF waves in the magnetosphere. Due to its curved shape the angle θ_{Bn} between the local shock normal and the IMF changes along the shock surface. Dashed lines along the bow shock in Figure 2.3 indicate the local shock normal. The region with $\theta_{Bn} < 45^0$ is designated "quasi-parallel" and the $\theta_{Bn} > 45^0$ region is "quasi-perpendicular". At the quasi-perpendicular region of the shock the IMF lines are nearly parallel to the shock surface. In this case reflected ions propagate upstream only for a few gyrations around the field line before they re-enter the shock. The particle is energised in the cyclotron motion and heats the downstream plasma upon re-entry to the shock, thus contributing to the energy dissipated by the shock. For the quasi-parallel region, however, the IMF line points away from the shock surface and particles can propagate far upstream. From now on the ion foreshock will be referred to simply as the foreshock.

Beams of upstream propagating ions are thought to be the first in a chain of processes necessary for the generation of downstream ULF activity. Under cyclotron motion beams of ions gyrate upstream along the penetrating field lines. Various mechanisms capable of generating these upstream propagating beams are briefly discussed.

Reflection from the shock. Sonnerup [1969] used a simple geometric treatment to show how particles are accelerated away from the bow shock by undergoing displacement along

the interplanetary electric field during the reflection process. Later Paschmann et al. [1980] generalised the geometry and confirmed that the theory agrees with observations aboard the ISEE 1 and 2 spacecraft. Initially, a reference frame in which the incident solar wind velocity $\mathbf{v}_i$ is along B_{IMF} is chosen. This choice of frame results in a zero interplanetary electric field (since $\mathbf{v}_i \times B_{IMF} = 0$), and, assuming that no other acceleration process is present, the reflected particle's energy is conserved under reflection:

$$v_{\perp i}^2 + v_{\parallel i}^2 = v_{\perp r}^2 + v_{\parallel r}^2. \tag{2.30}$$

The $\parallel$- and $\perp$-signs denote components parallel and perpendicular to the IMF of the incident (i) and reflected (r) velocities. Then, in a frame with the angle θ_{Bv} between $\mathbf{v}_i$ and B_{IMF} non-zero, resulting in a non-zero electric field, the ratio between incident and reflected particle energy is calculated, and written as a function of the angle θ_{Bn} between the shock normal $\hat{\mathbf{n}}$ and B_{IMF}, the angle θ_{Vn} between $\hat{\mathbf{n}}$ and $\mathbf{v}_i$, and θ_{Bv}:

$$E_r/E_i = 1 + 2(1+\delta)\frac{\cos^2\theta_{Vn} - \cos\theta_{Vn}\cos\theta_{Bn}\cos\theta_{Bv}}{\cos^2\theta_{Bn}}. \tag{2.31}$$

The constant factor δ is between 0 and 1 for a cold plasma and determines the ratio between the parallel components of the incident and reflected particle velocity: $v_{\parallel r} = \delta v_{\parallel i}$. This theory suggests that, apart from the magnetic moment, which determines δ, it is only the IMF, solar wind velocity and local shock structure that determines the acceleration of the reflected particles. Paschmann et al. [1980] confirmed the theory by using solar wind energy, velocity and IMF direction measurements made over 18 selected events by the ISEE 1 and 2 space craft, to compare the measured and modelled energy ratios as determined by equation 2.31.

Leakage from the shock. Shock waves in a collisionless plasma contain irregularities in magnetic structure. As charged particles move through the shock wave they are scattered and accelerated by the inhomogeneities, either in the upstream or downstream direction [e.g. Burgess, 1995]. It is possible for these particles to experience multiple reflections, resulting in substantial acceleration, before escaping the shock. This acceleration mechanism, first proposed in order to explain cosmic radiation, is known as first order Fermi acceleration. Given the turbulence in the magnetosheath region, directly behind the bow shock, Kovner and Feldstein [1973] argues that this mechanism must be responsible for the observed acceleration of protons into the foreshock region.

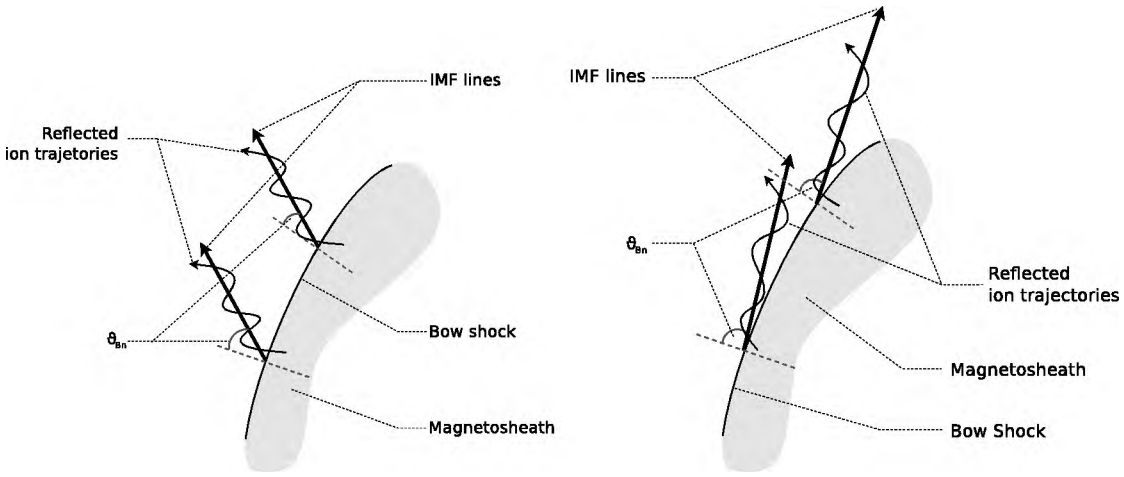

(a) Quasi-parallel shock (b) Quasi-perpendicular shock

Figure 2.4: Specular reflection of ions from the quasi-parallel and quasi-perpendicular bow shock. From a parallel shock the particle can escape upstream, but in a quasi-perpendicular configuration the particle returns, energised by the cyclotron motion, to heat the shock.

Specular reflection from the shock. Specularly reflected ions have their velocity normal to the shock reversed under reflection while the tangential component remains constant. Reflection off the quasi-perpendicular shock results in the guiding centre motion of the ions to point back towards the shock so that the ion gains energy before returning to the shock. The returned ions act as a source of free energy to the magnetosheath [Fuselier, 1994]. Figure 2.4 shows the scenarios for the quasi-parallel and quasi-perpendicular cases.

In the late 1960's populations of energetic particles [e.g. Asbridge et al., 1968] and low frequency waves [e.g. Fairfield, 1969] were observed in the foreshock region. In the 1970's the ISEE 1 and 2 spacecraft yielded valuable observations of particle populations in the ion foreshock. Three ion populations could be distinguished in the ion foreshock. Directly downstream of the foreshock boundary a population with a narrow, beam-like energy distribution is observed. This population was termed "reflected" [e.g. Bonifazi and Moreno, 1981a; Le and Russell, 1994], as it is believed to be leaked or reflected from the quasi-perpendicular region of the foreshock. Further downstream of the foreshock boundary the ions become more isotropic, with wider distributions of energy and pitch angle. These ions are termed "intermediate" [Fuselier, 1994]. Even further downstream, near the dawn sector of the foreshock the distribution is almost isotropic. The "diffuse" ion population has a flat velocity distribution [Russell and Hoppe, 1983]. In addition to the ion populations, wave activity of

various characteristic frequencies were observed. Near the foreshock boundary, low amplitude waves of approximately 1-second periods are found to be generated by an electron beam counter-streaming instability. Le and Russell [1992] used historical ISEE measurements from 1978, collected during intervals with relatively constant IMF conditions, so that measurements recorded with the downstream moving spacecraft yield a geometrically dependent profile of waves and particles in the foreshock. In the region populated by the intermediate and diffuse populations, ULF waves (30 s period) are observed. These are transverse waves with a nearly monochromatic spectrum and left-hand polarisation; they are initially upstream propagating and right-handed, but are convected downstream by the solar wind and hence are observed with opposite polarisation. In the diffuse ion region large amplitude compressional oscillations with steepened waveforms (called shocklets) and frequency of about 0.04 Hz are observed. These shocklets may further transform into discrete whistler mode wave packets [Hoppe et al., 1981].

Scarf et al. [1970] was the first to correlate the particles with wave activity. During an upstream event Ogo 5 measurements were used to correlate large fluctuations in the magnetic field with the presence of energetic (4 – 7 keV) proton fluxes. Scarf et al. [1970] concluded that the field oscillations were due to counter-streaming protons and suggested that the upstream propagating protons were being scattered by a wave-particle instability.

Although different terminology is used, most authors agree on the nature of the instability responsible for the upstream propagating waves. The waves are essentially ion-cyclotron modes, excited by counter-streaming beams of upstream moving ions and downstream propagating solar wind plasma [e.g. Treumann and Baumjohann, 1997a]. The resonance condition for these waves is defined by the beam motion parallel to the field lines $\mathbf{k}\cdot\mathbf{V}_b$ and the ion cyclotron frequency Ω_i [e.g. Gary, 1991]:

$$\omega_r - \mathbf{k}\cdot\mathbf{V}_b + \Omega_i = 0 \tag{2.32}$$

with ω_r the real part of the wave frequency

$$\omega = \omega_r + i\gamma, \tag{2.33}$$

$\mathbf{k}$ the wave vector, and $\mathbf{V}_b$ the beam velocity parallel to the magnetic field. The term $\mathbf{k}\cdot\mathbf{V}_b$ above indicates the amount of Doppler shift of the frequency due to the wave motion parallel

to the beam.

If the resonance condition is approximately satisfied the interaction becomes unstable and waves are excited. Wave growth is measured in the imaginary part of the wave frequency. The growth rate is calculated by calculating the dispersion relation between frequency and wave number k, and solving the imaginary part for γ. Growth occurs if $\gamma > 0$ and damping occurs for $\gamma < 0$.

As the ion beam propagates upstream momentum is lost to scattering by the incident solar wind plasma; i.e. the beam properties change and accordingly the wave properties change resulting in decreased group velocity (v_g) until $v_g < v_{sw}$. The result is that beam particles and waves are convected downstream by the solar wind [e.g. Krauss-Varban and Omidi, 1991]. The particle becomes part of the diffuse population observed in the quasi-parallel region of the foreshock [Russell and Hoppe, 1983]. As the waves are convected they still undergo growth to larger amplitudes [Le and Russell, 1992]. At large amplitudes non-linear wave-wave interactions dominate the linear growth and the low frequency waves steepen into the shock-like formations (shocklets) observed near the bow shock [e.g. Bonifazi and Moreno, 1981b].

2.5 Waves in the Magnetosheath

The bow shock slows the solar wind to subsonic speed and enables flow around the magnetosphere. The magnetosheath is the region downstream of the bow shock and upstream of the magnetopause where the shocked solar wind plasma flows. Due to the energy dissipated in the shock wave the sheath plasma is hotter and the flow more turbulent than the upstream solar wind. Laminar flow in the sheath region occurs only for very low Mach numbers ($M_A < 1.5$ according to [Krauss-Varban and Omidi, 1991]). For high Mach number shocks the combination of the downstream convected shocklets and the coupling of specularly reflected ions to the shock causes a re-configuration of the bow shock which induces downstream turbulence [Krauss-Varban and Omidi, 1991]. Spreiter et al. [1966] modelled the sheath flow in a purely gas dynamical approach and extended it to include the magnetic field by assuming the frozen in flux condition ($\mathbf{E} + \mathbf{V} \times \mathbf{B} = 0$) holds. This approximation provided a fairly accurate picture of magnetosheath flow in the MHD limit – i.e. for length scales much larger than the ion gyroradius.

As the flow is directed around the magnetopause the magnetic field lines frozen into the

plasma are draped around the magnetopause. For fast mode shocks (as is the case with the terrestrial bow shock) the field lines are refracted away from the shock normal in the transition from the upstream to the downstream plasma. It has been observed that magnetosheath turbulence is dependent on upstream solar wind conditions [e.g. Russell and Hoppe, 1981] and that wave activity in the magnetosheath can excite ULF waves on the magnetopause [e.g. Eriksson et al., 2006] and in the magnetosphere [Yumoto, 1985, for example]. Two instabilities capable of generating ULF waves in the sheath are dominant: the transverse mirror mode instability (MM) and the field aligned Alfvén (A) or ion-cyclotron (IC) modes.

Krauss-Varban and Omidi [1991] proposed a situation whereby upstream generated fast-mode waves maybe mode-converted to Alfvén waves in the quasi-parallel region of the sheath. They utilised a 1-dimensional hybrid code model with increasing M_A to show that upstream propagating fastmode waves will have the field aligned component of their wave vectors reversed, so that they are convected downstream by the solar wind across the shock and into the sheath region. Krauss-Varban and Omidi [1991, 1993] showed through one and two dimensional hybrid code simulations, respectively, that the upstream propagating waves excited by ion beam instabilities near the shock are convected downstream for $M_A > 3$. Furthermore, they showed that the downstream convected fast mode magnetosonic waves are mode converted to the A / IC mode as the fast magnetosonic mode becomes inaccessible across the shock. The propagation of the A / IC waves are field aligned but their wave vectors still point upstream along the field normal, i.e. $\mathbf{k} \parallel \mathbf{n}$. In the quasi-perpendicular shock field aligned Alfvén waves, as well as transverse waves excited by a mirror mode instability, may be excited by the temperature anisotropies found in this region of the sheath.

As the solar wind flows along the stream lines in the sheath the plasma is heated adiabatically in regions where the flow is across field lines and cooled where the flow is parallel to the field [Treumann and Baumjohann, 1997a]. This directional heating and cooling of the sheath plasma results in temperature and pressure anisotropy that is preferentially activated in the region behind the quasi-perpendicular shock [Treumann and Baumjohann, 1997a]. Due to the anisotropy a non-resonant mirror mode instability may be set up in the sheath. This instability excites low frequency $\omega < \Omega_i$ waves that propagate across the magnetic field. The growth condition for the mirror mode is [Treumann and Baumjohann, 1997a]

$$1 < \sum_s \left(\frac{16_{s,\perp}^2}{16_{s,\parallel}} - 16_{s,\perp} \right) \qquad (2.34)$$

with $\beta_{s,\perp}$ and $\beta_{s,\parallel}$ the species s plasma beta ratio in the directions parallel and perpendicular to the magnetic field, respectively. For large anisotropy in the perpendicular direction the term on the left will dominate.

It is shown by Omidi et al. [1994], Treumann and Baumjohann [1997a], and Shoji et al. [2009] that the linear growth of the IC waves is greater than that of the MM waves. Observations, however, suggest that both are present, and that the mirror mode dominates the IC mode. Omidi et al. [1994] and Shoji et al. [2009] both describe the competition between the IC and MM waves and explain how mirror mode waves can dominate the IC modes. According to Omidi et al. [1994] the mirror mode can dominate if the anisotropy in the sheath is driven by the solar wind buffeting of the shock, instead of starting with an initial anisotropy and allowing it to relax to isotropy. If the anisotropy persists throughout the sheath the MM and IC waves are generated near the shock and propagate downstream. Under these conditions the MM waves may propagate further than the IC waves. Shoji et al. [2009] used a three-dimensional model to show how the MM waves can consume the free energy provided by the temperature anisotropy causing the IC mode to saturate. Due to its oblique propagation the MM waves are excited over a larger range in wave vector space (**k**-space). The MM waves can then gain more free energy than the IC waves and the lack of free energy causes the IC waves to saturate faster than the MM waves.

However, Narita et al. [2006], through a statistical analysis of sheath measurements taken by the Cluster family of spacecraft, concluded that upstream and downstream wave activity does not correspond enough to validate the downstream convection of upstream waves as predicted by the Krauss-Varban and Omidi [1991] model. According to Krauss-Varban and Omidi [1991] the sheath wave vectors should point upstream while they are convected downstream through the sheath, but Narita et al. [2006] found that although foreshock waves exhibit this behaviour, waves in the sheath were in fact slow mode / mirror mode waves propagating transverse to the IMF toward the magnetopause. This was observed both in the quasi-parallel and quasi-perpendicular regions of the sheath.

2.6 Observational Evidence of Exogenic Sources of Pc3's

Since the earliest observations of the near-Earth solar wind, the possibility of extra-magnetospheric sources of pulsation activity had been proposed, due to the correlation between solar wind

parameters and pulsation observations. The first correlations observed were the dependence of pulsation amplitude on solar wind speed and a linear relationship between IMF magnitude and Pc3 frequency. Saito [1964] first discovered a positive correlation between pulsation amplitudes and solar wind speed and later Wolfe et al. [1980] confirmed the high linear correlation between solar wind speed and Pc3 amplitude for two events in the Pc3 – 5 bands. Wolfe et al. [1980] found the highest correlation with $_{Vsw}$ in the 30.7 - 60s period range, with progressively lower positive correlations in the 60 - 120s and 120 - 240s ranges. Recently Heilig et al. [2007] published results confirming the positive correlation between $_{Vsw}$ and Pc3 amplitude in a statistical analysis of a 132 day interval during 2001.

Through the analysis of measurements collected over a number of Explorer 34 orbits, Fairfield [1969] observed waves in the 10 – 50 mHz range in the foreshock, and noted the influence of IMF direction on the generation of upstream propagating waves: waves are only observed on IMF lines that intersect the bow shock (i.e. IMF is not quasi-perpendicular to the bow shock normal). This observation can be explained by the ion beam instability described earlier. Kovner et al. [1976] analytically investigated the generation of waves upstream of the bow shock and could explain some of the earlier experimental results linking IMF direction to Pc3 occurrence and $_{Vsw}$ with Pc3 amplitude. They found that upstream wave growth rate is optimal when IMF direction is not quasi-perpendicular to the Sun-Earth line. Greenstadt and Olson [1976] defined the cone angle U_{Bx} as the acute angle between the IMF and the direction parallel to the Sun-Earth line as an indication of IMF orientation:

$$U_{Bx} - \cos^{-1} \frac{B_x}{B} \tag{2.35}$$

with B_x the IMF component pointing to the Sun and B the IMF magnitude (cone angle is indicated in Figure 2.3). Due to the spiral formation of the magnetic field frozen into the solar wind plasma the cone angle under average conditions is about 45^0. When the IMF is nearly aligned with the Sun-Earth line (i.e. small U_{Bx}) the extent of the ion foreshock region is enhanced and more of the upstream generated waves can be transmitted downstream. Engebretson et al. [1986] noted the IMF control of pulsations when the Pc3/4 activity suddenly resumed upon IMF orientation from large (U_{Bx} sas $75^0 - 85^0$) to small ($25^0 - 40^0$) cone angle. Clausen et al. [2009] used multiple instruments (Geotail, Cluster, ground magnetometers) to simultaneously observe ULF activity upstream of the bow shock, in the magnetosphere, and on the ground at a middle to high latitude array of stations ($60.2^0 - 78.7^0$ N).

Bol'shakova and Troitskaya [1968] found that the occurrence of Pc3's is also correlated with the direction of the interplanetary magnetic field (IMF), confirming that the source of these pulsations must lie outside the magnetosphere. Later Troitskaya et al. [1971] used IMF measurements from the IMP-3 and IMP-4 spacecraft to find an empirical relation between IMF magnitude and Pc3–4 pulsation period. Rewritten in terms of frequency (f), it becomes

$$f = a\, B_{IMF} \tag{2.36}$$

with f the frequency of the observed pulsation in Hz, B_{IMF} the IMF strength in nT and $a = 0.00625$ a constant. This relation suggests that the origin of these pulsations lies outside the magnetosphere and that the gyration of ions around the IMF lines plays a role in the generation of pulsation activity. Subsequent investigations into this relationship yielded several values for the constant factor, all approximately 6×10^{-3} [Troitskaya, 1994]. Russell and Hoppe [1981] further elucidated the previous findings, and showed that this relation between IMF strength and frequency also holds (with $a = 0.0058$) for waves in the region upstream of the magnetosphere – establishing a connection between IMF, upstream waves (UW's) and ground-based Pc3's.

2.7 ULF Waves in the Magnetosphere

The correlations between solar wind parameters and Pc3 pulsations measured on the ground suggest that their source must lie beyond the bow shock. In order for Pc3's to be observed on the Earth's surface, energy must be transferred from the sheath, across the magnetopause deep into the magnetosphere, and up to the ionosphere where coupling with ionospheric currents can occur so that the horizontal component of the geomagnetic field is perturbed. Field line resonances provide the coupling between the magnetosphere and the ionosphere.

2.7.1 Compressional Pc3 Waves in the Magnetosphere

The ULF waves generated in the foreshock region are transmitted through the magnetosheath and into the magnetosphere where they propagate to low latitudes as compressional waves in the Pc3 frequency band. Correlations between IMF magnitude and compressional Pc3-4 (16 – 100 mHz) waves observed in the magnetosphere at geostationary orbit reported by Yumoto et al. [1984] is evidence of the direct propagation of foreshock waves, generated by the

ion-cyclotron mechanism described above, across the magnetosheath and into the magnetosphere. Magnetic field measurements from the low-Earth orbiting CHAMP spacecraft were used by Heilig et al. [2007] to show that these waves can propagate up to the topside ionosphere. Yumoto [1985] described the various ways in which these waves can couple to MHD waves in the magnetosphere and eventuallybe observed as Pc3's on the ground. Fundamental and higher harmonics of field line resonances and cavity or waveguide modes (all described below) can couple to the incident compressional waves. Furthermore, surface waves on the plasmapause and low latitude standing oscillations in the plasmasphere are listed as possible couplings.

2.7.2 Field Line Resonances (FLR's)

The ends of the Earth's dipole field lines are rooted in the ionosphere in opposite hemispheres. When a field line is displaced it returns to its equilibrium position due to a restoring tension force, much like a guitar string. The restoration is not perfect because field lines overshoot their equilibrium position due to the momentum of the charged particles gyrating around the field lines and they continue to oscillate after the initial displacement. Two modes of field line oscillation are possible. The toroidal mode oscillates in the azimuthal direction (Figure 2.5(a)) and the poloidal mode describes radial displacement of the field line (Figure 2.5(b)). Azimuthally adjacent field lines share similar resonant frequencies since they lie at the same radial position [e.g. McPherron, 2005]. It is possible for a field line oscillating with the toroidal mode to excite neighbouring field lines on the same L-shell. This, and the fact that toroidal modes do not change the density or magnetic field magnitude on the vibrating field lines (due to the direction of the displacement), ensures that toroidal modes are more commonly observed in the magnetosphere than poloidal modes [McPherron, 2005].

A field line is displaced when incident waves from the outer magnetosphere resonate with Alfvén waves on the field line by matching their wavelengths parallel to the field line with the Alfvén wavelength on a field line [Walker, 2005]. The resonance condition is $\omega = \pm k_z V_A$, with k_z the wave number along the field $\mathbf{B} = B\mathbf{z}$ [McPherron, 2005]. The eigenfrequency of a field line may be approximated by integrating over the field line length ds:

$$f^{-1} = \int \frac{ds}{V_A}, \qquad (2.37)$$

and depends on line length, and the magnetic field strength and particle density on the field

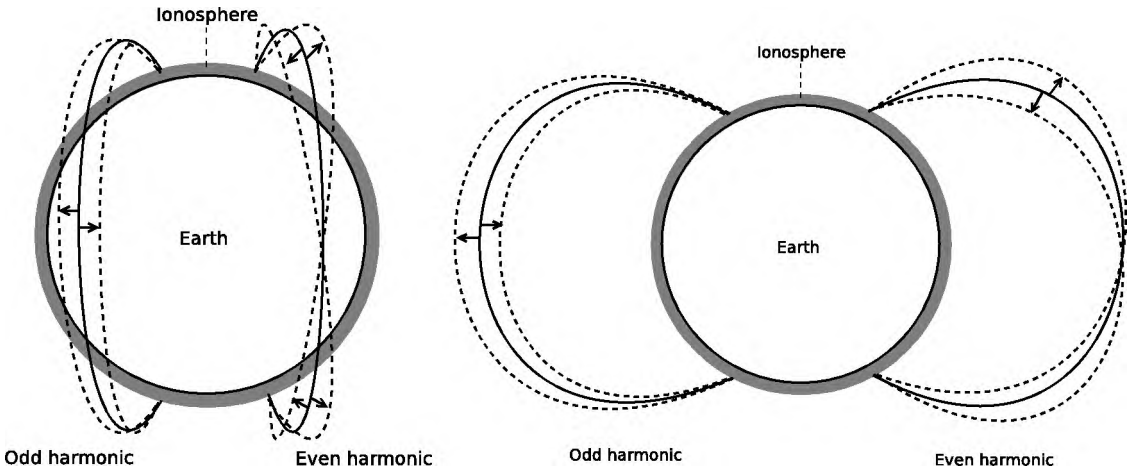

(a) Toroidal mode. (b) Poloidal mode.

Figure 2.5: Toroidal and poloidal mode resonances of dipole field lines.

line through V_A. Fraser et al. [1988] used ISEE 1 density and magnetic field measurements in the magnetosphere to calculate V_A for $L \approx 3.5-6\ R_E$. From the radial profile of V_A the resonant frequency of toroidal mode FLR's was calculated for the first six harmonics of the toroidal mode.

For FLR-related pulsations to be observed at low latitudes on the ground (conjugate field lines with low L-values) means that waves coupling to the field lines must be sustained to propagate several R_E to the inner magnetosphere. Yumoto [1985] used ISEE 3 and GOES 2 observations and measurements from two ground stations to relate solar wind data to Pc3's on the ground and suggested that it is compressional waves from a broadband source near the magnetopause that couples to FLR's near the Earth. This mechanism was confirmed, for example, by Engebretson et al. [1986] who used magnetic field measurements from the AMPTE and IMP8 spacecraft to simultaneously observe multiple harmonics of toroidal mode FLR's with an increase in broadband compressional wave power. Later, Ndiitwani and Sutcliffe [2009] confirmed the results from Engebretson et al. [1986] with simultaneous observations of compressional waves driving toroidal mode oscillations resulting in Pc3 band pulsations in the H and D components of the surface field (geomagnetic field components are defined in equations 2.1a – 2.1c).

2.7.3 Waveguide Mode Coupling to Field Line Resonances

Kivelson and Southwood [1985] first proposed a mechanism whereby entire subregions of the magnetospheric cavity resonate at a characteristic frequency, excited by compressional waves from the outer magnetosphere. FLR theory could not explain why certain discrete frequencies matching fast mode (i.e. compressional) mode eigenfrequencies are excited, when a broadband source to FLR's should excite all available resonant frequencies in the band. Kivelson and Southwood [1985] suggested that a broadband source could resonate with fast mode waves in a cavity bounded by the resonant field line and a perfect reflector. The model notes that an incident wave from $x = +\infty$ is imperfectly reflected by the surface traced out by field lines resonant to the wave. And if a perfect reflector is placed at $x = a < \infty$, the cavity $a_{\omega} < x < a$ would sustain a fast mode wave until the wave is completely damped by the energy transfer to the field line resonance at $x = a_{\omega}$ (see Figure 2.6). Samson et al. [1992] suggested that due to the open field lines in the magnetotail a waveguide mode, rather than a closed cavity, would be more accurate. High-frequency radar observations in the local midnight to morning sector of FLR's in the Pc5 frequency range (2 – 7 mHz) were explained by the waveguide mode [Samson et al., 1992]. Compressional waves excited by a Kelvin-Helmholtz instability on the magnetopause propagate up to a turning point defined by

$$\omega^2 / V_A^2(x_t) - (k_y^2 + k_z^2) = 0 \qquad (2.38)$$

with ω the frequency, and k_y and k_z the azimuthal and field aligned wavenumbers, respectively. The observation of Pc5's at high latitudes suggests that FLR's are dependent on latitude and that longer field lines vibrate at lower frequencies. As observational evidence of FLR's excited by the waveguide mode, an analysis by Samson et al. [1995] of power spectra observed at a number of low latitude stations ($L < 3$) revealed the presence of peaks in power at closely separated frequencies, about 3 - 5 mHz apart. The fine structure was explained as the observation of multiple waveguide mode harmonics by the ground-based magnetometers. A WKB-based model of the waveguide mode predicted a similar close separation between peaks in Pc3 power [Samson et al., 1995]. The model describes a cavity enclosed by the magnetopause, with turning points in the plasmasphere; this type of waveguide mode is further motivated by their observation that the fine structure seen at $L < 3$ latitudes is not present for a high latitude ($L = 6.7$, i.e. beyond the plasmapause) event. Field line resonant Pc3's are also observed at low latitudes, up to a certain low latitude limit ($L \approx 1.4$ in Menk et al. [2000]) as power diminishes due to ion mass loading in the ionosphere, where much of the low latitude field

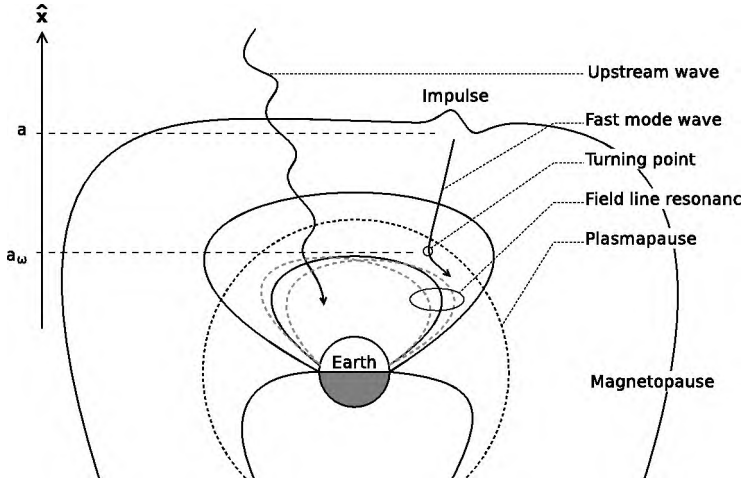

Figure 2.6: Waveguide mode between $x = a$ and $x = a_\omega$ exciting a field line to resonance with frequency ω, and an upstream generated wave propagating into the magnetosphere. This figure is adapted from Figure 1 of Samson et al. [1995].

lines reside. Menk et al. [2000] investigated low latitude FLR's ($L = 1.3 - 2$) and observed similar peaks in power spectra, separated by $3 - 5$ mHz. A low frequency component (< 40 mHz) exhibiting phase delays between stations was observed. The delay could not be explained by the propagation time of incoming fast mode waves from higher L-shells, and it is suggested that waveguide mode waves driving FLRs are responsible for the low frequency oscillation.

2.7.4 Magnetopause Oscillations and Coherent Fluctuations in the Solar Wind

Kepko [2002] showed that coherent oscillations in solar wind pressure is transmitted by the magnetopause to the magnetosphere. Increases in solar wind pressure moves the magnetopause current closer to the Earth, compressing the magnetosphere and increasing the internal magnetic field strength [McPherron, 2005]. A decrease in solar wind pressure has the opposite effect, causing the field to decrease. A step-like change in solar wind pressure generates field aligned currents into the magnetosphere that close in Pedersen and Hall currents (also see Section 2.8) in the ionosphere [McPherron, 2005]. These ionospheric currents, in turn, are observed as oscillations of the field on the ground.

The continuous buffeting of the day side magnetosphere by the incoming solar wind results in the excitation of surface waves on the magnetopause [Plaschke et al., 2009]. These are

standing Alfvén waves occurring under conditions with moderate v_{sw}, and an approximately radial, northward IMF (ϑ_{Bx} small, $B_z > 0$) [Plaschke et al., 2009]. Pressure enhancements in the solar wind plasma may act as an impulse exerted on the magnetospheric cavity providing the broadband signal that excites waveguide modes [Samson et al., 1995] capable of generating FLR's on appropriate field lines. Eriksson et al. [2006] observed the excitation of toroidal and poloidal mode FLR's by fastmode waves at 6.8 and 27 mHz (i.e. Pc3/4) simultaneously with periodic pressure enhancements in the solar wind at the same frequencies.

2.7.5 Coherent Wave Structures in the Solar Wind

Recently, Stephenson and Walker [2010] confirmed the existence of coherent ULF wave structures (2.1 mHz, Pc5 band) in the solar wind (about 240 R_E upstream of the Earth) and found a high correlation between these and high latitude FLR waves. The possibility of FLR's driven directly by waves in the solar wind is intriguing, although (according to my knowledge) no similar observations for low / middle latitude Pc3's have been published.

2.8 Ionospheric Effects on Incident Magnetospheric Waves

The transition from the fully ionised magnetospheric plasma to the Earth's neutral atmosphere is the region up to about 100 km altitude, known as the ionosphere [e.g. Treumann and Baumjohann, 1997b]. Neutral particles near the top side of the atmosphere are ionised by ultraviolet radiation from the Sun and particle precipitation from the magnetospheric plasma. Due to the high particle density in the ionosphere the collision rates between ionised particles and neutrals become significant. The ionosphere forms a conductive layer separating the magnetospheric plasma from the Earth's surface. The incident hydromagnetic waves from the magnetosphere induce currents in the ionosphere and it is the electromagnetic radiation from these currents that are observed on the ground as fluctuations in the Earth's magnetic field [McPherron, 2005]. Alfvén waves propagating along field lines into the ionosphere set up current sheets parallel to the incident field lines ($J_{\parallel}$), and the currents close in a so-called Pedersen current (J_P) on the conductive layer that is the ionosphere. A $\mathbf{E} \times \mathbf{B}$ current is also generated in the ionosphere, known as the Hall current (J_H). The incoming wave polarisation is rotated by the Hall current and depends on the (generally non-uniform) conductivity gradients in the ionosphere. In this way the MHD waves are "screened" by the ionosphere [Glassmeier, 1984]. Figure 2.7 depicts the Hall and Pedersen currents in response to an incident

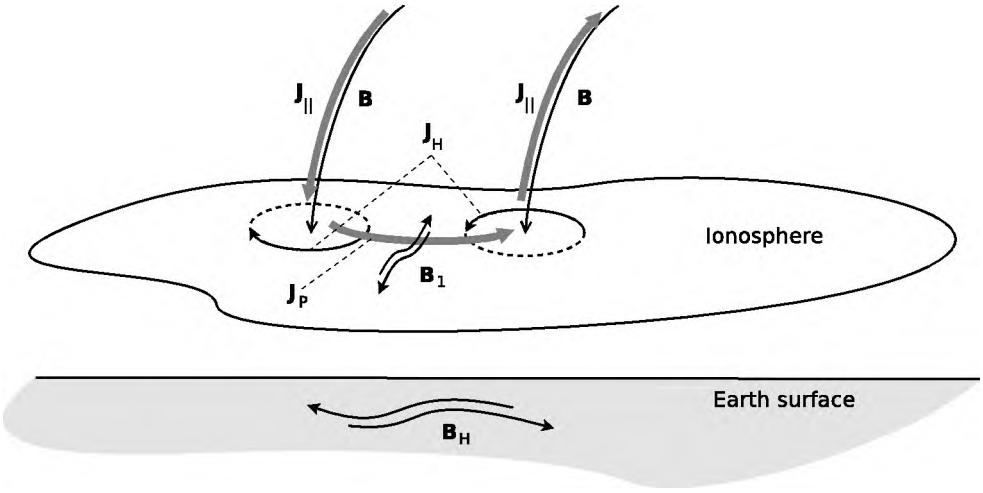

Figure 2.7: In response to an incident hydromagnetic wave the magnetic perturbations $\mathbf{B}_1$ are rotated by the Hall J_H and Pedersen J_P currents to be observed in the horizontal field component on the ground. This figure is adapted from Figure 19 in McPherron [2005].

MHD wave and the rotation of the magnetic field disturbance $\mathbf{B}_1$ to the horizontal component of the field on the ground ($\mathbf{B}_H$). Under exceptional circumstances, when the ionospheric currents are relatively uniform over the area under consideration, a near 90° rotation of the wave is observed. This was first observed by Vellante et al. [2004] and later confirmed by Ndiitwani and Sutcliffe [2009]. Furthermore, Sciffer et al. [2004] used a 1-dimensional model to simulate the transmission of ULF waves through the ionosphere and found that the small variations in wave amplitude and phase are attenuated in the passage to the surface; in this sense ionosphere acts as a low pass filter to magnetospheric ULF waves.

2.9 Summary

In this chapter the physical mechanisms important to the generation of Pc3 pulsations of the geomagnetic field were introduced. The structure of this chapter followed the chain of events leading to the observation of pulsations on the ground, from the formation of the solar wind to the rotation of magnetospheric waves by the ionosphere. Concepts that will be addressed later on like ion-cyclotron resonances and the correlation between solar wind parameters and Pc3 characteristics were highlighted as well.

Chapter 3

Artificial Neural Networks

Biological neural networks consist of large numbers of neurons (e.g. $\sim 10^9$ in the human brain [Haykin, 1994, pg. 1]) that are connected to each other via synapses. Learning through experience happens due to the forging and adaptation of the connections between neurons, enabling creatures to solve complex tasks and to adapt their reaction to stimuli based on previous experience. Artificial neural networks (ANN's) are computational structures inspired by biological networks of neurons that are used to perform cognitive tasks such as optimisation and learning [Müller and Reinhardt, 1996, pg. 12]. ANN based regression and classification models are employed in various fields of research such as medicine, speech recognition and finance [Fausett, 1994, pg. 7 – 11]. ANN's are employed due to their ability to solve highly non-linear relationships between input and output parameters. Linear regressions do not provide the necessary non-linearity between input and output parameters for such a study. In each of the subsequent two chapters (4 and 5) an ANN based model is developed to perform regression of the Pc3 index – an indication of Pc3 pulsation amplitude (see equation 4.6) – from solar wind based parameters.

This chapter describes the structure of ANN's and the nodes that comprise them. The learning procedure is explained and the use of ANN's for regression is demonstrated by an example.

3.1 Structure of an ANN

An ANN consists of different types of nodes that are joined by weighted connections. Figure 3.1 depicts a network of $N + M + S$ nodes connected by $(N \times M) + (M \times S)$ weighted connec-

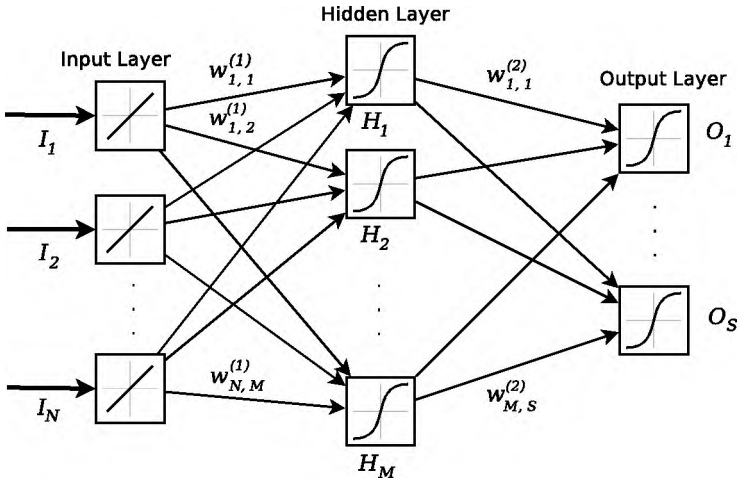

Figure 3.1: A fully connected feed forward neural network with N input nodes, M hidden nodes in a single hidden layer, and S output nodes. Input nodes have linear activation functions, and the hidden and output nodes have sigmoid-shaped activation functions. Weight $w^{(k)}_{i,j}$ connects node i in layer k with node j in layer $k+1$, with $k = 1, 2, 3$ the input, hidden and output layers, respectively.

tions (arrows). Three layers of nodes are defined: the input layer contains the input nodes (I_i with $i = 1, \ldots, N$), the hidden layer (containing the hidden nodes H_j, with $j = 1, \ldots, M$), and S output nodes (O_k, $k = 1, \ldots, S$) in the output layer. The arrows denote the direction of information flow through the network. In this case the direction of flow is in the forward direction. Such a network with flow directed strictly in the input layer → output layer direction is called a feed forward network. This network is a fully connected feed forward network, as all the nodes in a certain layer are connected to all the nodes in the next layer. In this thesis only fully connected feed forward ANN's are employed, and, therefore, other architectures are not discussed.

Every node in a network may be written as a function that produces output signals from a number of inputs. The input signals to a node in a certain layer are the weighted outputs of the nodes in the previous layer, and output signals form the inputs to the nodes in the next layer. Figure 3.2 illustrates the structure of a single node j. Weights $w_{i,j}$ are applied to N input signals $x_1, \ldots, x_N$ from the previous layer of nodes. The weighted numbers $w_{i,j}x_i$ are summed and the result forms part of the argument to the activation function $A(\cdot)$. The number b_j is a bias that is added to the sum of weighted inputs to form the argument of A. The bias is incorporated by adding a constant input signal of 1 with connection weight b_j; the output of

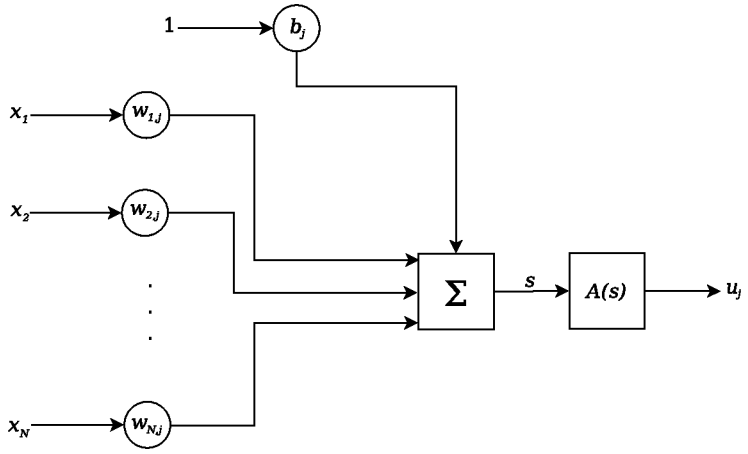

Figure 3.2: Structure of a node. Weights $w_{i,j}$ are applied to the input signals x_i, and their sum, with bias b_j, are evaluated by the activation function $A(\cdot)$ to produce the output u_j (see equation 3.1).

node j is

$$u_j = A\left(\sum_{i=1}^{N} w_{j,i} x_i + b_j\right). \tag{3.1}$$

The output of a node is determined by its activation function. Three classes of activation function are typically employed, depending on the application of the network. Threshold, or step-functions are typically used in classification models. In regression models, linear and sigmoid-type activations are used. Usually, input nodes have the identity function $f(x) = x$ as the activation function. Hidden and output nodes typically employ sigmoid-shaped functions [Fausett, 1994, pg. 17] like the hyperbolic tangent

$$A(s) = \tanh(s) = \frac{\exp(s) - \exp(-s)}{\exp(s) + \exp(-s)} \tag{3.2}$$

or the logistic function

$$A(s) = \frac{1}{1 + \exp(-\sigma s)} \tag{3.3}$$

with s the input argument and σ the steepness of (3.3). The activation function of each node is illustrated in Figure 3.1 as either linear (straight line) or sigmoidal (curved line). The use of a non-linear activation in the hidden layer enables the network to model non-linear relationships between input and output parameters [Fausett, 1994, pg. 17].

Consider a set of variables $\mathbf{O} = \{O_1, O_2, \ldots, O_S\}$ that is determined by another set of vari-

ables $\mathbf{I} = \{I_1, I_2, \ldots, I_N\}$ by some unknown function, Θ:

$$O_k = \qquad ., I_N), \; k \in \{1, \ldots, S\} \tag{3.4}$$

An ANN may be used to find approximate values of $O_1, \ldots, O_S$ for given values of $I_1, \ldots, I_N$. In ANN terminology the variables **I** are known as input parameters and **O** are output parameters. The ANN realisation of equation 3.4, with N input nodes, M hidden nodes in a single hidden layer, and S output nodes is given by equations 3.5 and 3.6 below. In a feed forward network with a single hidden layer the output parameters are determined by the output of the hidden nodes:

$$O_k = A_O \left(\sum_{j=1}^{M} w_{j,k}^{(2)} H_j + b_k \right), \quad k \in \{1, \ldots, S\} \tag{3.5}$$

and the output of the hidden nodes are determined by the input parameters

$$H_j = A_H \left(\sum_{i=1}^{N} w_{i,j}^{(1)} [I_i + b_i] + b_j \right), \quad j \in \{1, \ldots, M\} \tag{3.6}$$

The activation functions of the hidden and output nodes are denoted by A_H and A_O, respectively. The weights and biases act as the model parameters of the network, that determine its reaction to the input parameters. Weight and bias values are calculated using a process known as supervised learning [e.g. Haykin, 1994; Fausett, 1994]. Supervised learning employs a set of coinciding input and output parameter values to make a number of test predictions of the outputs, given certain input values. This is an iterative optimisation process whereby the weights and biases are adapted to minimise the error made in the test predictions. The process whereby pairs of input and output parameter values are used to adapt weights and biases is known as *training* the network. After training the optimised values of the weights and biases are fixed and the network can be used to make predictions from input parameter values. The training method applied to the ANN development in this thesis is known as the standard back-propagation algorithm first described by Werbos [1974].

3.2 The Back-Propagation Algorithm

The back-propagation algorithm uses the error made in each test prediction to calculate the adjustment to the weights and biases. In that sense the error is propagated back from the output nodes through the network to the input layer. The back-propagation algorithm is based

on the gradient descent optimisation method [Fausett, 1994, pg. 289].

A data set of *training patterns* are utilised by the back-propagation algorithm. Each pattern contains one observation of each input node, and the corresponding value of each output node. Typically, each pattern contains measurements of all input and output parameters taken at the same time. The set of training patterns consists of L observations of N input parameters $(x_{i,j})$ and S output parameters (known as target values $t_{i,k}$):

$$P = \begin{bmatrix} x_{1,1} & x_{1,2} & \dots & x_{1,N} & t_{1,1} & t_{1,2} & \dots & t_{1,S} \\ x_{2,1} & x_{2,2} & \dots & x_{2,N} & t_{2,1} & t_{2,2} & \dots & t_{2,S} \\ \vdots & \vdots & \ddots & \vdots & \vdots & \vdots & \ddots & \vdots \\ x_{L,1} & x_{L,2} & \dots & x_{L,N} & t_{L,1} & t_{L,2} & \dots & t_{L,S} \end{bmatrix} \tag{3.7}$$

The description of the back-propagation algorithm is adapted from [Fausett, 1994, Ch. 6]. The five steps below describe one iteration of the algorithm, using the training pattern r. One cycle of the algorithm denotes all L iterations, i.e. all $r = 1, \dots, L$. Typically, numerous cycles of the algorithm are required to train a network.

1. Training commences with a random initialisation of weights and biases. A small random number value is assigned to each weight and bias.

2. The outputs O_k are computed by equations 3.5 and 3.6 using input parameter values $I_i = x_{r,i}$, $i = 1, \dots, N$.

3. The error information term

$$\delta_k = (t_k - O_k) A'\left(\sum_{j=1}^{M} w_{j,k}^{(2)} H_j + b_k \right) \tag{3.8}$$

is calculated for every output parameter $k = 1, \dots, S$, using the prediction error $t_k - O_k$ and the derivative of the activation function ($A'(\cdot)$). The adjustment to be applied to weight $w_{j,k}^{(2)}$ is

$$\Delta w_{j,k}^{(2)} = \alpha \delta_k H_j \tag{3.9}$$

and bias b_k is adjusted by

$$\Delta b_k = \alpha \delta_k. \tag{3.10}$$

The number α is a constant value known as the learning rate.

4. **The error information term of hidden node j is**

$$\delta_j = \sum_{k=1}^{S} \delta_k w_{j,k}^{(2)} \; A'\left(\sum_{j=1}^{S} w_{j,k}^{(2)} H_j + b_k\right), \; j = 1,\ldots,M. \tag{3.11}$$

Weights $w_{i,j}^{(1)}$ are adjusted by

$$\Delta w_{i,j}^{(1)} = \alpha \delta_j x_{r,i} \tag{3.12}$$

and the bias correction is

$$\Delta b_j = \alpha \delta_j. \tag{3.13}$$

5. **All weights and biases are updated according to**

$$w_{i,j}^{(1)} \rightarrow w_{i,j}^{(1)} + \Delta w_{i,j}^{(1)} \tag{3.14a}$$

$$b_j \rightarrow b_j + \Delta b_j \tag{3.14b}$$

and

$$w_{j,k}^{(2)} \rightarrow w_{j,k}^{(2)} + \Delta w_{j,k}^{(1)} \tag{3.15a}$$

$$b_k \rightarrow b_k + \Delta b_k. \tag{3.15b}$$

The training of a neural network is equivalent to seeking the set of weights and biases that minimises the prediction error. The prediction error is a highly non-linear function of the weights and biases of the network, and may be visualised as an irregular multi dimensional error surface [e.g. Fausett, 1994]. The error surface has $M = K + L + 1$ dimensions, with K the total number of weights and L the number of biases [Bishop, 1995, pg. 254]. For example, a fully connected feed forward network with two input parameters, one hidden layer with two hidden nodes, and one output node, has 5 weights and 5 biases, i.e. the error function is a 11-dimensional surface. This is the layout of the network used in the example regression problem presented in the next section. In general the error surface is highly irregular, containing many local minima; the ANN training algorithm is tasked with finding the global minimum on the error surface. The minimum is sought by calculating the surface gradient in every direction and following the direction of steepest descent. Calculating the gradient requires the derivative of the activation function at many points on the surface. This makes both tanh() and the

logistic function (equations 3.2 and 3.3) good choices of activation functions since both are continuous and differentiable for all $s \in \mathbb{R}$. The constant number α is specified before training and specifies the step width of the gradient descent [Zell et al., 1998]. A very low learning rate will increase the number of cycles needed to find the global minimum, and if α is too large the minimum might be missed.

3.3 A Regression Problem Example

To illustrate the application of neural networks to a regression problem, an example is presented. The Stuttgart Neural Network Simulator (SNNS) [Zell et al., 1998] software package is used to simulate the ANN and perform the training of the network. In the previous chapter it is stated that R_{mp} [R_E], the distance from the Earth to the magnetopause, may be approximated by equation 2.29: $R_{mp} = 110.2(V_{swNP}^2)^{-1/6}$. In this example a fully connected feed forward network with two input nodes, two hidden nodes and one output node (see Figure 3.3) is employed to model the non-linear relationship between V_{sw}, N_p and R_{mp}. The input

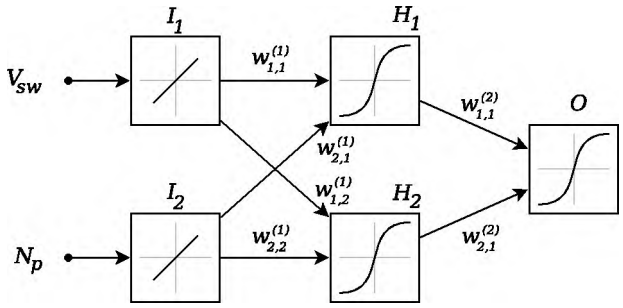

Figure 3.3: Feed forward ANN with two inputs, two hidden nodes and a single output node.

parameters are V_{sw} (measured in km.s^{-1}) and N_p [cm^{-3}], O is the output parameter, and the target output is R_{mp}. In Figure 3.4 the stand-off distance, solar wind speed, and proton density is plotted for day 50 to 100 of 2002.

The hidden and output parameters have logistic activation functions, with $\sigma = 1$, i.e.

$$A_O(s) = A_H(s) = \frac{1}{1+\exp(-s)} \tag{3.16}$$

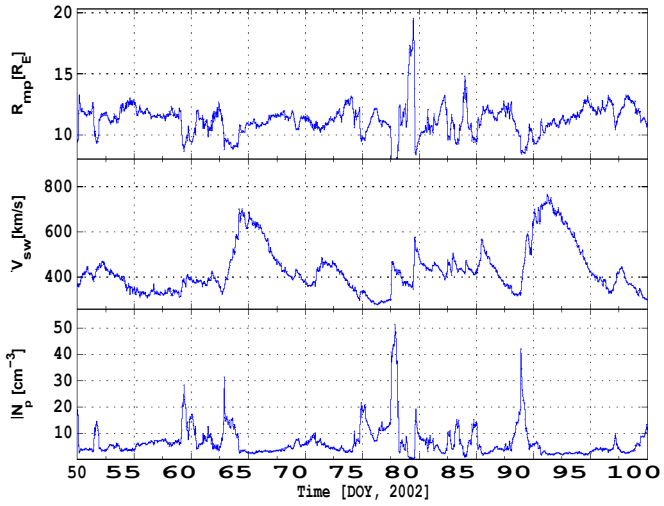

Figure 3.4: Magnetopause stand-off distance $R_{mp} = 110.2(V_{sw}^2 N_p)^{-1/6}$, solar wind speed ($V_{sw}$), and proton density ($N_p$) for day 50 to 100 of 2002.

The network (Fig. 3.3) may be written as the set of equations

$$O = f\left(1 + \exp\left(-w_{1,1}^{(2)} H_1 - w_{2,1}^{(2)} H_2 - b_O\right)\right)^{-1} \quad \textbf{(3.17a)}$$

$$H_1 = f\left(1 + \exp\left(-w_{1,1}^{(1)}(I_1 + b_{I_1}) - w_{2,1}^{(1)}(I_2 + b_{I_2}) - b_1\right)\right)^{-1} \quad \textbf{(3.17b)}$$

$$H_2 = f\left(1 + \exp\left(-w_{1,2}^{(1)}(I_1 + b_{I_1}) - w_{2,2}^{(1)}(I_2 + b_{I_2}) - b_2\right)\right)^{-1} \quad \textbf{(3.17c)}$$

The input parameters (I_1 and I_2) are V_{sw} and N_p, respectively. All input and output parameter measurements are normalised to fall between -1 and 1 in order to ensure that the scale of the different input and output parameters does not influence the training of the network. The training data set is comprised of all hourly averages of V_{sw}, N_p and R_{mp} taken between 2002 and 2005. Removing all patterns where measurement errors occur yields a set of 33420 data points out of 35024 hours in four years (including one leap year) per parameter.

The ANN simulator (SNNS) randomly sets a percentage of the training set apart to make test predictions while the back-propagation algorithm is performed. This data set is known as the testing set, and tests the network's ability to generalise beyond data seen during training. In this case 30% of the total set is used for testing; the training set consists of 23394 training patterns, and the testing set contains 10026 patterns. Training commences with a random set of weights and biases (step 1 of the back-propagation algorithm). The network is trained

for 1000 cycles with a learning rate of $\alpha = 0.1$. Figure 3.5 shows the sum of squared errors (SSE) of the testing (red) and training (black) data while training is in progress. Initially the error is large, but accuracy improves as more cycles of the back-propagation algorithm are performed.

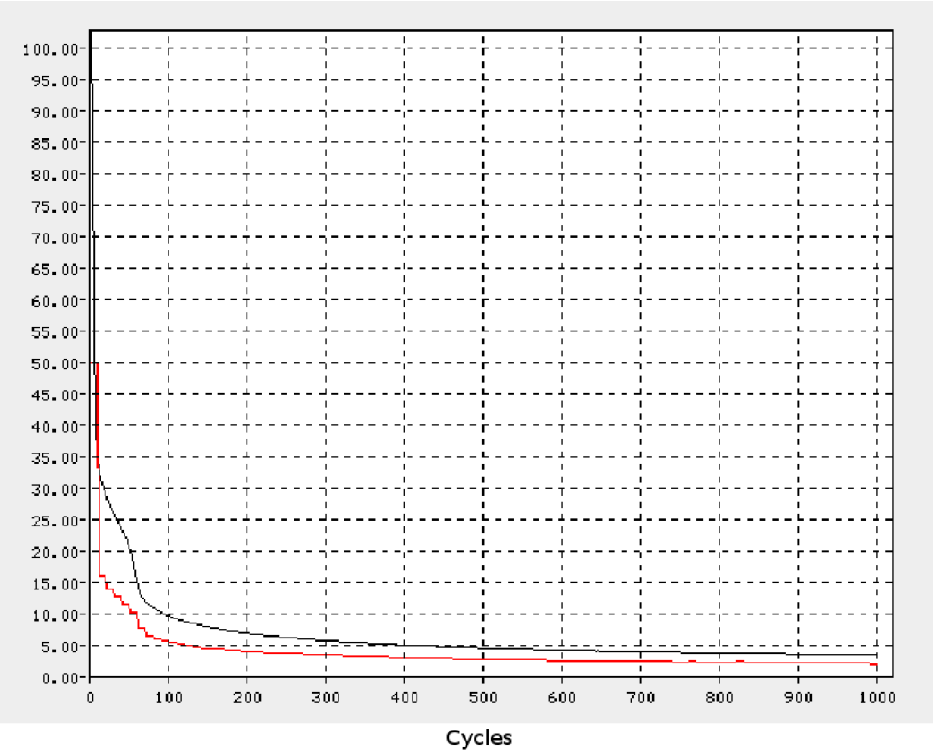

Figure 3.5: The sum of squared errors (SSE) for the testing (red) and training (black) data sets as the network is trained for 1000 cycles.

To illustrate the improvement of prediction accuracy the network weights and biases at 0 (initialised), 50, 500 and 1000 cycles are used to predict $_{R,np}$ during 2006. The weights and biases at these stages of training are listed in Table 3.1. The set of data from 2006 is known as the evaluation set and is used to evaluate the ANN after training. The evaluation set consists of data not included in the training or testing sets, i.e. it is out-of-sample, or unseen, data. Evaluating the model's prediction performance over an unseen set of data tests the model's ability to generalise beyond the data set used in training. The correlation coefficient (equation 3.18) and the root-mean-square of the error $R_{,np} - O$ (equation 3.19) is calculated for each stage of the training process. Figure 3.6 shows the measured and predicted $_{R,np}$ after 0 (initialised),

50, 500 and 1000 cycles of the training algorithm is performed. The coefficient of correlation between two random variables X and Y is [e.g. Ross, 2002]

$$\rho = \frac{cov(X, Y)}{\sigma_X^2 \sigma_Y^2} \tag{3.18}$$

with $cov(X, Y)$ the covariance between X and Y; and σ_X^2 and σ_Y^2 the variance of X and Y, respectively. The RMSE between variables $X = \{x_1, \ldots, x_N\}$ and $Y = \{y_1, \ldots, y_N\}$ is

$$\text{RMSE} = \sqrt{\frac{\sum_{i=1}^{N} (x_i - y_i)^2}{N}}. \tag{3.19}$$

The initialised model shows no positive correlation with R_{mp}: the correlation between O and R_{mp} is $\rho = -0.10$ and RMSE $= 1.97$. After just 50 cycles of training the output O closely matches R_{mp} with $\rho = 0.95$, RMSE $= 0.34$. The result does not improve much if the training is continued for more than 500 cycles. The correlation and RMSE after 500 cycles are $\rho = 0.98$ and RMSE $= 0.16$, and the output after 1000 cycles is almost identical, with $\rho = 0.99$ and RMSE $= 0.14$ (compare the dotted and red curves in Figure 3.6). The correlation coefficient and RMSE are also used to gauge the performance of the ANN models in Chapters 4 and 5.

The weights and biases in Table 3.1 may be used as arguments to equations 3.17a – 3.17c to calculate the output parameter O. The trained network (after 1000 cycles) may be written as:

$$O = \{1 + \exp[7.96364 H_1 + 4.03191 H_2 - 9.49954]\}^{-1} \tag{3.20a}$$

$$H_1 = \tilde{} \left[1 + \exp\left[0.36229\left(\left(V_{sw}\right) + 0.79265\right) - 16.17579\left(\left(N_p\right) + 0.16497\right) - 17.62448\right]^{-\tilde{}}\right]^{-1} \tag{3.20b}$$

$$H_2 = \tilde{} \left[1 + \exp\left[-1.43594\left(\left(V_{sw}\right) + 0.79265\right) - 1.60631\left(\left(N_p\right) + 0.16497\right) - 2.83232\right]^{-\tilde{}}\right]^{-1} \tag{3.20c}$$

The brackets $(\cdot)$ denote normalisation to $[-1, 1]$.

The method discussed here is applied to the modelling of pulsation intensity based on solar wind parameters in Chapters 4 and 5. In Chapter 4 the Neural Network toolbox from MATLAB is used to simulate the networks and perform the training. Due to computer memory restrictions, SNNS is preferred in Chapter 5.

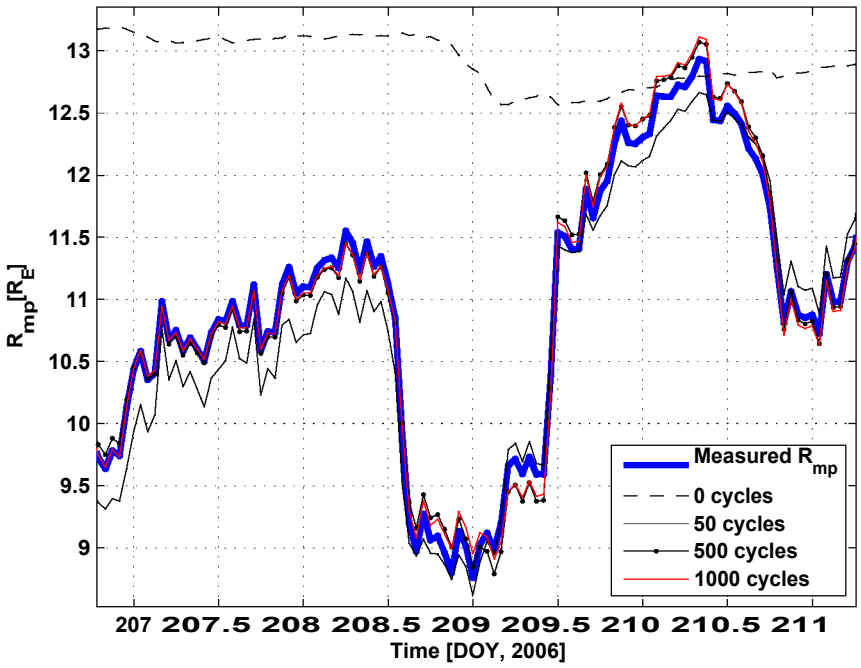

Figure 3.6: Predicted $_{R,np}$ with the initialised (random) weights and biases (0th cycle), and at 50, 500, and 1000 cycles of the training algorithm. $_{R,np}$ is predicted for day 207 till day 210 of 2006. This data was not included in the training or testing data sets.

Table 3.1: Weights and biases of the ANN at various stages (initialisation – 0 cycles, 50, 500, and 1000 cycles) of training. See Figure 3.3 for the layout of the network.

(a) The bias of each node at various stages of training.

cycles	b_{I_1}	b_{I_2}	b_{H_1}	b_{H_1}	b_O
0	-0.34262	0.03810	0.24861	-0.42573	-0.86053
50	-0.92349	0.89283	6.01584	-0.36557	1.78491
500	0.70095	0.17333	13.94675	-2.15979	4.80636
1000	0.79265	0.16497	17.62448	2.83232	9.49954

(b) The weight of each connection at various stages of training.

cycles	$w^{(1)}_{1,1}$	$w^{(1)}_{1,2}$	$w^{(1)}_{2,1}$	$w^{(1)}_{2,2}$	$w^{(2)}_{1,1}$	$w^{(2)}_{2,1}$
0	-0.86110	0.13080	0.45550	0.54531	0.90665	-0.08225
50	-0.18329	-1.53992	5.59736	0.55357	-5.39377	3.10846
500	-0.44808	-1.22136	12.62363	-0.95468	-7.74833	5.04576
1000	-0.36229	1.43594	16.17579	1.60631	-7.96364	-4.03191

Chapter 4

A Low Resolution Pc3 – Solar Wind Model

4.1 Introduction

The relationship between solar wind plasma and IMF parameters has been studied by various authors from the early 1960's [for example Saito, 1964; Bol'shakova and Troitskaya, 1968; Yumoto et al., 1984; Kovner and Feldstein, 1973]. Most of these authors used linear correlation coefficients between sets of solar wind and Pc3 data to study the solar wind control of Pc3 activity.

Due to the complex nature of the processes involved in the generation, propagation and transmission of ULF energy a more sophisticated approach to the analysis of the solar wind – Pc3 system is required. This chapter describes the development of an empirical model that predicts pulsation activity at a location on the Earth's surface from solar wind plasma and IMF measurements. The model is based on a feed forward neural network with solar wind, IMF and local time parameters as input and an indicator of pulsation intensity as output. Various input parameters are tested for their influence on model accuracy by training and evaluating a number of networks over identical data sets and training parameters. Through this process a number of optimal input parameters are identified from a larger set of candidate inputs. Data employed in the development of the model are in situ solar wind and horizontal component geomagnetic field measurements taken during 2002 and 2003.

The development of the neural network based model presented in this chapter is published in section 4.4 of Heilig et al. [2010]. This paper describes the modelling of pulsation intensity (through the pulsation index $Pc3_{ind}$) by a linear regression method (this part of the

paper is written by B. Heilig) and a neural network. The two models are compared and the implications of the solar wind parameters that are used as input are discussed in the paper.

4.2 Data Sources

4.2.1 Solar Wind Measurements from OMNI

Solar wind data used in this investigation are collected by several spacecraft located upstream of the Earth. The data is processed and published as OMNI data sets at various time averages (1 minute, 1 hour, and 27 days) through the OMNIWeb interface at http://omniweb.gsfc.nasa.gov. One hour averages of solar wind data, collected during 2002 and 2003, from the OMNI-2 data set have been used for the work presented in this chapter.

The OMNI data is sourced from various spacecraft including the Advanced Composition Explorer (ACE), Wind, and Geotail. Most measurements were taken by ACE (349199 data points at 1-minute resolution), and 95127 measurements from Wind are used. The locations (in GSE coordinates) of ACE and Wind where the measurements are taken during 2003 are plotted in Figure 4.1 (in blue for ACE and red for Wind). The Geocentric Solar Ecliptic (GSE) coordinate system is an orthogonal set of three axes (x_{GSE}, y_{GSE}, z_{GSE}), with its origin at the Earth. The $_{xGSE}$ axis connects the Earth and the Sun, with positive x pointing towards the Sun. Positive $_{yGSE}$ points toward dusk in the ecliptic plane, and $_{zGSE}$ completes the orthogonal set of axes. ACE orbits the first Lagrangian point (L1) at $x_{GSE} \approx 225\ R_E$, with $R_E = 6367.5$ km. The average solar wind flow speed toward the Earth is 450 km.s^{-1} (Table 2.3); at this speed a parcel of solar wind plasma takes about 53 minutes to travel from ACE (at $x_{GSE} = 225\ R_E$) to the bow shock nose (approximately at $x_{GSE} = 10\ R_E$). To account for the time delay 1-minute spacecraft measurements are shifted in time up to the nose of the bow shock. The shifted data set then represents the state of the solar wind plasma and magnetic field parameters just upstream of the bow shock. Calculations of the time delay magnitude are based on (i) the location of the spacecraft with respect to the Earth when the measurement is taken; (ii) the velocity vector of the solar wind at that time; (iii) the phase fronts of solar wind variation. More information on the processing and shifting of data for the OMNI-2 data sets is available at http://omniweb.gsfc.nasa.gov/html/omni2_doc.html.

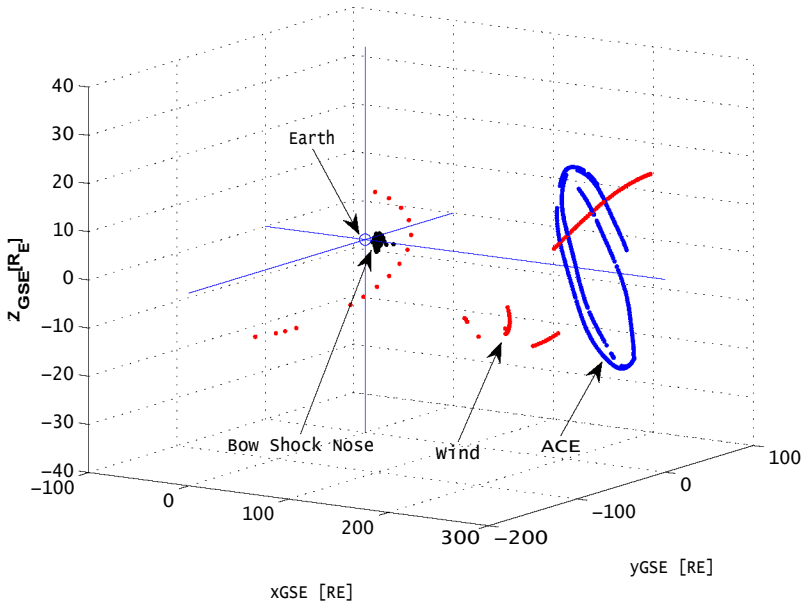

Figure 4.1: Positions of ACE (blue) and Wind (red) spacecraft where measurements are taken during 2003. The Earth is located at the origin and the location of the bow shock nose throughout the year is also indicated (black points).

4.2.2 Pc3 Observations

Geomagnetic data are measured at the THY (Tihany, Hungary) Intermagnet (http://www.intermagnet.org/) station by a fluxgate magnetometer with 1 Hz sampling rate in pico Tesla (pT); 1 pT = 10^{-12} T. THY has geographical coordinates (46.90^0 N, 17.89^0 E) and geomagnetic coordinates (42.44^0 N, 92.39^0 E), according to the altitude adjusted corrected geomagnetic model (AACGM) [Baker and Wing, 1989], calculated using the international geomagnetic reference field (IGRF) of 2001 [Peddie, 1982].

THY is a middle latitude ground station and lies at L = 1.84. Waters et al. [1991] introduced the crossphase technique to measure field line resonant frequencies based on measurements from two meridional stations. The method relies on the calculation of the crossphase spectrum of Pc3 pulsations measured at the two stations. According to this work the eigenfrequencies of a field line at L_{sas} 1.8 is 50 mHz (+- 2 mHz). This places FLR related oscillations at THY in the range of Pc3 pulsations, indicating that the pulsations measured at THY will include both FLR and upstream wave generated Pc3 activity (ULF waves travelling directly into the inner magnetosphere from the foreshock region; see Figure 2.6).

4.3 Input and Output Parameters

In this section the input and output parameters, and the data sets employed in the development of the neural network based model are described. The linear relationships between pairs of input and output parameters, quantified by a correlation coefficient, are also discussed.

4.3.1 Input Parameters

Seven solar wind plasma and IMF parameters are used to study the solar wind – Pc3 relationship. The parameters are based on the in situ measurements in the OMNI-2 data set. The solar wind based parameters are listed with units of measurement in Table 4.1. The candidate inputs (seven solar wind and two local time parameters) are selected based on the observations discussed in Chapter 2.6. Pulsation amplitude correlates positively with high solar wind speed (V_{sw}) [e.g. Saito, 1964; Heilig et al., 2007] and small cone angle (ϑ_{Bx}) [e.g. Kovner et al., 1976], and the frequency of the pulsations are related to IMF magnitude (B_{IMF}) [Bol'shakova and Troitskaya, 1968].

Table 4.1: Solar wind-based input parameters used in the model development. Each parameter is measured in the units listed in the third column and defined by the equation numbers listed in the last column.

Symbol	Description	Unit	Eqn.
V_{sw}	Bulk solar wind speed	$km.s^{-1}$	–
B_{IMF}	Magnitude of magnetic field	nT	(4.2)
ϑ_{Bx}	Angle between IMF and Sun-Earth line (x_{GSE})	$^{\circ}$	(2.35)
N_p	Solar wind proton number density	cm^{-3}	–
P_d	Dynamic solar wind pressure	nPa	(4.4)
R_{mp}	Magnetopause stand-off distance from the Earth	R_E	(2.29)
M_A	Alfvénic Mach number	–	(2.20)
hrs	Sine of UT decimal hour of the day	–	(4.5a)
hrc	Cosine of UT decimal hour of the day	–	(4.5b)

Cone angle is calculated by equation 2.35 from the magnetic field measurements listed in the OMNI-2 set. Measurements of the IMF are made in the GSE components of the field

$$\mathbf{B_{IMF}} = B_x\hat{\mathbf{x}}_{\mathbf{GSE}} + B_y\hat{\mathbf{y}}_{\mathbf{GSE}} + B_z\hat{\mathbf{z}}_{\mathbf{GSE}} \tag{4.1}$$

and the magnitude is

$$B_{IMF} = \sim B_x^2 + B_y^2 + B_z^2. \tag{4.2}$$

Field components and total magnitude in the OMNI-2 set are measured in nT and rounded to single decimals. Using the listed B_{IMF} values (that are rounded to single decimals) introduces an error into ϑ_{Bx} calculations that is especially visible at low ϑ_{Bx}. Figure 4.2 depicts the distribution of ϑ_{Bx} calculated by using B_{IMF} from the OMNI-2 set (bars) and the distribution of ϑ_{Bx} calculated using $B_{IMF} = \sim B_x^2 + B_y^2 + B_z^2$ with the component values as listed in OMNI-2 (red squares). Some values of B_x/B_{IMF} near 1 are mapped to 1 because of the restriction of the OMNI-2 B_{IMF} to a single decimal, resulting in the mapping of some $< 10^0$ cone angles to 0^0, since $\cos(10^0) = 0.9848$ sas 1 and $\cos(x) \dashrightarrow 1$ for $x \dashrightarrow 0^0$. Consequently the total IMF used in the calculation of ϑ_{Bx} and in the rest of the modelling is computed by equation 4.2 and the OMNI-2 values of B_{IMF} are not used.

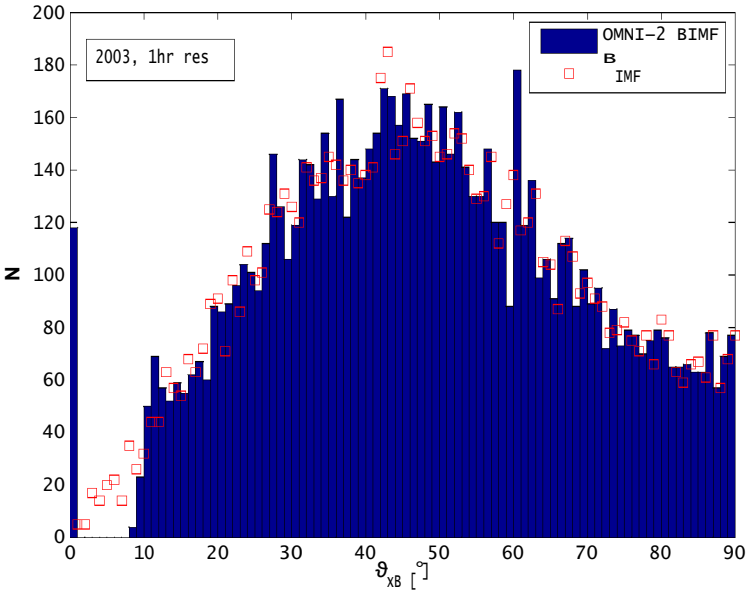

Figure 4.2: The error introduced by using B_{IMF} rounded to a single decimal in the calculation of ϑ_{Bx}. Blue bars denote the distribution of ϑ_{Bx} when the rounded B_{IMF} from the OMNI-2 dataset are used. Red squares indicate the distribution of ϑ_{Bx} when the correct values of B_{IMF} are used. Rounded B_{IMF} results in $\vartheta_{Bx} < 10^0$ being mapped to 0^0.

Proton density in the solar wind (N_p) and three density-related input parameters are added to the set of candidate inputs. The magnetopause stand-off distance $_{(Rmp)}$ from the Earth de-

termines the distance propagated by incoming waves into the magnetosphere. It is approximated by equation 2.29, with solar wind speed and density measurements (N_p and V_{sw}) from OMNI-2. The Alfvénic Mach number M_A is the ratio between the Alfvén and solar wind speed (see section 2.4) and is approximated by

$$M_A = \frac{V_{sw}\sqrt{N_p}}{20 B_{IMF}} \tag{4.3}$$

as part of the OMNI-2 set. The size of the magnetosphere is largely determined by the pressure exerted by the incoming solar wind on the geomagnetic field; the solar wind dynamic flow pressure is part of the OMNI-2 set and is calculated in nPa from the proton density, solar wind speed, and the ratio (N_a/N_p) between alpha particles (H+) and protons:

$$P_d = 1.67 \times 10^{-6} N_p V_{sw}^2 (1 + 4 N_a/N_p). \tag{4.4}$$

Two time-based parameters are utilised to model the diurnal variation in Pc3 activity. The sine and cosine of the hour of the day, in Universal Time (UT)

$$hrs = \sin\left(2\pi \frac{hr}{24}\right) \tag{4.5a}$$

$$hrc = \cos\left(2\pi \frac{hr}{24}\right) \tag{4.5b}$$

are used as a periodic pair of input parameters. Employing hrs and hrc as a pair of inputs is equivalent to using the linear combination $a\,hrs + b\,hrc$ as a single input, with a and b the weights determined by the training algorithm. As the goal of the training algorithm is to minimise the error between predicted and measured output, a and b will be adapted by the algorithm to optimally reproduce the periodic component of $Pc3_{ind}$.

4.3.2 Output Parameter

In this thesis the intensity of Pc3 pulsations is measured by the Pc3 pulsation index [Heilig et al., 2010], defined as the root-mean-square of Pc3 bandpass filtered H-component of the geomagnetic field magnitude:

$$Pc3_{ind} = \frac{1}{N}\sum_{i=1}^{N} H_{Pc3}^2 \tag{4.6}$$

where $_{HPc3}$ is a series of N H component data filtered in the Pc3 band. In this chapter data sets of 1-hour $_{Pc3_{ind}}$ averages are used, and in chapters 5 and 6 $_{Pc3_{ind}}$ data at 1-minute resolution are utilised.

4.3.3 Data Set Selection

In this section the construction of the training, testing and evaluation data sets employed in the development of the neural network models is discussed. During geomagnetically active periods the ULF frequency band (including the Pc3 band) is flooded with perturbations that are due to the storm activity. Therefore active periods are excluded from the data sets employed in the model development. The planetary K-index (K_p) is a scale of global geomagnetic activity (see Mayaud [1980], for example) that indicates the geomagnetic activity for 3-hour intervals on a scale of thirds, between 0 and 9 for a total of 28 possible values:

$$K_p = \{0_0, 0+, 1-, 1_0, 1+, 2-, 2_0, 2+, \ldots, 8-, 8_0, 8+, 9-, 9_0\}.$$

Only hours where $K_p < 4_0$ (i.e. geomagnetically quiet periods) are included in the data used in the development of the neural network model.

Data spanning 2003 (day 1 to day 365) are used to construct the testing and training data sets. Out of the 8243 error-free hourly averages in the year, 6551 are identified as $K_p < 4_0$ (Table 4.2). The testing data set is constructed by randomly selecting 30% of this combined set, while the remaining 70% forms the training data set. The evaluation set contains data from 2002 collected from day 76 to 105. Out of 678 hours of error-free data, 639 hourly averages of input and output parameter data comprise the evaluation data set (Table 4.2).

Applying the $K_p < 4_0$ limit to the solar wind and $_{Pc3_{ind}}$ data changes the distribution of the observed parameters. The original and reduced $_{Pc3_{ind}}$ data sets for 2003 and 2002 (day 76 to 105) are summarised in Table 4.2. The number of data points, 10th, 50th (median), and 90th percentiles, and normalised variance (last column) is listed for the entire set, and for the restricted (only $K_p < 4_0$) set. The k-th percentile P_k of $\mathbf{x} = \{x_1, x_2, \ldots, x_N\}$ is the value x_k below which k% of the values in the set $\mathbf{x}$ lies. The minimum of $\mathbf{x}$ is P_0, since there are no values smaller than P_0, the median is $_{P_{50}}$ (half the set is larger than $_{P_{50}}$ and the other half is smaller), and the maximum is $_{P_{100}}$, since $x_i < P_{100}$, $\forall i \in [1, N]$. The reduced set of observations

is shifted to slightly smaller values of $Pc3_{ind}$ as P_{10}, P_{50} and P_{90} decrease when active periods are excluded. The normalised variance (σ^2/N) of the $K_p < 4_0$ set is also slightly smaller due to the reduced activity (see Table 4.2).

Table 4.2: Summaries of all hourly averages of $Pc3_{ind}$ and the reduced sets where only hours with $K_p < 4_0$ are considered. The total number of data points (N), 10th, 50th and 90th percentiles, and the normalised variance (σ^2/N) are calculated for both sets.

criteria (2002, day 76 to 105)	N	P_{10}	P_{50}	P_{90}	σ^2/N
All	678	7.20	28.77	142.88	11.63
$K_p < 4_0$	639	7.09	26.20	130.34	9.91
criteria (2003)	N	P_{10}	P_{50}	P_{90}	σ^2/N
All	8243	14.69	53.64	197.34	1.08
$K_p < 4_0$	6551	13.30	46.97	176.41	1.05

The pulsation index is plotted for 2002 (day 75 to 105) in Figure 4.3(a), and for 2003 in Figure 4.3(b). Hours with $K_p > 4_0$ are indicated with red points. Figure 4.4(a) shows the distribution of all $V_{su,}$ data collected during 2003 (blue curve), and the distribution of $V_{su,}$ during 2003 when only $K_p < 4_0$ data are considered (red curve). In Figure 4.4(b) the distribution of $Pc3_{ind}$ is plotted for all of 2003, and only $K_p < 4_0$, in red and blue step-like curves, respectively. Both distributions of $Pc3_{ind}$ and $V_{su,}$ are slightly skewed toward smaller values when instances of $K_p > 4_0$ are excluded. This is expected, as geomagnetic activity is usually accompanied by increased solar wind activity due to CME's or coronal holes. Furthermore, the data was recorded in 2003, at the peak of the previous solar cycle, when very large CME's (leading to very high $V_{su,}$) were observed. Note that in the restricted set of solar wind speed data (red curve, Fig. 4.4(a)) no observation of $V_{su,} > 900$ km.s^{-1} is made, while the unrestricted data set (blue curve, Fig. 4.4(a)) has hourly averages of over 1100 km.s^{-1}. The effect of restricting observations to $K_p < 4_0$ is also visible in the distribution of recorded $Pc3_{ind}$. Excluding $K_p > 4_0$ from the set of data also excludes the highest observations of $V_{su,}$ from the set, which, in turn, excludes the larger values of $Pc3_{ind}$. The fraction of data at the low end of the observed range ($Pc3_{ind}$ N 100 pT) is significantly higher when active times are excluded. This agrees with other studies [e.g. Saito, 1964; Heilig et al., 2010] that state the positive correlation between $V_{su,}$ and pulsation amplitude.

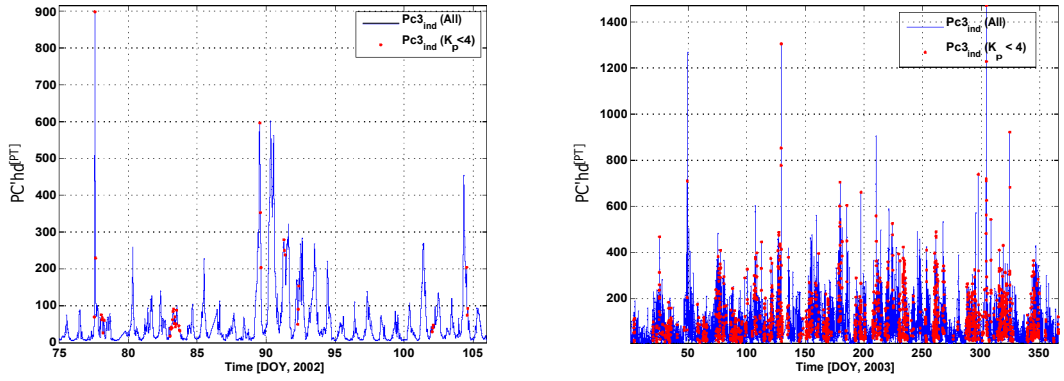

(a) 2002 (b) 2003

Figure 4.3: Observed $Pc3_{ind}$ during (a) 2002 (day 76 to 105) and (b) 2003. Hours where $K_p \geq 4_0$ are indicated in red.

4.3.4 Correlation Between Parameters

The set of solar wind-based parameters described above are all measurements of the same body of solar wind plasma. Hence it is expected that some degree of correlation exists between pairs of these parameters. Furthermore, the selection of parameters are based on known relationships between solar wind and IMF parameters and Pc3 activity. To this end the correlation coefficient (equation 3.18) between pairs of parameters is computed.

Table 4.3: Correlation between all pairs of candidate input parameters and $Pc3_{ind}$ over the combined training and testing datasets. Numbers in boldface indicate those correlations that are significant in the 99% confidence level.

	V_s	B_{IMF}	N_p	P_d	M_A	$\#_{Bx}$	R_{mp}	hrs	hrc	$Pc3_{ind}$
V_s	1	**-0.1618**	**-0.4679**	0.0282	**0.1059**	**-0.1482**	**-0.1581**	-0.0087	-0.0028	**0.4305**
B_{IMF}	**-0.1618**	1	**0.2289**	**0.2471**	**-0.6440**	**0.1284**	**-0.1175**	-0.0037	0.0045	**-0.0784**
N_p	**-0.4679**	**0.2289**	1	**0.7820**	**0.2528**	**0.1555**	**-0.5902**	-0.0234	0.0113	**-0.1055**
P_d	0.0282	**0.2471**	**0.7820**	1	**0.3002**	**0.1023**	**-0.8126**	-0.0285	0.0086	**0.1515**
M_A	**0.1059**	**-0.6440**	**0.2528**	**0.3002**	1	-0.0205	**-0.3808**	-0.0105	0.0013	**0.1200**
$\#_{Bx}$	**-0.1482**	**0.1284**	**0.1555**	**0.1023**	-0.0205	1	**-0.0897**	-0.0209	0.0230	**-0.3031**
R_{mp}	**-0.1581**	**-0.1175**	**-0.5902**	**-0.8126**	**-0.3808**	**-0.0897**	1	0.0212	0.0246	**-0.2361**
hrs	-0.0087	-0.0037	-0.0234	-0.0285	-0.0105	-0.0209	0.0212	1	0.0002	**0.1178**
hrc	-0.0028	0.0045	0.0113	0.0086	0.0013	0.0230	0.0246	0.0002	1	**-0.4769**
$Pc3_{ind}$	**0.4305**	**-0.0784**	**-0.1055**	**0.1515**	**0.1200**	**-0.3031**	**-0.2361**	**0.1178**	**-0.4769**	1

Table 4.3 lists the correlation between pairs of input and output parameters, over the combined set (2002, day 76 to 105, and 2003) of quiet time ($K_p < 4_0$) data; numbers in bold-face indicate correlations that are significant in the 99% confidence interval. For a correlation

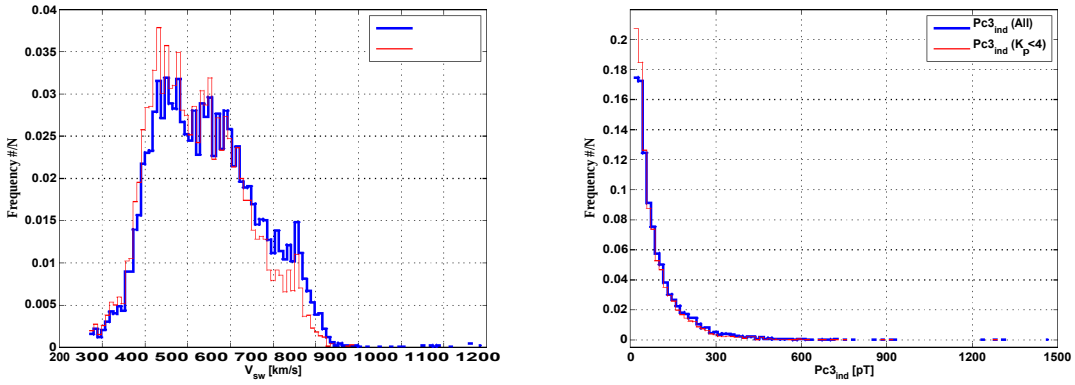

(a) $V_{su,}$ (b) $Pc3_{ind}$

Figure 4.4: The distributions of $_{Vsu,}$ (left) and $_{Pc3_{ind}}$ (right) data collected during 2003. The normalised frequency per interval of observation is plotted. Blue curves denote the distribution when all data is considered, and the red curves represent the distributions when only hours with $K_p < 4_0$ are included.

coefficient value to be considered significant, the probability of the null-hypothesis (which states that the two parameters have absolutely no relation) holding true must be small; it is less than 1% in this case. Firstly, there is no significant correlation between *hrs* or *hrc* and any solar wind based parameter. Of course this is expected; any significant correlation between universal time and solar wind activity would not be physically feasible. The absence of a significant correlation between P_d and $_{Vsu,}$ is interesting since the dynamic pressure is a function of velocity. However, this relation is purely quadratic (equation 4.4) and the correlation coefficient calculated is a measure of linear correlation between variables; hence it does not account for this non-linear dependence. The highest correlations are among three of the four density-related parameters ($_{(R,np}$, N_p, P_d) and two of the three IMF-related parameters ($B_{IM\,F}$, M_A). The $P_d - R_{,np}$ pair has a negative correlation of -0.8126, the highest correlation magnitude of all pairs. Since the dynamic pressure exerted by the solar wind on the magnetosphere directly determines the size of the magnetosphere, the location of the magnetopause $_{R,np}$ is dependent on P_d. This also explains the high correlation between $_{R,np}$ and N_p. Dynamic pressure, in turn, is determined by the density and velocity of the solar wind plasma ($P_d \sim NV^2$), as is made clear by the high correlation between P_d and N_p (0.7820). M_A is determined by the solar wind speed, density and IMF magnitude, and hence M_A has a high negative correlation with $B_{IM\,F}$ (-0.6440), and correlates to a lesser extent with N_p, $_{Vsu,}$ and P_d.

All correlations between the candidate inputs and the output parameter (last row / col-

umn in Table 4.3) fall within the 99% confidence interval. Solar wind speed and the cosine of the UT hour (hrc) yields the largest correlations with $Pc3_{ind}$, at 0.4305 and −0.4769, respectively. High solar wind speed ensures easier propagation of energy across the bow shock, magnetosheath and magnetopause into the magnetosphere [Potapov and Mazur, 1994]. Figure 4.5 clearly illustrates the dependence of $Pc3_{ind}$ on $V_{su,}$ during this interval. The increase in solar wind speed over the six days from day 88 to 94 of 2002 is clearly reflected in Pc3 activity as increased $Pc3_{ind}$. The lower panel of Figure 4.5 illustrates the local time dependence of Pc3 activity: $Pc3_{ind}$ peaks daily near $hrc = -1$, i.e. near local noon. The high negative correlation with the cosine of UT points to the predominantly daytime occurrence of Pc3 activity, and alludes to the propagation of ULF energy from the bow shock into the magnetosphere, since it is the day side of the Earth facing the incoming solar wind. The four density-related parameters have smaller (though significant at 99% confidence) correlations with $Pc3_{ind}$ (N_p: −0.1055, $_{Rmp}$: 0.1515, M_A: 0.1200, P_d: −0.2361). This might suggest that solar wind density plays a more non-linear role in the generation of Pc3's.

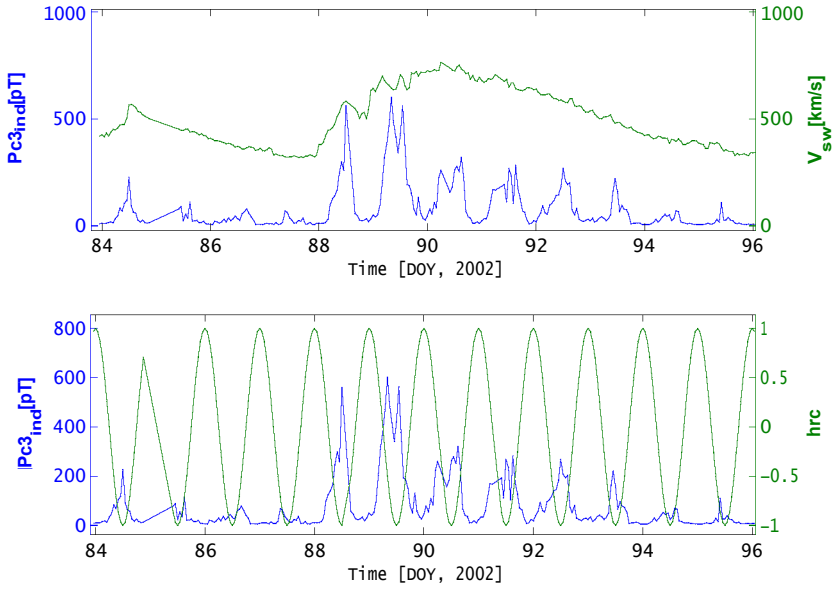

Figure 4.5: Solar wind speed (upper panel) and cosine of UT hour (lower panel) plotted against $Pc3_{ind}$. The dependence of $Pc3_{ind}$ on $V_{su,}$ and hrc is clear.

4.4 Neural Network Model Development

To enable a neural network model to predict pulsation intensity due to fluctuations in solar wind parameters, the choice of input parameters is critical. In the previous section a number of candidate input parameters are selected. The aim in this section is to obtain the subset of those candidate inputs that will optimally predict $Pc3_{ind}$. The quality of the prediction achieved and the set of input parameters that enable it could indicate the preferred generation mechanism of terrestrial Pc3 pulsations. In this chapter two metrics are used to gauge model performance by comparing measured and predicted output: the correlation coefficient (equation 3.18) and the root mean square error (RMSE, equation 3.19).

4.4.1 Neural Network Wrapper

A robust development process is used to identify the set of input parameters that best reproduce the observed output. The "wrapper" employed here is simply a process whereby many models are evaluated and the best performing one selected [e.g. Kim et al., 2005]. Initially a set of N candidate input parameters are identified. N identical neural networks are trained under identical conditions (same training algorithm, number of cycles, learning parameter, etc.), except that each network has a different input candidate as its only input parameter. Each one of the N trained networks are evaluated for accuracy on the same evaluation set, and the input parameter corresponding to the most suitable model is identified as the first optimal input (I_a). This is the first round of training. In the second round of training each network has two input parameters – the first optimal input (I_a), and one of the remaining $N-1$ candidate inputs. The corresponding $N-1$ two-input networks are trained and evaluated, and a second parameter I_b is identified to form the optimal *pair* of inputs (I_a and I_b). In the third round $N-2$ networks are trained and evaluated, each with three input parameters, yielding (I_a, I_b, I_c). The fourth round of training evaluates $N-3$ networks, the fifth $N-4$, and so on. This process continues until all N candidates have been identified as optimal, or until no significant improvement in accuracy (due to the inclusion of additional input parameters) can be observed.

This process is applied to a number of feed-forward networks trained using the training, testing and evaluation data sets described in the previous section. The set of candidate input parameters utilised are identified in Table 4.1. Each network is a fully connected feed-forward network with N_I input parameters, a single hidden layer and a single output param-

eter $Pc3_{ind}$. The number of hidden nodes is determined by

$$N_H = 2N_I + 1 \tag{4.7}$$

Each network is trained using the standard back-propagation algorithm, and training continues until the errors in test predictions begin to diverge. Before training all input and output parameters are normalised. All hidden nodes have hyperbolic tangent activation functions, and the output activation is a pure linear function.

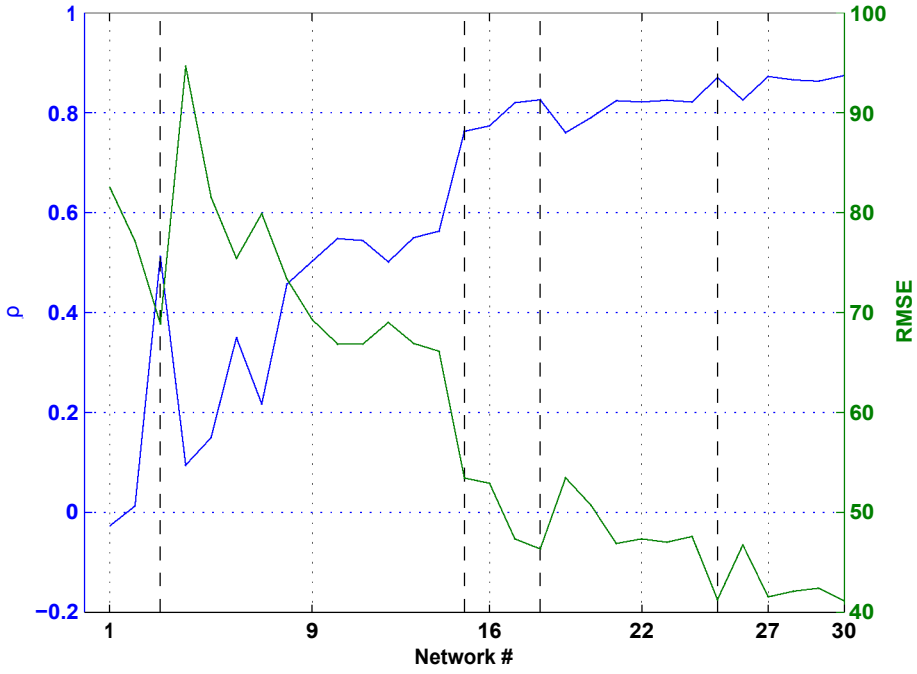

Figure 4.6: Correlation (blue) and RMSE (green) between measured and modelled $Pc3_{ind}$ as inputs are added according to the wrapper process. Network numbers on the x-axis indicate the start of a new round of training. Vertical dashed lines indicate the winner of each round of training. Also see Table 4.4.

Table 4.4 and Figure 4.6 illustrate the evolution of the wrapper process. Each network is trained with the input parameters marked with x's in Table 4.4, and the correlation between measured and predicted output is listed in the last column. The number of hidden nodes for each network is listed in the second column (N_H). In the last two columns of Table 4.4 the correlation ρ and root mean square errors are listed. The process commences with $N = 8$

networks each trained with one input parameter. Note the use of the pair $[hrs, hrc]$ as a single candidate input in the wrapper process; in neural network terms, however, hrs and hrc are separate input nodes.

In the first round of training the network with $_{Vsu,}$ as input achieves the best correlation and the lowest RMSE between measured and predicted $_{Pc3_{ind}}$ with $p = 0.51$ and RMSE = 68.87. Networks 8 and 6 produces the second and third best results, with ($p = 0.45$, RMSE = 73.34) and ($p = 0.34$, RMSE = 75.42), respectively. The second round of training tests networks with pairs of inputs and here network number 15, with $_{Vsu,}$ and $[hrs, hrc]$ as input, yields a correlation of 0.76 between measured and predicted output and RMSE = 53.44. The second best model is network 14 (inputs $_{Vsu,}$ **and** $_{R,np}$) with ($p = 0.56$, RMSE = 66.12).

After the third round of training (networks 16 – 21) three sets of input parameters yield near-equal performance in p and RMSE: (i) network 17, with $_{Vsu,}$ $[hrs, hrc]$, and N_p has $p = 0.8203$ and RMSE = 47.35; (ii) network 18, with input parameters $(_{Vsu,}$ $[hrs, hrc]$, $P_d)$ yields $p = 0.8261$ and RMSE = 46.33; (iii) network 21 with $(_{Vsu,}$ $[hrs, hrc]$, $_{R,np})$ has $p = 0.8258$ and RMSE = 46.74.

The three newly added input parameters are proton density N_p, and two of the density-related inputs ($_{R,np}$ and P_d). In terms of p the networks with $_{R,np}$ and P_d perform marginally better than network 17 (with N_p), but the RMSE of network number 17 is lower than that of network 21. Both $_{R,np}$ and P_d are directly related to the size of the magnetosphere, which may suggest that $_{Pc3_{ind}}$ is dependent on the degree of attenuation experienced by waves travelling from outside the magnetosphere (more attenuation should be observed over a larger magnetosphere). However, the choice of which parameter yields the best performance is somewhat ambiguous because the separation between the respective values of p and RMSE is so small. Nevertheless, P_d is identified as the third optimal input as model number 18 has the lowest RMSE and highest p. The small difference in performance of the three models is expected due to the high degree of correlation between N_p, $_{R,np}$ and P_d. Table 4.3 lists the correlations of 0.78, -0.59 and -0.81 between N_p and P_d, N_p and $_{R,np}$, and P_d and $_{R,np}$. Due to their similarity, the performances of networks 17, 18 and 21 are almost identical. The neural network models' sensitivity to the similarity between the three parameters (N_p, $_{R,np}$ and P_d) is revealed in the results following the fourth round of training: Networks with $_{R,np}$ and N_p as inputs do not improve the performance of network 18, as they offer no new information to a model which

already has P_d as an input. In this (fourth) round, it is network number 25 that yields the best prediction of $Pc3_{ind}$. This network adds cone angle (ϑ_{Bx}) to the optimal subset of inputs. After a fifth round of training (networks 27 to 30 in Table 4.4) it is concluded that none of the remaining parameters (B_{IMF}, N_p, M_A, $_{Rmp}$) can contribute to the model's performance, since no significant increase in accuracy is observed.

The model development results in a 5-input feed-forward network with 11 hidden nodes in one hidden layer and a single output. The optimal subset of candidate input parameters, as determined by the wrapper is

$$V_{sw}, [hrs, hrc], P_d, \vartheta_{Bx}.$$

Model accuracy, as determined by the correlation between measured and predicted $Pc3_{ind}$ over the evaluation data set is $\rho = 0.8706$ and RMSE = 41.2655. The roles of the input parameters are discussed in the next section.

Table 4.4: Evolution of the wrapper process. Inputs are iteratively added (denoted by x's) according to the performance of the associated network. The inputs yielding the optimum performance (indicated by p and RMSE) are highlighted in boldface. Also see Figure 4.6.

net	N_h	B_{IMF}	N_p	V_{sw}	P_d	M_A	V_{Bx}	R_{mp}	[hrs, hrc]	p	RMSE
001	3	x								-0.0269	82.8127
002	3		x							0.0125	81.0426
003	3			x						**0.5125**	**68.8752**
004	3				x					0.0949	94.6694
005	3					x				0.1495	81.5524
006	3						x			0.3499	75.4256
007	3							x		0.2171	79.9142
008	5								x	0.4569	73.3498
net	N_h	B_{IMF}	N_p	V_{sw}	P_d	M_A	V_{Bx}	R_{mp}	[hrs, hrc]	p	RMSE
009	5	x		x						0.5029	69.2946
010	5		x	x						0.5482	66.8614
011	5			x	x					0.5440	66.8630
012	5			x		x				0.5013	69.0202
013	5			x			x			0.5500	66.9222
014	5			x				x		0.5629	66.1217
015	7			x					x	**0.7627**	**53.4467**
net	N_h	B_{IMF}	N_p	V_{sw}	P_d	M_A	V_{Bx}	R_{mp}	[hrs, hrc]	p	RMSE
016	9	x		x					x	0.7739	52.9169
017	9		x	x					x	0.8203	47.3541
018	9			x	x				x	**0.8261**	**46.3385**
019	9			x		x			x	0.7604	53.4569
020	9			x			x		x	0.7901	50.7318
021	9			x				x	x	0.8242	46.8888
net	N_h	B_{IMF}	N_p	V_{sw}	P_d	M_A	V_{Bx}	R_{mp}	[hrs, hrc]	p	RMSE
022	11	x		x	x				x	0.8217	47.3522
023	11		x	x	x				x	0.8250	47.0162
024	11			x	x	x			x	0.8215	47.5801
025	11			x	x		x		x	**0.8706**	**41.2655**
026	11			x	x			x	x	0.8258	46.7430
net	N_h	B_{IMF}	N_p	V_{sw}	P_d	M_A	V_{Bx}	R_{mp}	[hrs, hrc]	p	RMSE
027	13	x		x	x		x		x	0.8728	41.5396
028	13		x	x	x		x		x	0.8659	42.1073
029	13			x	x	x	x		x	0.8631	42.4169
030	13			x	x		x	x	x	0.8746	41.1251

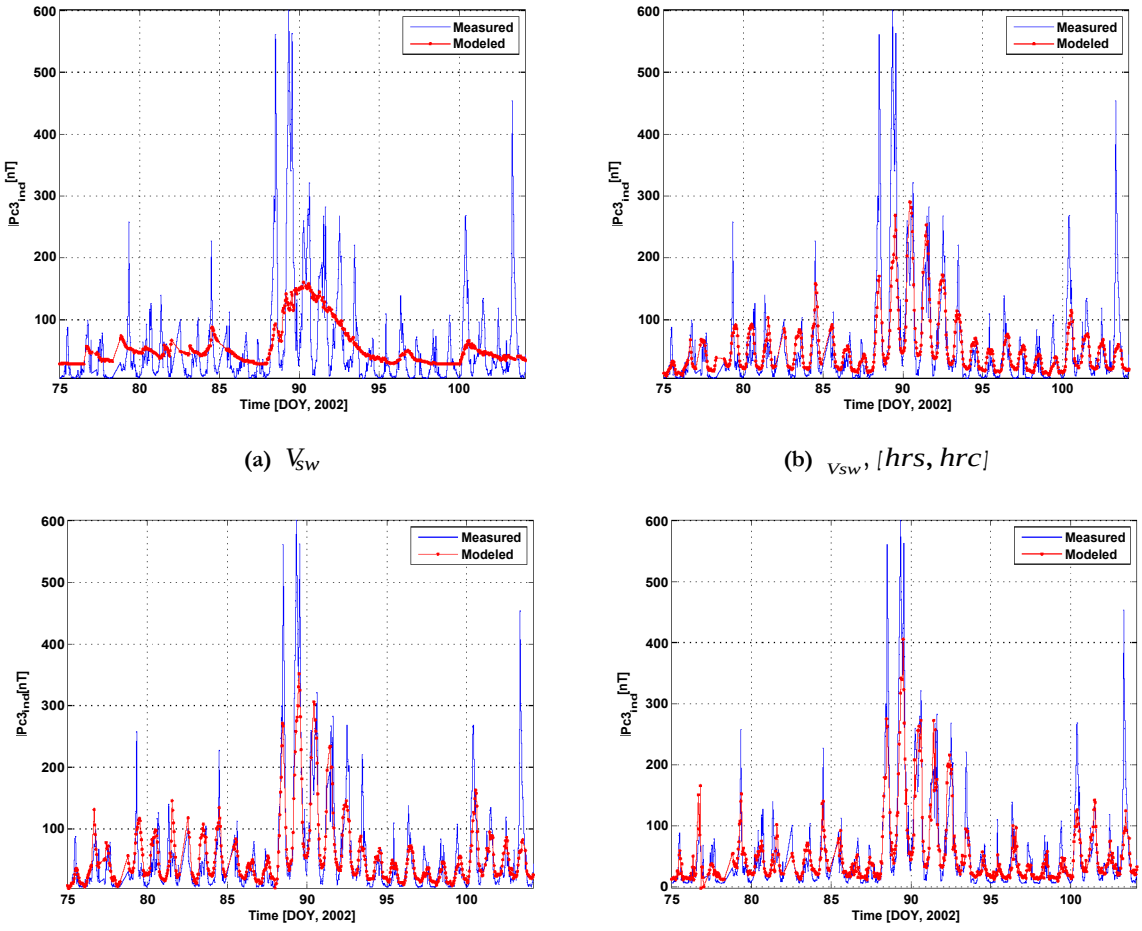

(a) V_{sw}

(b) $_{Vsw}$, $[hrs, hrc]$

(c) $_{Vsw}$, $[hrs, hrc]$, P_d

(d) $_{Vsw}$, $[hrs, hrc]$, P_d, $\boldsymbol{t}_{ax}$

Figure 4.7: The measured and predicted output from networks 3, 15, 18, and 25. As input parameters are added to the optimal set model performance clearly improves.

4.4.2 Results Analysis

The evolution of the model is illustrated in Figures 4.7 and 4.8. In each sub-figure of 4.7 the output from the winning model of each round of training is plotted against the measured output for a portion of the evaluation set. Figure 4.8 shows how the error distribution (histogram of errors) changes as inputs are added to the optimal set. The output of network 3 (Figure 4.7(a)) is only dependent on a single input parameter, $_{Vsw}$. In Figure 4.9 modelled $_{Pc3_{i,,d}}$ follows the gradual increase and decrease in solar wind speed over the same interval and does not react to the shorter time scale (less than ~ 1 day) variations in $_{Pc3_{i,,d}}$. The error distribution (top panel of Figure 4.8) peaks between −20 and −30 pT in a quasi-normal distribution

about the mean.

The inclusion of the time-based parameters (Figure 4.7(b)) enables the model to react to the diurnal variation in Pc3 activity. The increase in model performance is visible in the error distribution as the peak shifts toward 0 pT due to a decrease in the fraction of large negative errors (second panel of Fig. 4.8). The addition of P_d and ϑ_{Bx} to the set of input parameters yields a relatively small improvement in overall performance, but the modelling of the largest peaks are improved (compare Figure 4.7(b) with Figures 4.7(c) and 4.7(d)). Furthermore, the RMSE is reduced by the addition of P_d and ϑ_{Bx} and the error distributions of networks 18 and 25 (third and fourth panels of Figure 4.8) both become narrower, with larger peaks near 0, indicating a significant reduction in large errors.

The weights and biases computed by the training algorithm are listed in Appendix B for each of the four networks (3, 15, 18 and 25). These weights and biases, along with normalised input parameter measurements, maybe used as arguments to equations 3.6 and 3.5 to reproduce the networks and make predictions using other sets of input data.

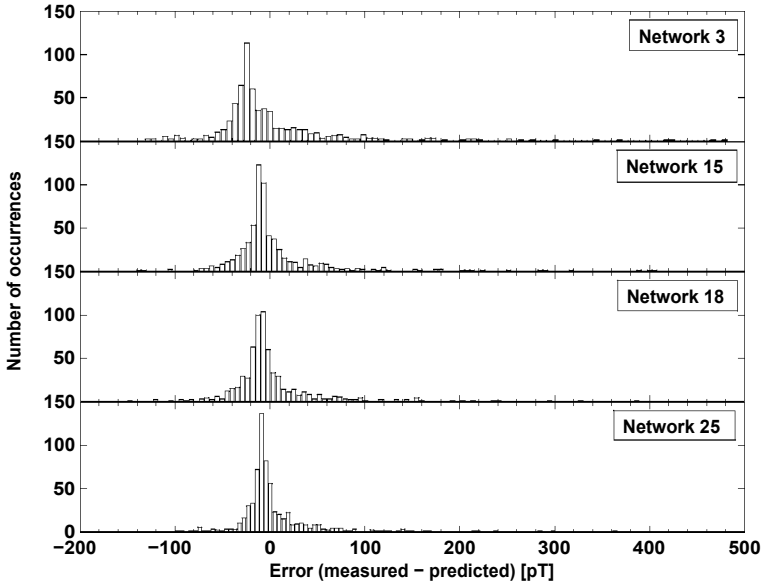

Figure 4.8: Error distributions of the predicted output from networks 3, 15, 18 and 25. Errors shift toward narrower Gaussian distributions as model performance increase.

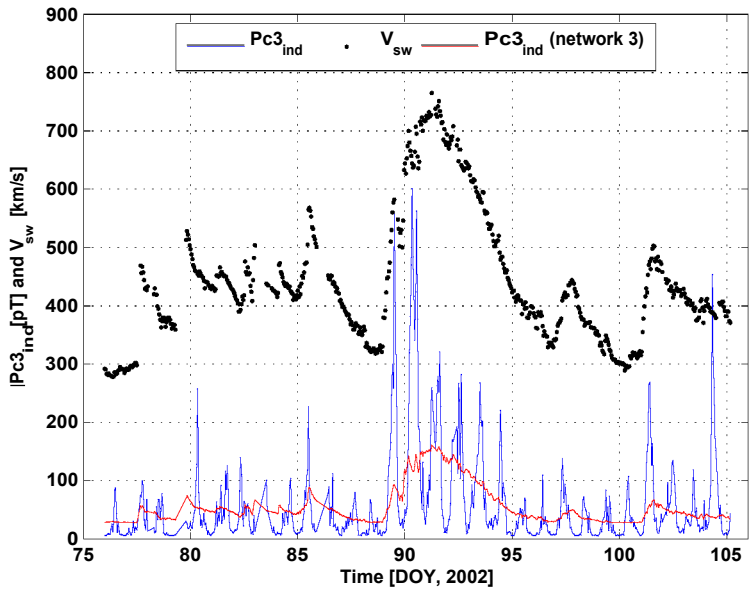

Figure 4.9: Solar wind speed and measured and predicted (from network 3) $Pc3_{i,,d}$ plotted for the evaluation data set.

4.5 Discussion

In this chapter a neural network based model of the relationship between solar wind plasma and magnetic field measurements, taken upstream of the magnetosphere and adapted for solar wind flow up to the bow shock nose, is developed. The model is developed by a robust iterative process that selects and ranks the most influential subset of input parameters from a larger set of candidates. Prediction performance is gauged by the correlation coefficient and the RMSE, with the most accurate model predicting $Pc3_{i,,d}$ with $\rho = 0.8706$ and RMSE = 41.2655. The highest $Pc3_{i,,d}$ peaks in the evaluation data set are under estimated. This is due to the relative rarity of values over 300 pT in the measured data (see Figure 4.4(b)). The optimal set of input parameters are $_{Vsw}$, $[hrs, hrc]$, P_d and ϑ_{Bx}. The results of previous studies [e.g. Saito, 1964; Bol'shakova and Troitskaya, 1968; Wolfe et al., 1980] are in agreement with the selection of $_{Vsw}$ and ϑ_{Bx}, as they note the correlation between these parameters and Pc3 amplitude. Furthermore, it is confirmed that Pc3's are predominantly day side phenomena as is shown by the marked increase in model performance with the addition of $[hrs, hrc]$ to the set of inputs.

Three density-related parameters included in the set of candidates yield near-equal model

performance, suggesting that any one of N_p, $_{Rmp}$ or P_d could be employed in the model. The dependence of $_{Pc3_{ind}}$ on density is especially clear during intervals where the density N_p in the solar wind is extremely low. Such a low density event (LDE) and the neural network model's response is discussed here. Figure 4.10 shows the reaction of measured and modelled $Pc3_{ind}$ (blue and red curves, top panel) to the LDE, with N_p and P_d plotted in the bottom panel of the figure; $_{Vsu,}$ ^{and} ϑ_{Bx} are plotted in the second and third panels, respectively.

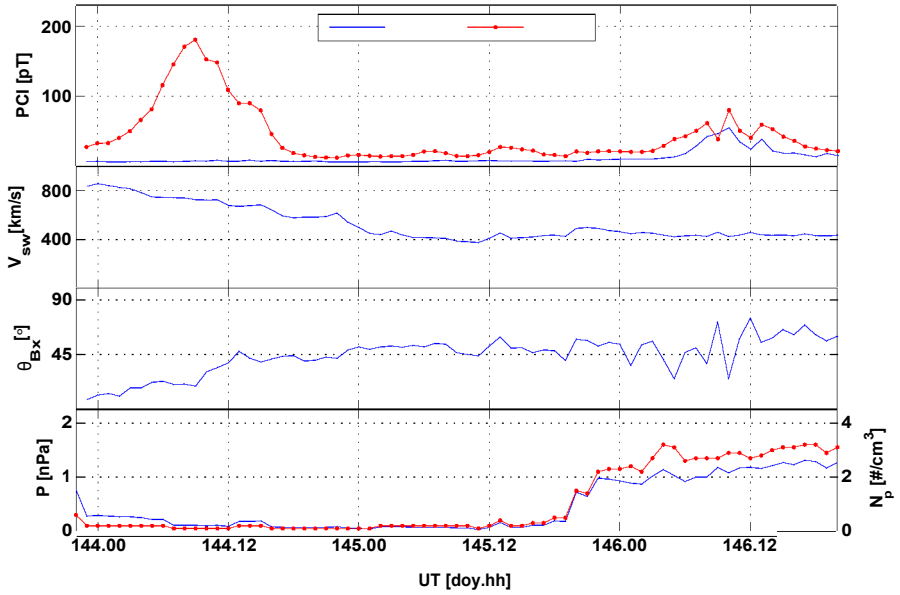

Figure 4.10: Measured and predicted $Pc3_{ind}$ is plotted for an interval of low solar wind density (top panel). Solar wind speed (second panel), cone angle (third panel) and P_d (blue curve, bottom panel) and N_p (red curve, bottom panel) are plotted for the same period.

During day 144 and 145 of 2002 the proton density in the solar wind is extremely low, below 1 cm^{-3} for the majority of the 48 hours. While N_p N 1 cm^{-3} on day 144 and 145, the pulsation index is extremely low: $_{Pc3_{ind}}$ N 10 pT, near the noise level of the magnetometer (6 – 7 pT RMS) [Heilig et al., 2010]. During this interval the pulsation index does not react to normally favourable conditions. $_{Pc3_{ind}}$ remains near 10 pT while high solar wind speed (400 km.s^{-1} N $_{Vsu,}$ N 850 km.s^{-1}) and a favourable orientation of the IMF ($_{\vartheta_{Bx}}$ N 50°) is observed; even the usual diurnal variability, where $_{Pc3_{ind}}$ peaks near local noon, is not observed. The model reacts positively to the favourable $_{Vsu,}$ ^{and} ϑ_{Bx} conditions on day 144 and predicts moderate $_{Pc3_{ind}}$, peaking near noon; no reaction to the low level of N_p is visible.

On day 145, when the conditions are slightly less favourable for the generation of Pc3's due to lower average $_{Vsu,}$ (about 400 km.s^{-1}) and higher ϑ_{Bx} ($\approx 50^{\circ}$) the model accurately predicts the constant low level of $_{Pc3_{ind}}$. Near 20:00 UT on day 145 an increase in density is observed and by 22:00 $N_p > 2$ cm^{-3} and remains above 2 cm^{-3} throughout day 146. On day 146 the model accurately resolves the observed activity, with the expected noon peak, and apparently reacting to lower $_{Vsu,}$ and higher ϑ_{Bx} by predicting lower $_{Pc3_{ind}}$ than for day 144.

The absence of Pc3 activity during intervals of low solar wind density, despite otherwise favourable conditions in the solar wind (high speed, radial IMF) suggests a breakdown in the generation or transmission mechanism(s) necessary for Pc3's to be observed on the ground. The influence of N_p on $_{Pc3_{ind}}$ is studied in detail in Chapter 6.

Chapter 5

A High Resolution Pc3 – Solar Wind Model

5.1 Introduction

In the previous chapter a neural network based model of the solar wind – Pc3 index relationship was developed. This model used input (solar wind) and output ($Pc3_{ind}$) data sets with measurements averaged over 60 minutes. The averaging smooths out much of the variability in the solar wind parameters and in the $_{Pc3_{ind}}$ data. Figure 5.1 illustrates the loss of detail due to the 1-hour averaging. In the hourly-averaged data the cone angle effect on Pc3 intensity is visible (small ϑ_{Bx} is favourable for higher $Pc3_{ind}$), but finer details, such as the decrease in $_{Pc3_{ind}}$ after a sudden increase in ϑ_{Bx} between 09:00 and 10:00 UT, is not clear at such low time resolution.

In this chapter a neural network-based model, tasked with predicting $Pc3_{ind}$ from a number of solar wind plasma and magnetic field parameters, is developed. Measurements of solar wind parameters at 1-minute resolution from the high-resolution OMNI (HRO) data set (available for download from ftp://nssdcftp.gsfc.nasa.gov/spacecraft_data/omni/high_res_omni/) are collected and their 5-minute running averages are used as input parameters to the model. To ease the modelling of the solar wind – $Pc3_{ind}$ system the 5-step running average of all input (solar wind and local time) and output ($_{Pc3_{ind}}$) parameters are calculated and used in the development of this model. Due to the short time scale employed the propagation time of perturbations from the upstream region to the Earth must be taken into account in order to model the causal relationship between upstream (solar wind) and downstream (Pc3) phenomena investigated here.

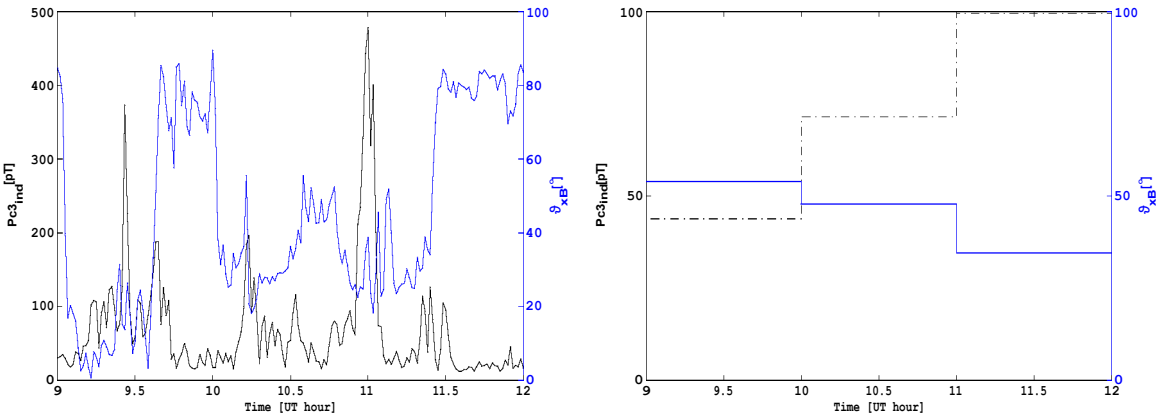

(a) 1-minute averages.

(b) Averaged over 60 minutes.

Figure 5.1: Minute (left) and hourly (right) averages of $Pc3_{ind}$ measured at THY, and ϑ_{Bx} from the OMNI-2 data set during day 166 of 2007. The cone angle effect on pulsation intensity, i.e. small ϑ_{Bx} results in increased Pc3 amplitude and vice versa, is visible on the 1-hour time scale but much of the finer detail is lost in averaging.

5.2 Wave Propagation Delay Time Through the Magnetosheath and Magnetosphere

The perturbations that cause pulsations of the Earth's field have to propagate from the upstream region across the magnetosheath and into the magnetosphere for Pc3's to be observed on the ground. To accurately model the relationship between upstream activity and pulsation intensity on the ground, the upstream data set is shifted in time with respect to the downstream data (ground measurements). The sets are shifted by the time (Δt) it takes for the perturbations upstream of the bow shock to propagate to the Earth where Pc3's are observed. The total delay time (in seconds) from a solar wind parameter measurement, made aboard a spacecraft (S), to a ground-based magnetometer measurement taken at THY is estimated in three parts (see Figure 5.2):

Δt_{SB} : Time from spacecraft (S) to bow shock nose (B).

Δt_{BM} : Time from bow shock nose to magnetopause (M).

Δt_{MG} : Time from the magnetopause to ground (G) observation.

Measurements from OMNI are shifted in time to account for the solar wind flow from the spacecraft position to the subsolar point on the bow shock nose; i.e. the HRO data set in-

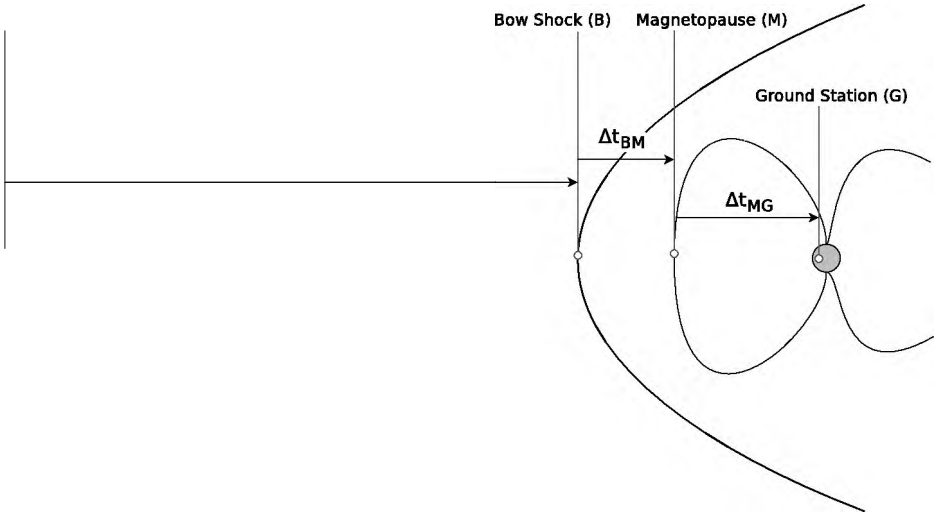

Figure 5.2: Propagation times from the solar wind to the Earth. The time from the spacecraft to the bow shock is Δt_{SB}, from the bow shock to the magnetopause is Δt_{BM}, and from the magnetopause to the Earth's surface (ground) is Δt_{MG}.

cludes the time delay Δt_{SB}. The HRO data set is used for all solar wind based measurements in this chapter, hence it is not necessary to estimate Δt_{SB} here.

According to Clausen et al. [2009] the propagation of compressional waves through the magnetosheath that drive pulsations in the magnetosphere can be calculated using the process described by Khan and Cowley [1999]. Propagation through the sheath is determined by sheath width, solar wind speed (V_{sw}), plasma flow speed into the magnetopause (V_{mp}) and the shock jump ratio

$$\alpha = \frac{(\gamma - 1)M_{ms}^2 + 2}{(\gamma + 1)M_{ms}^2}, \tag{5.1}$$

with $\gamma = 5/3$ and M_{ms} the magnetosonic Mach number. The magnetosonic Mach number is the ratio of solar wind to Alfvén and magnetosonic speeds

$$M_{ms} = \sqrt{\frac{V_{sw}^2}{V_A^2 + V_{ms}^2}} \tag{5.2}$$

The magnetosonic speed V_{ms} depends on the ratio of the thermal pressure P_{th} and particle density [Grocott et al., 2009]

$$V_{ms} = \sqrt{\gamma P_{th}/N_p}^{1/2} \tag{5.3}$$

Distance from the Earth to the bow shock nose is R_{bs}; this parameter is computed as part of the HRO data set. The distance to the magnetopause is approximated by equation 2.29. According to Khan and Cowley [1999] the propagation time (in seconds) through the sheath is

$$\Delta t_{BM} = \frac{R_{bs} - R_{mp}}{\alpha V_{sw} - V_{mp}} \log\left(\frac{\alpha V_{sw}}{V_{mp}}\right) . \tag{5.4}$$

The bulk speed of plasma flow into the pause V_{mp} is approximated [Khan and Cowley, 1999] as 20 km.s^{-1}.

It is assumed that the fast mode wave is responsible for carrying ULF energy through the magnetosphere at the Alfvén speed V_A toward the Earth [Clausen et al., 2009]. Burton et al. [1970] used measurements of the ion density and magnetic field in the magnetosphere to estimate V_A during a number of passes through the dawn quadrant of the magnetosphere. The OGO 5 spacecraft made a number of passes from the outer to the inner magnetosphere ($L \approx 12$ R_E to $L \approx 2$ R_E) in the equatorial plane; V_A was calculated for four passes on 7, 15, 17 and 22 April 1968 (see Figure 5.3). The means (dashed lines, Figure 5.3) of the V_A estimates are used to estimate average propagation times of fast mode waves in the magnetosphere. The mean Alfvén speed of each pass and the approximate magnetopause stand-off distance (equation 2.29) is used to estimate the magnetospheric propagation delay. Figure 5.4(a) depicts Δt_{MG} throughout 2007 for the lowest and highest V_A means (15 and 17 April 1968), $V_A = 1755$ km.s^{-1} and $V_A = 3341$ km.s^{-1}, respectively, and for the mean of all V_A estimates: $V_A = 2608$ km.s^{-1}. The delays range between 0.3 (17) and 1.2 (73) minutes (seconds), varying with R_{mp}. The average Alfvén speed ($V_A = 2608$ km.s^{-1}) is used to shift the $Pc3_{ind}$ data relative to the solar wind parameters. Since the pulsation index is calculated at 1 minute intervals, all pulsation data will be shifted by $T = \Delta t_{MG}/60$, rounded to integer minutes. This results in a shift due to magnetospheric propagation of 0 or 1 minute throughout 2007, and similarly for the rest of the data set (2002 – 2006).

The total delay to be applied to the HRO – THY data sets is $\Delta t = \Delta t_{BM} + \Delta t_{MG}$ and is plotted in Figure 5.4(b) for the year 2007; the delay ranges between 0 and 21 minutes. The minimum, mean and maximum Δt_{BM} for 2007 is 0, 4 and 20 minutes, respectively. All decimal minutes are rounded to the nearest integer. The delay Δt is mostly due to the propagation through the sheath, since the maximum Δt_{MG} is 1 minute. On day 13 of 2007 the solar wind density is below 1 cm^{-3} for most of the day, resulting in the expansion of the magnetosphere and magnetosheath. The magnetosheath width on this day is about 10 R_E, while the median

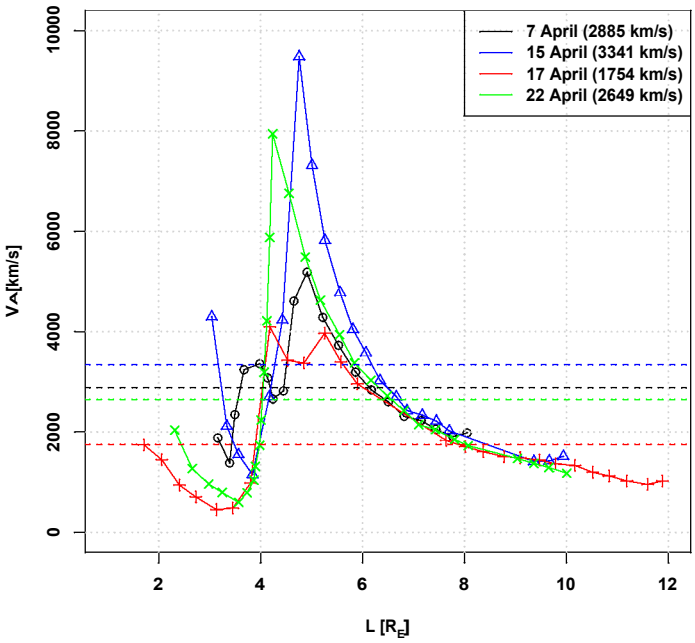

Figure 5.3: Alfvén speed calculated by Burton et al. [1970] at various L-shell values on 7, 15, 17 and 22 April 1968. Dashed lines indicate the mean of each curve.

sheath width for 2007 is approximately 2 R_E. It is the increase in magnetosheath width that causes the long (21 minute) propagation time delay on day 13. Figure 5.5 shows the time delay (left-hand side) and the sheath width (right) for days 10 to 16 of 2007.

5.3 Data Sets

The data used in the development of this model spans the interval from 2002 to 2007, at 1-minute cadence. The 1-minute measurements of all parameters are smoothed with a 5-minute running mean. The entire data set collected throughout the 6 year period is not utilised. Since Pc3 pulsations occur on the day side of the Earth [e.g. Le and Russell, 1994] only measurements taken during local (THY) day time are considered, reducing the size of the set by about 50%. The solar zenith angle χ indicates the angle between the line connecting an observer on the Earth's surface with the Sun and the zenith line. The angle is dependent on the time of day, the location of the observer on the Earth and the position of the Earth relative to the Sun. Seasonal and diurnal variations are captured by χ. The solar zenith angle changes

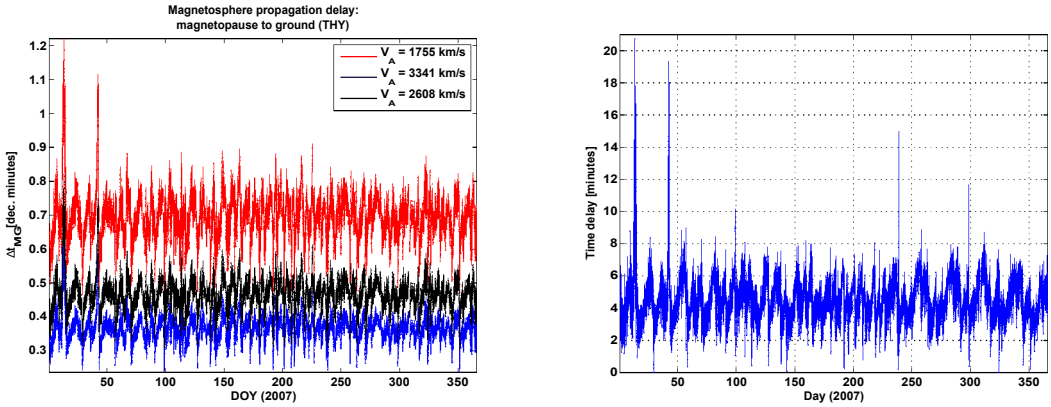

(a) Δt_{MG} (b) $\Delta t = \Delta t_{MG} + \Delta t_{BM}$

Figure 5.4: Time delay due to (a) magnetospheric propagation (Δt_{MG}), calculated for various average Alfvén speeds (left), and (b) the total delay time (Δt) calculated by adding the magnetosheath and magnetospheric delays.

throughout the day, from 90^0 at sunrise to a minimum value, that depends on the location and season, at noon, to values larger than 90^0 after sunset. Only data measured while $\chi < 90^0$ are included in the data sets utilised in this chapter. During geomagnetically active periods the Pc3 band is flooded with storm activity driven by mechanisms other than those driving Pc3's. Only instances where the planetary K-index indicates quiet conditions ($K_p < 4_0$) are included in the data sets used in the model development. In Table 5.1 $Pc3_{ind}$ data are summarised as the selection criteria are applied. For each year from 2002 to 2007 and for each criterion the set of $Pc3_{ind}$ measurements are summarised as follows: the number of data points (2nd column), the 10th, 50th and 90th percentile levels (columns 3 to 5) and the normalised variance (column 6) of each subset is listed. Applying these selection criteria changes the distribution of $Pc3_{ind}$ measurements. Figure 5.6 shows the distributions of $Pc3_{ind}$ as the different criteria (All, $K_p < 4_0$, $\chi < 90^0$, $K_p < 4_0$ and $\chi < 90^0$) are applied. Subsets of $Pc3_{ind}$ data (selected according to the different criteria) are binned in histograms, with each bin 20 pT in width. Due to the increased activity in the Pc3 band during disturbed conditions, the exclusion of $K_p > 4_0$ elements shifts the distribution of $Pc3_{ind}$ slightly towards zero, noted by the decrease in the percentile levels for each year. A slight decrease in variance due to the restriction to quiet times is also observed. The shift towards lower $Pc3_{ind}$ is clear when only quiet time data is considered (red curve, Figure 5.6), as a larger portion of $Pc3_{ind}$ is observed in the lowest bin of the histogram (0 - 20 pT) and smaller fractions of the total set is observed at higher $Pc3_{ind}$.

The absence of Pc3's on the night side of the Earth is illustrated by a marked increase in

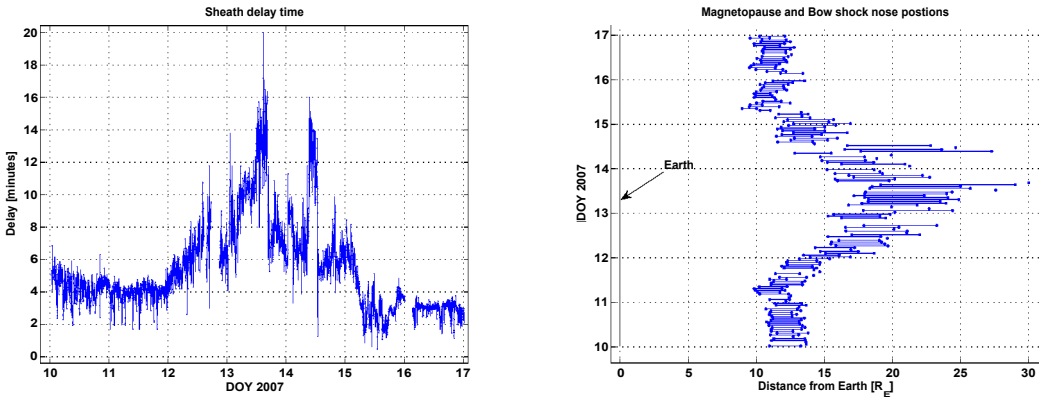

(a) Δt_{BM} (b) $R_{bs} - R_{mp}$

Figure 5.5: Time delay due to magnetosheath propagation (left) and the width of the magnetosheath (right) from day 10 to day 16 of 2007. The vertical black line indicates the Earth's position and the blue horizontal lines denote the sheath width, i.e. $R_{bs} - R_{mp}$, from day 10 to day 17.

normalised variance, and a shift of the distribution towards higher $Pc3_{ind}$, when only day side ($\chi < 90^0$) measurements are considered. This is visible in Figure 5.6 as the fractions of observations at higher $Pc3_{ind}$ is increased (see the blue and dashed curves). Combining the two criteria, so that only day time instances under quiet conditions are considered, results in a slight decrease in variance and a shift towards smaller $Pc3_{ind}$ compared to the $\chi < 90^0$-only case.

The following convention will be followed to assist the reader: The data sets defined in Table 5.1 that will be used in the model development, i.e. those satisfying the criteria $K_p < 4_0$ and $\chi < 90^0$ are denoted C2002, C2003, ... , C2007.

5.3.1 Input and Output Parameters

In the model development discussed in Chapter 4 solar wind speed $_{Vsw}, [hrs, hrc]$, solar wind dynamic pressure P_d, and the cone angle ϑ_{Bx} are identified as the most significant input parameters to a $Pc3_{ind}$-prediction model. In this chapter a similar model is developed, with the exception that short time scale data sets (5-minute running averages of 1-minute measurements) are used. A pool of candidate input parameters is identified and through the iterative wrapper process introduced in Chapter 4 a set of optimal inputs is selected. Since the same physical relationship is to be modelled, albeit at a shorter time scale, the pool of candidate

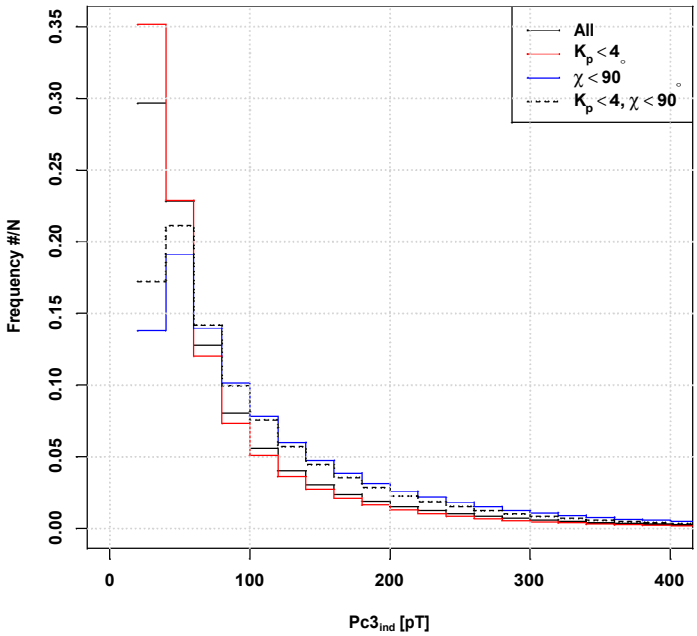

Figure 5.6: Distribution of $Pc3_{ind}$ for the selection criteria listed in the legend.

input parameters to be selected from is similar. Initially, 8 solar wind and IMF parameters are considered: solar wind speed V_{SW}, proton density N_p, electric (E) and magnetic (B) fields, cone angle ϑ_{Bx}, dynamic pressure P_d, Alfvénic Mach number M_A, and solar wind plasma β ratio. This is the ratio of thermal to magnetic energy in the plasma and is defined by [e.g. Treumann and Baumjohann, 1997b]

$$\beta = \frac{P_{th}}{P_{mag}} = 2\mu_0 \frac{N k_B T}{B^2} \tag{5.5}$$

where N is the particle number density, k_B is Boltzmann's constant and T the temperature. Two UT-derived variables are included to represent the local time dependence of Pc3 intensity. Solar zenith angle from the measurement position (THY) $\chi\,[^\circ]$ and $\chi' = 180^\circ - \chi$ forms an out-of-phase pair of input parameters that represents daily and seasonal variations. The pair $[\chi, \chi']$ is used in the same manner as the UT pair $[hrs, hrc]$ employed in Chapter 4.

Table 5.1: Statistical summary of $Pc3_{ind}$ measured at THY from 2002 – 2007 for the different selection criteria.

criteria (2002)	N	P_{10}	P_{50}	P_{90}	σ/N
all	468273	7.18	21.40	100.42	0.0079
$K_P < 4_0$	410733	6.94	19.55	93.75	0.0072
$\chi < 90^0$	235138	10.15	36.68	139.57	0.0241
$K_P < 4_0, \chi < 90^0$	208536	9.70	34.19	130.66	0.0218
criteria (2003)	N	P_{10}	P_{50}	P_{90}	σ/N
all	517879	9.75	37.11	176.99	0.028
$K_P < 4_0$	370596	8.72	31.16	150.38	0.020
$\chi < 90^0$	258965	16.56	65.65	250.14	0.088
$K_P < 4_0, \chi < 90^0$	190596	14.50	55.96	211.97	0.061
criteria (2004)	N	P_{10}	P_{50}	P_{90}	σ/N
all	515050	7.76	20.94	99.54	0.0088
$K_P < 4_0$	456263	7.54	19.35	91.17	0.0074
$\chi < 90^0$	258295	10.06	33.79	136.85	0.0233
$K_P < 4_0, \chi < 90^0$	232738	9.72	31.19	126.30	0.0202
criteria (2005)	N	P_{10}	P_{50}	P_{90}	σ/N
all	502741	7.75	22.65	110.64	0.011
$K_P < 4_0$	438684	7.500	20.67	99.62	0.008
$\chi < 90^0$	252965	10.56	37.69	154.60	0.036
$K_P < 4_0, \chi < 90^0$	223425	10.14	34.58	138.51	0.025
criteria (2006)	N	P_{10}	P_{50}	P_{90}	σ/N
all	515685	7.01	17.53	84.35	0.0065
$K_P < 4_0$	481686	6.89	16.55	79.13	0.0062
$\chi < 90^0$	257845	8.74	27.3	118.26	0.0206
$K_P < 4_0, \chi < 90^0$	242599	8.57	25.9	111.98	0.0199
criteria (2007)	N	P_{10}	P_{50}	P_{90}	σ/N
all	522426	6.83	16.46	81.260	0.0051
$K_P < 4_0$	495786	6.75	15.73	76.420	0.0049
$\chi < 90^0$	262929	8.36	25.00	114.962	0.0156
$K_P < 4_0, \chi < 90^0$	251212	8.25	23.83	107.499	0.0148

5.3.2 Correlation Between Parameters

It is reasonable to assume that some correlation between input parameters exists since all (solar wind) parameters are measurements of the same body of plasma. The correlation coefficient between pairs of input parameters and input-output parameter pairs are determined. Table 5.2 shows Pearson's correlation (ρ) between input parameters and between inputs and the output parameter for C2004. All correlations are significant at the 99% confidence level. The correlations for the other years are similar and the tables for c2002, C2003, C2005, C2006, C2007 are listed in Appendix A.

Table 5.2: Pearson correlation coefficient between parameters for 2004. Only data with $\chi < 90^{\circ}$ and $K_p < 4_0$ are considered.

2004	χ	χ'	V_{sw}	N_p	E	B	ϑ_{Bx}	P_d	M_A	β	$Pc3_{ind}$
χ	1.000	-1.000	-0.061	0.069	-0.019	0.012	0.002	0.061	0.048	0.056	-0.116
χ'	-1.000	1.000	0.061	-0.069	0.019	-0.012	-0.002	-0.061	-0.048	-0.056	0.116
V_{sw}	-0.061	0.061	1.000	-0.362	-0.087	0.050	-0.101	0.161	-0.012	-0.132	0.422
N_p	0.069	-0.069	-0.362	1.000	-0.102	0.352	0.172	0.798	0.263	0.233	0.003
E	-0.019	0.019	-0.087	-0.102	1.000	-0.285	-0.040	-0.195	0.058	0.029	-0.033
B	0.012	-0.012	0.050	0.352	-0.285	1.000	0.082	0.443	-0.527	-0.304	0.069
ϑ_{Bx}	0.002	-0.002	-0.101	0.172	-0.040	0.082	1.000	0.113	0.032	0.026	-0.360
P_d	0.061	-0.061	0.161	0.798	-0.195	0.443	0.113	1.000	0.277	0.161	0.275
M_A	0.048	-0.048	-0.012	0.263	0.058	-0.527	0.032	0.277	1.000	0.838	0.087
β	0.056	-0.056	-0.132	0.233	0.029	-0.304	0.026	0.161	0.838	1.000	0.013
$Pc3_{ind}$	-0.116	0.116	0.422	0.003	-0.033	0.069	-0.360	0.275	0.087	0.013	1.000

Several parameter pairs exhibit high correlation. The solar zenith angle pair (χ and χ') has a perfect negative correlation since χ' is just χ shifted by 180°. Solar wind speed and proton density are dependent variables and are negatively correlated (see earlier studies of solar wind parameters by [Hundhausen et al., 1970], for example). The magnetic field and proton density is positively correlated with $\rho = 0.352$ and the electric field, in turn, is negatively correlated with N_p due to the dependence on B. The cone angle shares a positive correlation with N_p, and a weak negative correlation with V_{sw}. The dependence on V_{sw} is probably a secondary dependence due to the $V_{sw} - N_p$ correlation. Dynamic solar wind pressure is defined by $P_d \sim N_p V_{sw}^2$ and a clear linear correlation between P_d and N_p exists. Dependence on V_{sw} is less clear via the linear correlation calculated, and a number of secondary correlations (with E, B and ϑ_{Bx}) is observed. The Alfvénic Mach number M_A (equation 2.20) is dependent on solar wind speed V_{sw}, density (N_p) and the IMF magnitude (B); essentially, $M_A \sim V_{sw} N_p / B$. This explains the high positive correlation with N_p and P_d, and the negative correlation with B. By definition (equation 5.5) the high correlation between β and N_p and B is expected. Secondary dependencies on N_p explain the correlations with P_d and M_A.

A strong correlation between the pulsation index $Pc3_{ind}$ and V_{sw} suggests the forcing of turbulence downstream by the solar wind. The cone angle effect is visible via the negative correlation of ϑ_{Bx} and $Pc3_{ind}$. The fairly strong dependence on P_d suggests that the size of the magnetosphere is important. Electric and magnetic field magnitudes do not exhibit strong correlations with any other parameters, except their expected mutual correlation.

It is important to note that these are merely linear correlations and that higher order dependencies are not resolved by ρ. For this reason the importance of solar wind parameters to

Pc3 generation cannot be discounted due to small correlations with $Pc3_{ind}$. However, two parameters from Table 5.2 are excluded from the modelling process: Plasma beta and M_A show very similar correlations with all other parameters, and they share a large degree of correlation with each other. Therefore it is reasonable to exclude β from further model development as it will play a similar role to M_A in the prediction of $Pc3_{ind}$. Although P_d shares a fair correlation with $Pc3_{ind}$, it is highly correlated with N_p, and to a lesser degree with V_{sw} as explained above. Consequently, P_d is excluded from the development of the model. The solar wind based parameters included in the set of candidate inputs are V_{sw}, N_p, E, B, ϑ_{Bx}, and M_A.

5.3.3 Training, Testing and Evaluation Data sets

Neural networks are trained by adapting weights between nodes such that the error made in test predictions during the training process are minimised. To produce a neural network-based prediction model three distinct data sets are necessary: the *training set* used by the training algorithm to adjust the weights after test predictions are made using the *testing set*, and the *evaluation set* of input and output parameter data that is used to gauge model fitness (i.e. the accuracy of the model). For the model to capably predict the observed relationship between input and output parameters, the training and testing data sets have to be representative of the modelled system.

A subset of a larger data set could be considered "representative" of that set if the two sets are distributed equally. In order to select a subset of data from a larger set with some unknown distribution, while ensuring that the subset has approximately the same distribution as the larger set, the following arguments are followed. Let $\mathbf{x} = \{x_1, x_2, \ldots, x_N\}$ be N observations of the random variable X that is observed with some unknown probability distribution. Next $M < N$ values $\mathbf{j} = \{j_1, j_2, \ldots, j_M\}$ are randomly selected from the set of integers $\{1, 2, \ldots, N\}$. The random selection is done uniformly, i.e. each integer could be selected with equal probability, and without replacement (i.e. the same integer cannot be selected twice). The subset of $\mathbf{x}$ with indices $\mathbf{j}$ is $\mathbf{y} \equiv \mathbf{x}_j = \{x_{j_1}, x_{j_2}, \ldots, x_{j_M}\}$, and since $\mathbf{j}$ is selected uniformly, $\mathbf{y}$ will have a similar distribution to that of $\mathbf{x}$ for large enough M. The training, testing and evaluation data sets used in this model are selected using this method.

The evaluation data set is constructed by selecting 7500 patterns from C2003 and C2005, respectively (the evaluation set consists of 15000 patterns). 50000 patterns are sampled from C2002, C2004, and C2006, respectively, to form a set of 150000 patterns; 30% of this set is used

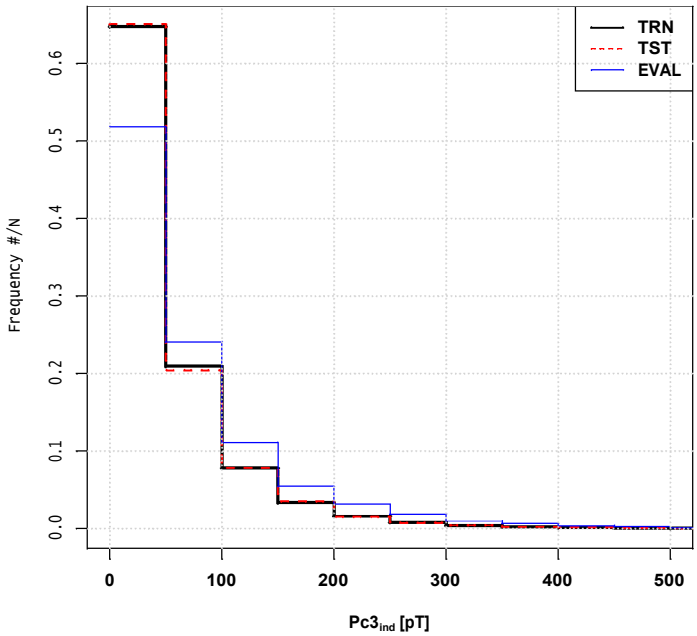

Figure 5.7: Distributions of $Pc3_{ind}$ for the training (TRN), testing (TST) and evaluation (EVAL) sets.

as the testing set and the remaining 70% of the set is the training set. C2007 is used for further evaluation and demonstration of the model. The distributions of $Pc3_{ind}$ for the the training (TRN), testing (TST) and evaluation (EVAL) sets are compared in Figure 5.7. The training and testing sets are distributed almost identically but the distribution of the evaluation set is slightly distorted.

5.4 Model Development

The process used to progressively build a neural network model with solar wind-based inputs and $Pc3_{ind}$ as output is the same as the one employed in Chapter 4. The set of candidate input parameters are: solar wind speed V_{SW}, proton density N_p in the solar wind, magnetic (B) and electric (E) fields, cone angle ϑ_{Bx}, and Alfvén Mach number M_A. The pair of time-related parameters $[X, X']$ is considered as a single input in the wrapper process. Each network is a fully connected feed-forward network with a single hidden layer. The number of hidden

nodes in each network is calculated by

$$N_h = 2N_i + 1 \tag{5.6}$$

and every ANN is trained for a maximum of 1000 training cycles or until divergence of the training and testing targets occur. Model fitness is judged by computing the correlation coefficient and root-mean-square error (RMSE) between measured $Pc3_{ind}$ and the predicted output $\hat{Pc3}_{ind}$. In each round of training the network that yields the best result in terms of the error measures (ρ, RMSE) is identified and the corresponding input parameters are selected to continue to the next round of training. The training process is illustrated by Table 5.3 and Figure 5.8. In the first round of training seven networks (nn01 – nn07) are trained, each with a different input parameter (indicated by the x's in the table), and the output $\hat{Pc3}_{ind}$ from each network is gauged for fitness according to ρ and RMSE. The ANN with V_{sw} as input (nn02) is the fittest model, with (ρ = 0.4549, RMSE = 73.6843), ahead of nn06 with V_{Bx} as input. After the second round V_{Bx} is added to the set of optimal input parameters with correlation of 0.6023 between measured and predicted output; nn09 yields the second best result, with (ρ = 0.4952, RMSE = 71.7619). Round three of the development process adds N_p to the set and in the fourth round nn19 with V_{sw}, V_{Bx}, N_p, and $[x, x']$ yields the best output with (ρ = 0.6838, RMSE = 60.23).

After the fourth round of training the network development concludes because no clear improvement in network performance is observed due to the addition of E, B, and M_A to the set of input parameters. A model with all candidates as inputs yields (ρ = 0.6864, RMSE = 60.0863), close to the performance of nn19. The performance of the network with all candidates is indicated with a horizontal line in Figure 5.8(a) and 5.8(b). The addition of any of the three remaining candidate inputs (E, B, or M_A) does not improve the model.

In Figure 5.9 the measured and predicted output from the winner of every round of training is plotted for a portion of the evaluation data set. The x-axis on each sub-figure indicates the index of the evaluation data set. The index number is used instead of time because the evaluation set is constructed by random selection from C2003 and C2005, and patterns do not necessarily follow each other in time. The model in Figure 5.9(a) has only V_{sw} as input and the output from this ANN is clearly only responding to the slow variation in V_{sw}. The higher resolution component of $Pc3_{ind}$ is not resolved at all. The addition of V_{Bx} to the set of input parameters (nn12 in Table 5.3 and Figure 5.9(b)) clearly increases the model's response

Table 5.3: Network performance during the wrapper process. Every network has a different set of input parameters, marked with x's. Two error measures (p and RMSE) are used to gauge network fitness. The fittest network in each round is nn02, nn12, nn15 and nn19.

Network #	$[X, X']$	V_{sw}	N_p	E	B	V_{Bx}	M_A	p	RMSE
nn01	x							0.1888	84.454
nn02		x						**0.4549**	**73.6843**
nn03			x					0.1136	85.0868
nn04				x				-0.0147	85.6106
nn05					x			0.1012	84.6344
nn06						x		0.3728	79.6431
nn07	,						x	0.263	82.1762
Network #	$[X, X']$	V_{sw}	N_p	E	B	V_{Bx}	M_A	p	RMSE
nn08	x	x						0.4932	72.021
nn09		x	x					0.4952	71.7619
nn10		x		x				0.4637	73.4462
nn11		x			x			0.4718	72.7557
nn12		x				x		**0.6023**	**66.5442**
nn13	,	x					x	0.4942	71.871
Network #	$[X, X']$	V_{sw}	N_p	E	B	V_{Bx}	M_A	p	RMSE
nn14	x	x				x		0.6287	64.6002
nn15		x	x			x		**0.6577**	**62.1878**
nn16		x		x		x		0.5988	66.5768
nn17		x			x	x		0.6105	65.791
nn18	,	x				x	x	0.603	66.4389
Network #	$[X, X']$	V_{sw}	N_p	E	B	V_{Bx}	M_A	p	RMSE
nn19	x	x	x			x		**0.6838**	**60.2383**
nn20		x	x	x		x		0.6547	62.4199
nn21		x	x		x	x		0.6562	62.2364
nn22		x	x			x	x	0.6572	62.2293

to short time scale variations in $Pc3_{ind}$. Adding N_p and the solar zenith angle pair X and X' to the set of inputs yields slight improvements in resolving some of the higher peaks in $Pc3_{ind}$ (see Figures 5.9(c) and 5.9(d)). As with the previous model, the highest peaks in $Pc3_{ind}$ are under estimated due to the rarity of large Pc3 events in the data.

5.5 Analysis and Conclusions

Each input parameter relates differently to the pulsation index. In this section nn19 is used to predict $Pc3_{ind}$ from C2007 and the influence of each input parameter on $Pc3_{ind}$ and $Pc3_{ind}$

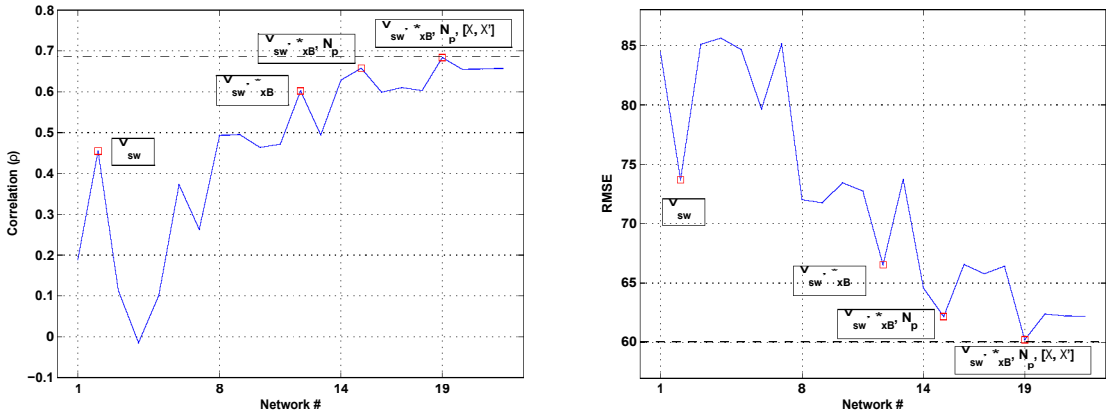

(a) Correlation coefficient (ρ) (b) RMSE

Figure 5.8: The (a) correlation coefficient and (b) root mean square error (RMSE) for each network trained. The winners of each round of training are indicated with squares labelled with the corresponding input parameters. A network with all candidate parameters as input achieves ρ and RMSE as indicated with a horizontal dashed line in each sub-figure.

is discussed. Using the C2007 set as the evaluation set, the model with $V_{sw}, V_{Bx}, N_p, [x, x']$ as input parameters reproduced the measured output with error measures of $\rho = 0.6891$, and RMSE = 42.0012.

From the earliest statistical studies of the influence of the solar wind on Pc3 pulsations [e.g. Saito, 1964; Wolfe et al., 1980] it has been clear that the Pc3 amplitude correlates positively with solar wind speed. Table A.6 confirms this by the $\rho = 0.5223$ correlation between V_{sw} and $Pc3_{ind}$ during 2007. The response of $Pc3_{ind}$ and $Pc3_{ind}$ to V_{sw} is made clear in Figure 5.10 where the peak intervals in pulsation activity coincide with peaks in solar wind speed, and the intervening decreases in $Pc3_{ind}$ with decreasing V_{sw}. Solar wind speed varies slowly on the 5 minute time scale and does not influence $Pc3_{ind}$ on this short scale.

Over short intervals it is V_{Bx} that governs the amplitude of Pc3's on the ground. Figure 5.11 shows the measured and modelled $Pc3_{ind}$, with V_{sw} and V_{Bx} for two consecutive days. On day 66 of 2007 the solar wind speed averages about 600 km.s^{-1} and on day 67 V_{sw} is below 500 km.s^{-1} for the entire day. The cone angle during both days averages about 50^0 and varies from over 80^0 to below 20^0. Pulsation intensity decreases from day 66 to day 67 (mean $Pc3_{ind}$ is 110 and 27 pT, respectively) as the average solar wind velocity falls from about 600 km.s^{-1} on day 66 to approximately 450 km.s^{-1} on day 67. At the same time the modelled

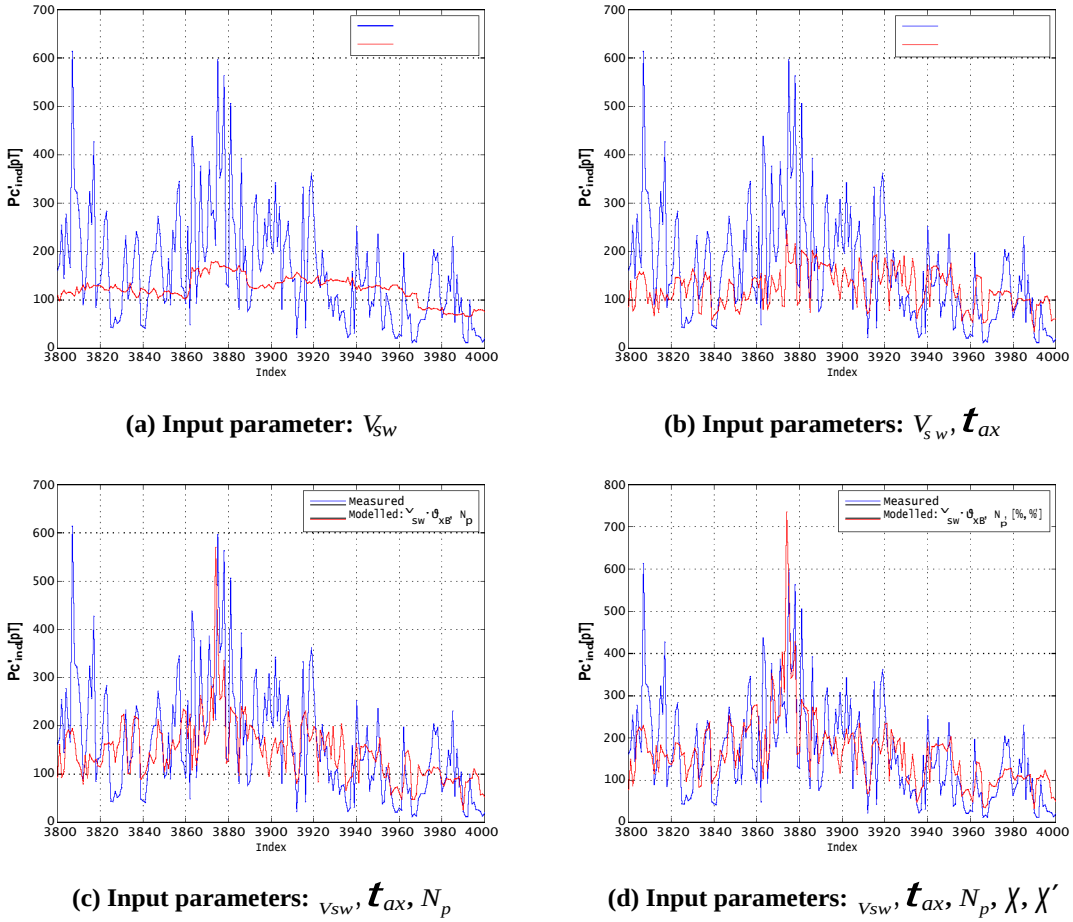

(a) Input parameter: V_{sw}

(b) Input parameters: V_{sw}, τ_{ax}

(c) Input parameters: V_{sw}, τ_{ax}, N_p

(d) Input parameters: V_{sw}, τ_{ax}, N_p, χ, χ'

Figure 5.9: Measured $Pc3_{ind}$ (blue) and the values predicted (red) by the four winning networks (nn02, nn12, nn15, nn19). The progressive improvement in the predicted output is clear as input parameters are added.

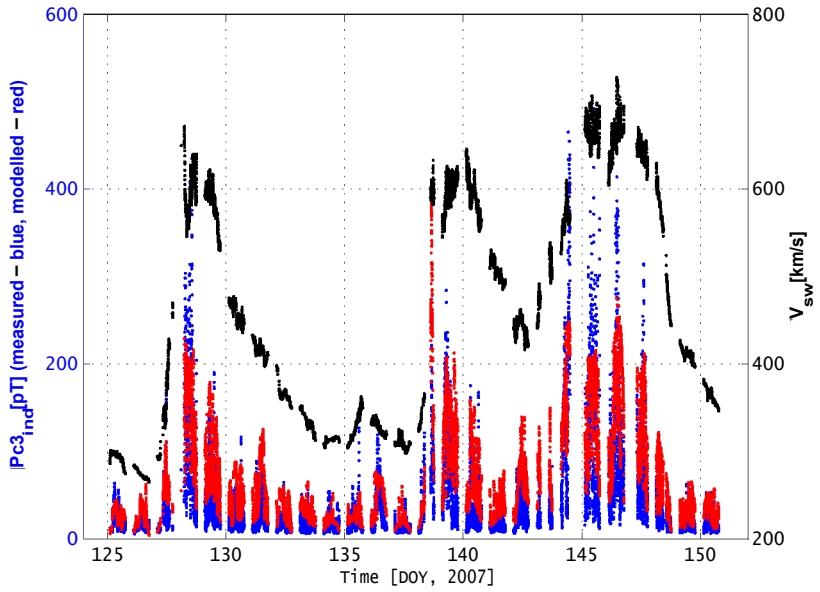

Figure 5.10: The influence of $_{Vsw}$ (black) on measured (blue) and predicted (red) $Pc3_{ind}$.

and measured $_{Pc3_{ind}}$ reacts to variations in cone angle magnitude on intervals less than one hour. (See the trough-peak-trough structure in ϑ_{Bx} between 12:00 and 14:00 on day 66, and the peak in $_{Pc3_{ind}}$ due to the decrease in ϑ_{Bx} near 15:00 on day 67, for example.)

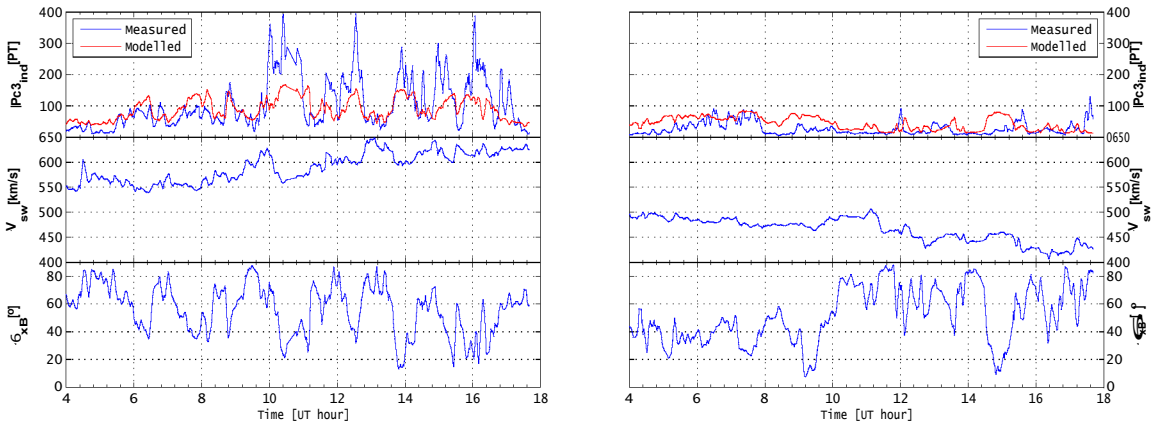

(a) Day 66 of 2007.

(b) Day 67 of 2007.

Figure 5.11: Measured and modelled pulsation index on (a) day 66 and (b) day 67 of 2007. The top panels show $_{Pc3_{ind}}$ and $Pc3_{ind}$, in the middle panels the solar wind speed $_{Vsw}$ is plotted and the lower panels show the cone angle.

To compare the reaction of modelled and measured $Pc3_{ind}$ to variations in cone angle and solar wind speed, the correlation p between ($Pc3_{ind}$, $Pc3_{ind}$) and V_{sw}, and ($Pc3_{ind}$, $Pc3_{ind}$) and V_{Bx} is calculated separately for each day in C2007. Figure 5.12 depicts the correlation for each day (blue dots and red x's) and the average correlations (horizontal lines) for measured $Pc3_{ind}$ and $\overline{Pc3}_{ind}$, respectively. The correlations between V_{sw} and $Pc3_{ind}$ (Figure 5.12(a)) are erratic, varying almost uniformly between -1 and 1. The average correlation with both the modelled and measured $Pc3_{ind}$ values are approximately $p = -0.04$. Furthermore, the fraction of negative correlations between V_{sw} and measured $Pc3_{ind}$ (207 out of 364 days) is large; a negative correlation between V_{sw} and $Pc3_{ind}$ does not make sense physically (Chapter 2), or according to the data (Table 5.2, Figure 5.10). The erratic and predominantly negative correlation between V_{sw} and $Pc3_{ind}$ over daily intervals suggest that V_{sw} does not influence $Pc3_{ind}$ on the short (5 minute) time scale considered here. The daily correlation between the pulsation index and V_{Bx} exhibits the dependence of $Pc3_{ind}$ on the rapid variations in IMF direction (Figure 5.12(b)). Re-orientation of the IMF from nearly parallel to the solar wind flow to a perpendicular orientation can result in the 'closure' of the magnetosheath to upstream generated turbulence, so that pulsation activity in the magnetosphere ceases [e.g. Wolfe et al., 1980; Le and Russell, 1994]. Figure 5.12(b) highlights the model's over-reliance on V_{Bx}. While the actual correlation between V_{Bx} and $Pc3_{ind}$ is -0.36, on average, the modelled $Pc3_{ind}$ has a much larger correlation ($p \approx -0.8$). Figure 5.13 illustrates the effect of V_{Bx} on $Pc3_{ind}$ in detail. The upper panel shows the measured and predicted $Pc3_{ind}$ for day 166 of 2007. In the lower panel the mirror-like interaction between V_{Bx} and $Pc3_{ind}$ reveals the model's over-reliance on cone angle.

In order to quantify a characteristic time scale of each solar wind based input parameter (V_{sw}, V_{Bx}, and N_p) the rise time (r_r) and fall time (r_f) are introduced. Levine [1996] defines the rise time of a parameter as the time required for the parameter to rise from x% to y% of its final value. Here the rise time is defined as the average time it takes solar wind parameter X to rise from below its 10th percentile level to above its 90th percentile level, and the fall time is the average time it takes to fall from above the 90% level to below the 10th percentile. One minute time resolution data sets for each year (2002 – 2007) are used to calculate r_r and r_f. Table 5.4 lists the rise and fall times of V_{sw}, V_{Bx}, and N_p for 2002 – 2007. The number of missing values per year is indicated in brackets. The rise time, fall time, and the 10th and 90th percentile levels of each variable are listed. The average rise times of V_{sw} vary between 4682 minutes (in 2005) and 7609 minutes (2006), while average fall times for V_{sw} is between 2489 minutes

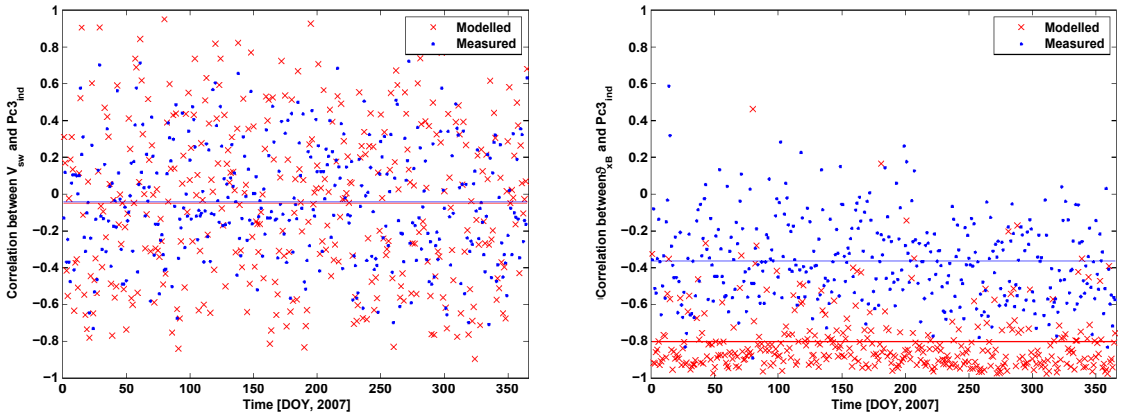

(a) $_{Vsw}$ - $Pc3_{ind}$ (b) ϑ_{Bx} - $Pc3_{ind}$

Figure 5.12: Daily correlation between $_{Vsw}$ and $Pc3_{ind}$ (left), and between ϑ_{Bx} and $Pc3_{ind}$ (right).

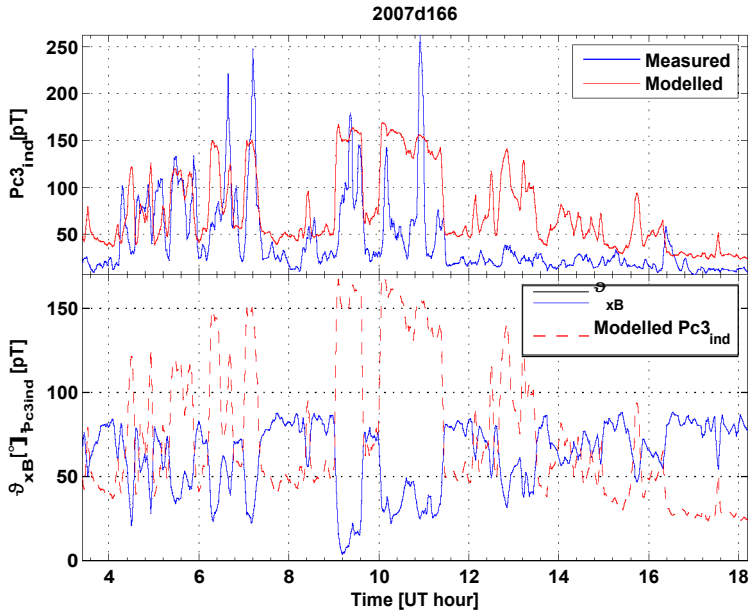

Figure 5.13: Influence of ϑ_{Bx} on measured and modelled $_{Pc3_{ind}}$. In the top panel measured (blue) and modelled (red) $_{Pc3_{ind}}$ is plotted and in the bottom panel cone angle (blue curve) is plotted with modelled $_{Pc3_{ind}}$ (red dashed curve).

in 2002 and 3858 minutes (2005). Shorter τ_f of $_{Vsw}$ is indicative of rapid increases in $_{Vsw}$ due to solar activity, and comparatively slow recovery from active periods. Conversely, the rise times of N_p are usually longer than fall times. This is observed due to the low plasma density

Table 5.4: Rise (r_r) and fall (r_f) times of V_{sw}, N_p and V_{Bx}, in minutes. The 10th and 90th percentile levels (P_{10} and P_{90}) of each parameter are indicated. The number of missing values for each year is indicated in brackets in the first column.

year (# missing)	X	r_r [min]	r_f [min]	P_{10}	P_{90}
2002 (100437)	V_{sw}	2489	4986	344 km.s^{-1}	570 km.s^{-1}
	N_p	1500	947	2.49 cm^{-3}	13.0 cm^{-3}
	V_{Bx}	44	42	25.0	82.0
2003 (87251)	V_{sw}	3570	5617	398 km.s^{-1}	717 km.s^{-1}
	N_p	1513	964	1.94 cm^{-3}	9.59 cm^{-3}
	V_{Bx}	31	34	23.0	81.0
2004 (80935)	V_{sw}	2613	7207	334 km.s^{-1}	587 km.s^{-1}
	N_p	790	948	2.06 cm^{-3}	10.13 cm^{-3}
	V_{Bx}	42	42	24.0	82.0
2005 (74937)	V_{sw}	3258	4682	336 km.s^{-1}	644 km.s^{-1}
	N_p	1534	1129	1.85 cm^{-3}	11.86 cm^{-3}
	V_{Bx}	40	40	23.0	82.0
2006 (94177)	V_{sw}	3825	7609	313 km.s^{-1}	593 km.s^{-1}
	N_p	1516	1060	1.98 cm^{-3}	12.31 cm^{-3}
	V_{Bx}	42	39	23.0	83.0
2007 (102659)	V_{sw}	2970	6566	314 km.s^{-1}	619 km.s^{-1}
	N_p	2056	1471	2.03 cm^{-3}	10.78 cm^{-3}
	V_{Bx}	37	38	23.0	83.0

at the trailing edge of high speed solar wind streams [Usmanov, 2005] and the long recovery time from high V_{sw} periods. Furthermore, N_p is negatively correlated with V_{sw}, so that a long recovery time from high V_{sw} to normal levels correspond to a long recovery time from low density to normal levels of N_p. Cone angle rise and fall times are nearly equal for every year, with a maximum difference between r_r and r_f of 3 minutes (2006). Rise and fall times are near 40 minutes for most years, except in 2003 where the minimum r_r and r_f are observed (31 and 34 minutes, respectively). The shorter rise and fall times in 2003 are indicative of the higher variability in the solar wind at solar maximum. The rise and fall times of N_p and V_{sw} are two orders of magnitude larger than that of V_{Bx}. This explains the sensitivity of measured and modelled $Pc3_{ind}$ to V_{Bx}, rather than V_{sw} or N_p, over sub-24 hour time intervals. Figure 5.14 shows typical rise and fall times of V_{sw} (5.14(a)) and V_{Bx} (5.14(b)).

Both the error measures computed show that the predicted output improves with the addition of N_p to the set of input parameters: Model nn12 with V_{sw} and V_{Bx} as input parameters

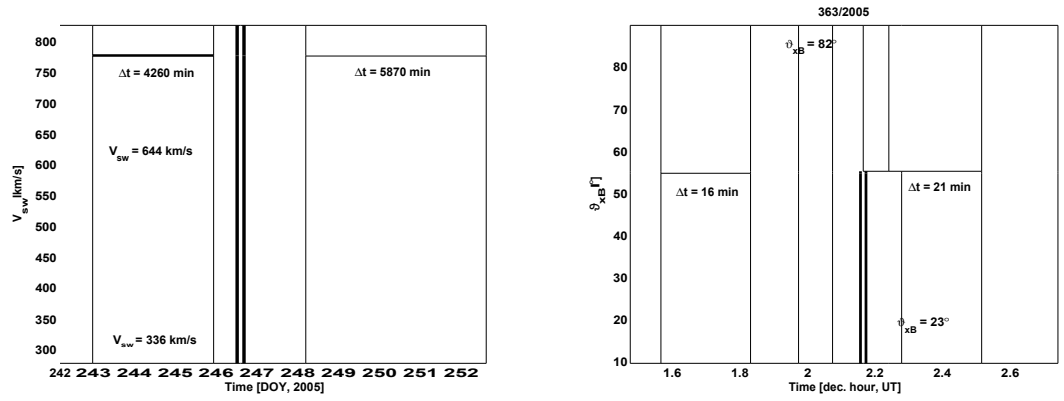

(a) V_{Sw} (b) V_{Bx}

Figure 5.14: Typical rise and fall times of (a) $_{VSW}$ and (b) V_{Bx} during 2005. The P_{10} and P_{90} levels of V_{Bx} and $_{Vsw}$ are indicated by horizontal dashed lines. See Table 5.4.

has $p = 0.6023$, and RMSE = 66.5442; and the inclusion of N_p (nn15) yields $p = 0.6577$, and RMSE = 62.1878. Comparing networks 12 and 15 during an interval of low N_p reveals the influence that N_p has on the model (Figure 5.15). On day 14 of 2007 the proton density is very low ($N_p \approx 1$ cm^{-3}) until about 12:50 UT (bottom panel of Figure 5.15(a)). During this interval very little pulsation activity is observed. Network 12 (with $_{Vsw}$ and V_{Bx} as inputs) only reacts to the variation in cone angle and the model does not reflect the observed cessation of Pc3 activity. The addition of N_p to the set of inputs (i.e. network 15) results in a decrease in the level of $Pc3_{ind}$ on this day, while the short-term variations in $_{Pc3_{ind}}$ are dictated by V_{Bx}. A similar comparison (Fig. 5.15(b)) on day 16 of 2007, but with a higher level of N_p observed (between 3 and 6 cm^{-3}) does not indicate a significant change in the predicted output due to the inclusion of N_p.

In Figure 5.16 the distribution of $_{Pc3_{ind}}$, and $_{Pc3_{ind}}$ from models nn12 and nn15, are plotted as functions of N_p. Each step-like curve represents the 95th percentile $_{(P_{95})}$ of $Pc3_{ind}$ for successive percentile intervals of N_p. That is, the height of each step is the level below which 95% of $_{Pc3_{ind}}$ falls, and the width of each step indicates the interval wherein 1% of N_p is observed. This type of plot provides information about the distribution of $_{Pc3_{ind}}$ versus N_p, but also about the distribution of N_p. The 95th percentile is plotted (instead of the mean, for example) to illustrate that the maximum level of $_{Pc3_{ind}}$ is dependent on N_p, barring outliers. The blue curve represents the output from nn12, the red curve nn15 and the black curve is the percentile levels of the measured pulsation index; the data is listed in Table 5.5, up to

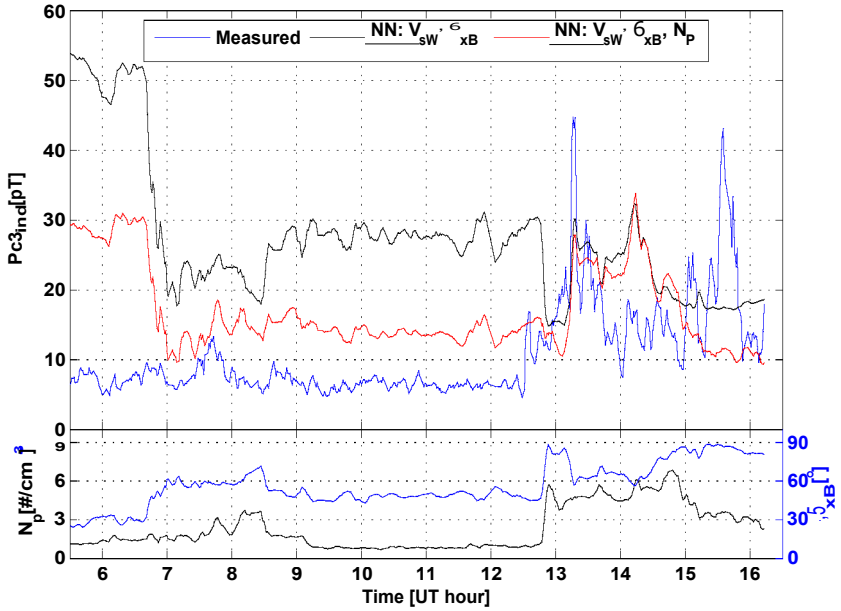

(a) Day 14 of 2007.

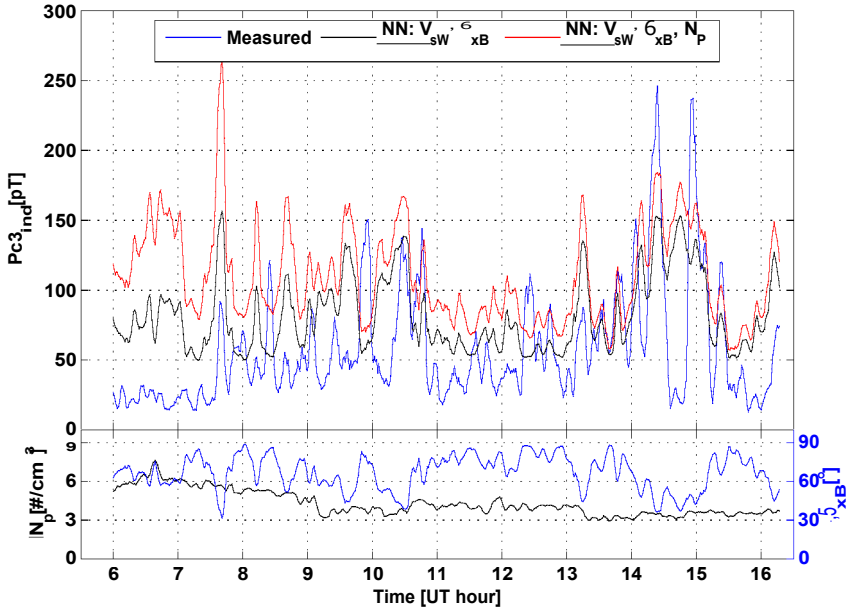

(b) Day 16 of 2007.

Figure 5.15: Influence of N_p on predicted $Pc3_{ind}$ on (a) day 14 and (b) day 16 of 2007. The black curve is the output of network 12, with V_{sw} and ϑ_{Bx} as input parameters, and the red curve is the predicted output of network 15, with inputs V_{sw}, ϑ_{Bx} and N_p. Cone angle (blue curve) and density (black curve) is indicated in the bottom panel of each sub-figure.

the 30th percentile of N_p. The increase in model accuracy due to the addition of N_p is clear when comparing the three distributions. The distribution of $Pc3_{ind}$ predicted by model nn15 is similar in shape to the observed $Pc3_{ind}$, illustrating the sensitivity of the neural network to N_p. However, the model (nn15) underestimates the level of $Pc3_{ind}$ for 1 cm^{-3} N N_p N4 cm^{-3}. These distributions of observed and modelled $Pc3_{ind}$ explain the observations in Figure 5.15: On day 14 (Fig. 5.15(a)) much of the observed N_p is below 1 cm^{-3} where model 15 (red curve) better represents the low levels of observed $Pc3_{ind}$ than model 12. On day 16 (Fig. 5.15(b)) N_p lies approximately between 3 and 6 cm^{-3} where the difference in $Pc3_{ind}$ distributions is much smaller between the two models, and hence no clear improvement in accuracy is seen on this day (Figure 5.15(b)).

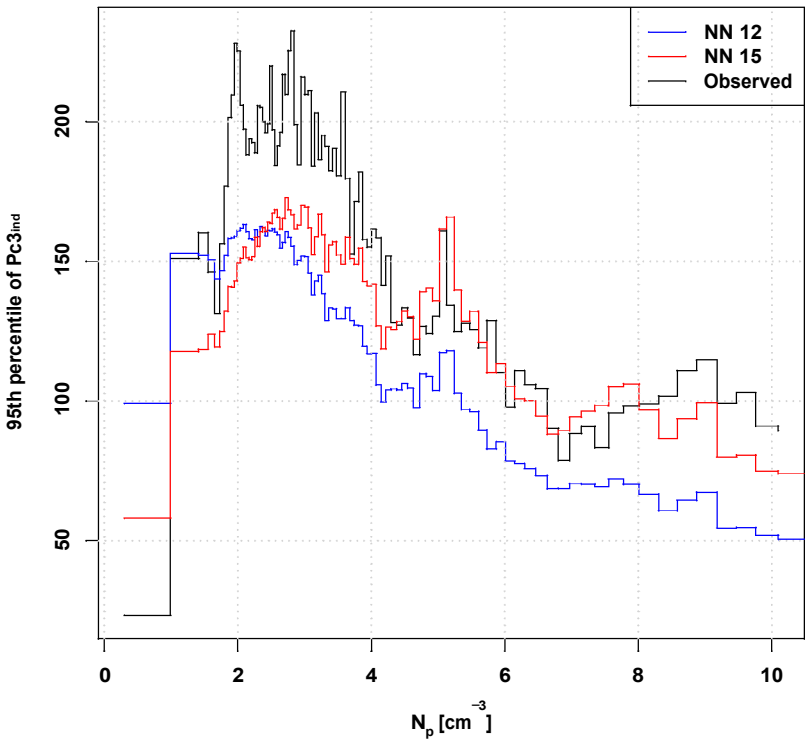

Figure 5.16: Distributions of observed $Pc3_{ind}$ (black curve) and the modelled $Pc3_{ind}$ for model numbers 12 and 15 (from Table 5.3). The curves indicate the 95% level of $Pc3_{ind}$ at successive percentiles of observed N_p.

It is known that Pc3 pulsations generally do not occur on the night side of the Earth and

Table 5.5: The 95th percentile levels of $Pc3_{ind}$ are computed at successive percentile intervals of N_p. The 95% level of all $Pc3_{ind}$ observed in coincidence with $P_i < N_p \leq P_{i+1}$ are listed in column 4, 5, and 6 for $Pc3_{ind}$ modelled by network 12, network 15 and observed $Pc3_{ind}$. Only the first 30 percentiles are listed. All 100 percentile values are plotted in Figure 5.16.

N_p percentiles			P_{95} of $Pc3_{ind}$		
i	P_i	P_{i+1}	Network 12	Network 15	Observed
0	0.304	0.992	100.173	58.472	23.5664
1	0.992	1.412	152.778	117.659	151.594
2	1.412	1.556	152.247	118.495	160.711
3	1.556	1.656	150.707	123.947	146.113
4	1.656	1.732	144.332	119.705	131.044
5	1.732	1.800	147.133	125.033	156.728
6	1.800	1.854	152.483	132.477	179.709
7	1.854	1.904	158.242	140.951	201.597
8	1.904	1.948	158.427	140.922	210.328
9	1.948	1.990	158.876	142.752	228.589
10	1.990	2.038	161.081	149.511	223.616
11	2.038	2.082	161.857	150.946	205.719
12	2.082	2.124	162.792	154.964	194.369
13	2.124	2.168	160.407	151.305	185.294
14	2.168	2.210	158.971	151.426	193.490
15	2.210	2.252	157.510	151.489	193.346
16	2.252	2.294	161.243	158.503	188.897
17	2.294	2.332	158.850	155.714	205.898
18	2.332	2.370	162.067	160.431	205.205
19	2.370	2.408	161.698	160.552	200.060
20	2.408	2.444	159.137	162.148	198.085
21	2.444	2.480	161.033	164.026	201.625
22	2.480	2.516	160.931	163.783	218.803
23	2.516	2.552	161.724	167.303	199.286
24	2.552	2.590	160.446	168.219	185.901
25	2.590	2.628	159.217	165.007	190.710
26	2.628	2.668	155.174	161.946	199.036
27	2.668	2.710	157.121	166.190	216.620
28	2.710	2.752	161.126	173.603	215.4775
29	2.752	2.796	158.399	168.221	225.3632
30	2.796	2.844	155.607	167.140	229.7904

hence measurements taken while $\chi \geq 90^{\circ}$ are excluded from the development of this model (see Section 5.3.3). Le and Russell [1994] showed that due to the orientation of the IMF with respect to the bow shock (Figure 2.3), the ion foreshock and the associated upstream ULF

wave activity occurs mostly in the morning sector of the upstream region. Heilig et al. [2010] concluded that the ULF energy responsible for exciting Pc3's in the magnetosphere enter near the subsolar point of the magnetosphere, and this is supported by the low resolution model's dependence on local time (Chapter 4). In Table A.6 a correlation of $p = -0.1049$ between $Pc3_{ind}$ and X is listed. Figure 5.17 below shows the influence of X on $_{Pc3_{ind}}$ and $Pc3_{ind}$ over three days. Since the zenith angle changes slowly on the minute scale the dependence of $_{Pc3_{ind}}$ on X is only visible over longer (multiple hour) intervals. The dependence of Pc3 activity on the Earth's orientation with respect to the Sun is clear, in that almost no activity is observed while $X > 90^0$. The modelled Pc3 index also exhibits dependence on X, even when restricted to predicting daytime data. The distribution of $_{Pc3_{ind}}$ and $\overrightarrow{Pc3}_{ind}$ versus X is plotted in Figure 5.18. Step-like curves are the 95th percentile levels of $_{Pc3_{ind}}$ (black) $\overrightarrow{Pc3}_{ind}$ (blue - nn15, red - nn19) plotted at successive percentile levels of X. The improvement in model performance, due to the inclusion of solar zenith angle as an input, is clear when comparing the distributions of model nn15, with V_{sw}, V_{Bx} and N_p as input parameters, and nn19 (with V_{sw}, V_{Bx} N_p and $[X, X']$). The largest Pc3 amplitudes occur in the smallest 2% of solar zenith angle observed in C2007: 95% of $_{Pc3_{ind}}$ lies below 261.9 pT if $23.5^0 < X < 24.8^0$ (first percentile interval of X), and 95% of $_{Pc3_{ind}}$ lies below 237.7 pT if $24.8^0 < X < 26.2^0$ (2nd percentile interval). Judging by the distribution of 95th percentile levels, X does not seem to influence $_{Pc3_{ind}}$ much between about 30 and 70 degrees, but as X increases from 70^0 toward 90^0, the pulsation activity is limited (from about 150 pT to about 100 pT). The inclusion of the out of phase pair $[X, X']$ improves the distribution of $\overrightarrow{Pc3}_{ind}$. Model nn15 does not resolve the decrease in $_{Pc3_{ind}}$ at high X and although an increase in $_{Pc3_{ind}}$ is observed at low X the level is far below the observed. Model nn19 correctly predicts the increased activity at small X and the decrease in $_{Pc3_{ind}}$ at large X, although the largest $_{Pc3_{ind}}$ values are not resolved.

The development of the high resolution model shows that it is three upstream parameters (V_{sw}, V_{Bx} and N_p) and a local time parameter (X) that determines most of the Pc3 activity observed on the ground. Using these four parameters as input to a neural network achieved accuracy of $p = 0.6838$, and RMSE = 60.2383 when predicting $_{Pc3_{ind}}$ from unseen data. The analysis of the influence of each input parameter suggests that solar wind velocity provides the level of pulsation intensity to be expected over long (hours to days) intervals and the cone angle V_{Bx} governs the variability in pulsation activity over short intervals (~ 5 minutes). Two indicators of local time, the solar zenith angle X and $X' = 180^0 - X$ provides the local time dependence of Pc3's that is due to the preferential day side generation and transmission into the magnetosphere of upstream ULF activity. The influence that N_p has on the pulsation

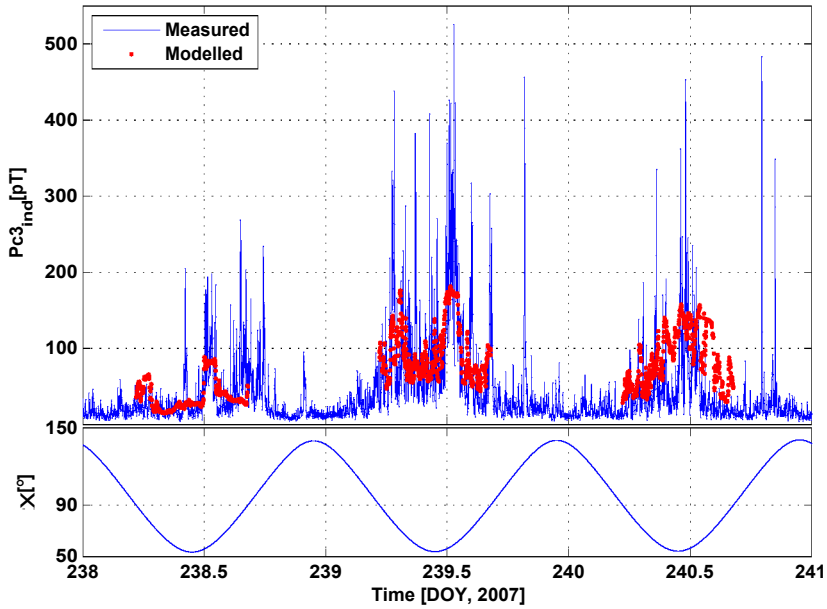

Figure 5.17: Measured and modelled $Pc3_{ind}$ from day 238 to 240 of 2007. $Pc3_{ind}$ is only modelled while $\chi < 90^{\circ}$ (red points). The lower panel shows the solar zenith angle (χ) for the same period.

index is less clear. The distribution of $Pc3_{ind}$ at various levels of observed N_p indicates that low N_p (< 1 cm^{-3}) results in a significant decrease in Pc3 activity, and the reaction of the ANN model clearly shows the decrease in the level of $Pc3_{ind}$ over a period of small N_p. In the next chapter the dependence of Pc3's on solar wind proton density is studied in detail.

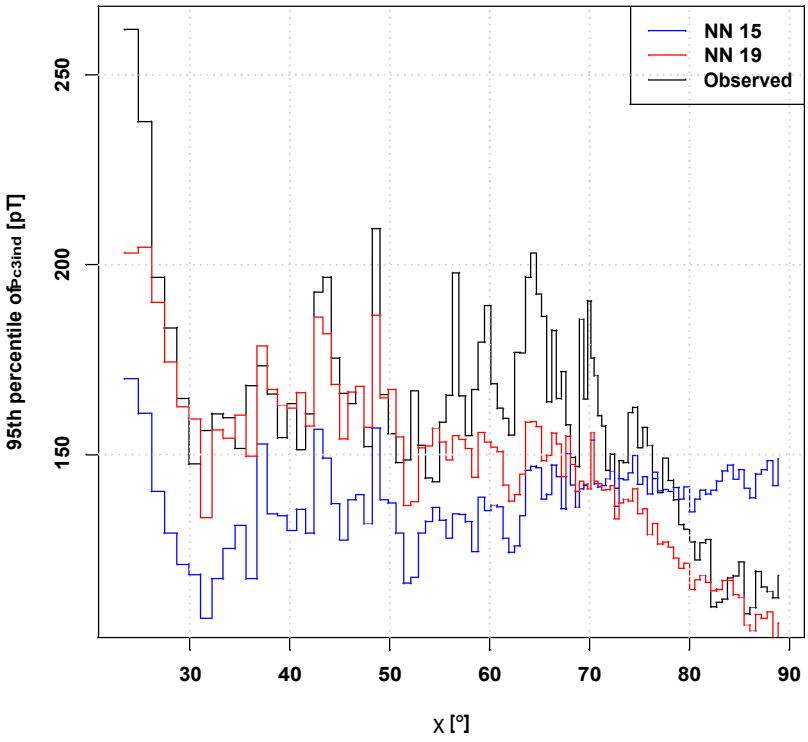

Figure 5.18: Distributions of observed $Pc3_{ind}$ (black curve) and the modelled $Pc3_{ind}$ for models nn15 (with inputs V_{sw}, ϑ_{Bx}, N_p) and nn19 (with V_{sw}, ϑ_{Bx}, N_p, $[\chi, \chi\ ]$). The curves indicate the 95% level of $Pc3_{ind}$ at successive percentile levels of χ.

Chapter 6

The Dependence of Pc3 Activity on Solar Wind Density

Chapters 4 and 5 described neural network based models for the prediction of the intensity of Pc3 pulsations observed on the ground, from solar wind parameters. In both chapters the modelling process ranks solar wind density-related parameters as important input parameters. The low resolution model (Chapter 4) has P_d as its third influential input parameter, after solar wind speed and universal time, with $_{R,np}$ and N_p yielding similar, but slightly lower accuracy. The high resolution model (Chapter 5) ranked N_p as the third most important input; P_d and $_{R,np}$ were not considered in the set of candidate inputs. In the analysis of both models it is observed that pulsation activity is inhibited during intervals of low solar wind density. Figures 4.10 and 5.15(a) show two intervals (day 144–145 of 2002, and day 16 of 2007) where low solar wind density (N_p N 1 cm^{-3}) results in a pause in pulsation activity. The distribution of $_{Pc3_{ind}}$ versus N_p, plotted in Figure 5.16, further suggests that pulsation activity is inhibited when N_p is low.

In this chapter the dependence of pulsation intensity $_{(Pc3_{ind}}$) on solar wind proton density (N_p) is investigated – specifically for low N_p, when the pause in Pc3 activity is observed. A simple statistical analysis of a large data set of $_{Pc3_{ind}}$ and solar wind measurements (1-minute averages taken between 2002 and 2007) is done, and the mechanisms that may inhibit pulsation activity due to low N_p are discussed.

6.1 A Low Density Interval

It has been observed that the magnetosphere and the foreshock region is more quiet during intervals of very low solar wind density. Le et al. [2000a] and Le et al. [2000b] investigated the pause in Pc3 activity on day 131 of 1999 when the solar wind density was below 1 cm^{-3} for most of the day. An order of magnitude decrease in ULF wave power is observed in the foreshock on day 131, compared to day 133 of 1999 when N_p sas 5 cm^{-3} for most of the day. Usmanov [2005] listed a number of low density anomalies (LDA, defined as intervals with $N_p < 0.3$ cm^{-3}) and sub-Alfvénic events (SAE, $M_A < 1$) in solar wind data from 1963 to 2003. Heilig et al. [2010] extended this list to include data from 2004 until 2008, and listed average values of solar wind parameters $_{(Vsw}$, P_d, M_A, ϑ_{Bx}) $^{\text{and}}$ $_{Pc3_{ind}}$ for events from 2001 to 2008. For most of the LDA's the pulsation index measured at THY is below 10 pT, near the noise level (6-7 pT) of the magnetometer used at THY [Heilig et al., 2007].

In Figure 6.1 the pulsation index (top panel) and a number of solar wind parameters (V_{sw}, ϑ_{Bx}, ^{Np,} $_{Rmp}$ and M_A) are plotted for day 27 of 2003, at 1 minute intervals. On this day the solar wind density decreases to below 1 cm^{-3} and remains near 1 cm^{-3} for almost four hours, causing pulsation activity to cease during this interval. Solar wind speed (black curve in the second panel of Figure 6.1) gradually decreases from near 540 km.s^{-1} to below 480 km.s^{-1} at the end of the day, and cone angle (blue curve, second panel) varies between 34 and 67 degrees. Proton density N_p (third panel) first becomes smaller than 1 cm^{-3} at 08:39 UT; two brief excursions above 1 cm^{-3} are observed near 10:00 and 12:00, but N_p does not exceed 1.22 cm^{-3} until 12:34 UT. During the 3h 54min interval (from 08:39 until 12:33 UT) the average pulsation index is 6.76 pT– at the noise level (6-7 pT) of the pulsation magnetometer employed at THY, i.e. zero pulsation activity in the Pc3 band. Average $_{Pc3_{ind}}$ between 05:02 (when χ first falls below 90^0) and 08:38 is 89.39 pT. After 12:34 N_p recovers to > 1.5 cm^{-3} and remains near 2 cm^{-3} until 16:35 (when χ rises above 90^0); accordingly, Pc3 activity resumes after 12:33 UT and the average $_{Pc3_{ind}}$ level between 12:34 and 16:35 is 40.16 pT. The decrease in $_{Pc3_{ind}}$ after the low density interval may be due to the lower solar wind speed (down from near 530 km.s^{-1} to near 480 km.s^{-1}). Two density dependent parameters, $_{Rmp}$ and M_A, are plotted in the bottom panel of Figure 6.1. During the low density interval the magnetopause expands to over 15 R_E and gradually decreases to $R_{mp} < 13$ R_E with $_{Vsw}$ as N_p recovers to values > 1 cm^{-3}. The Mach number M_A (blue curve, bottom panel) varies between 1.59 and 2.50 while N_p ,< 1 cm^{-3}.

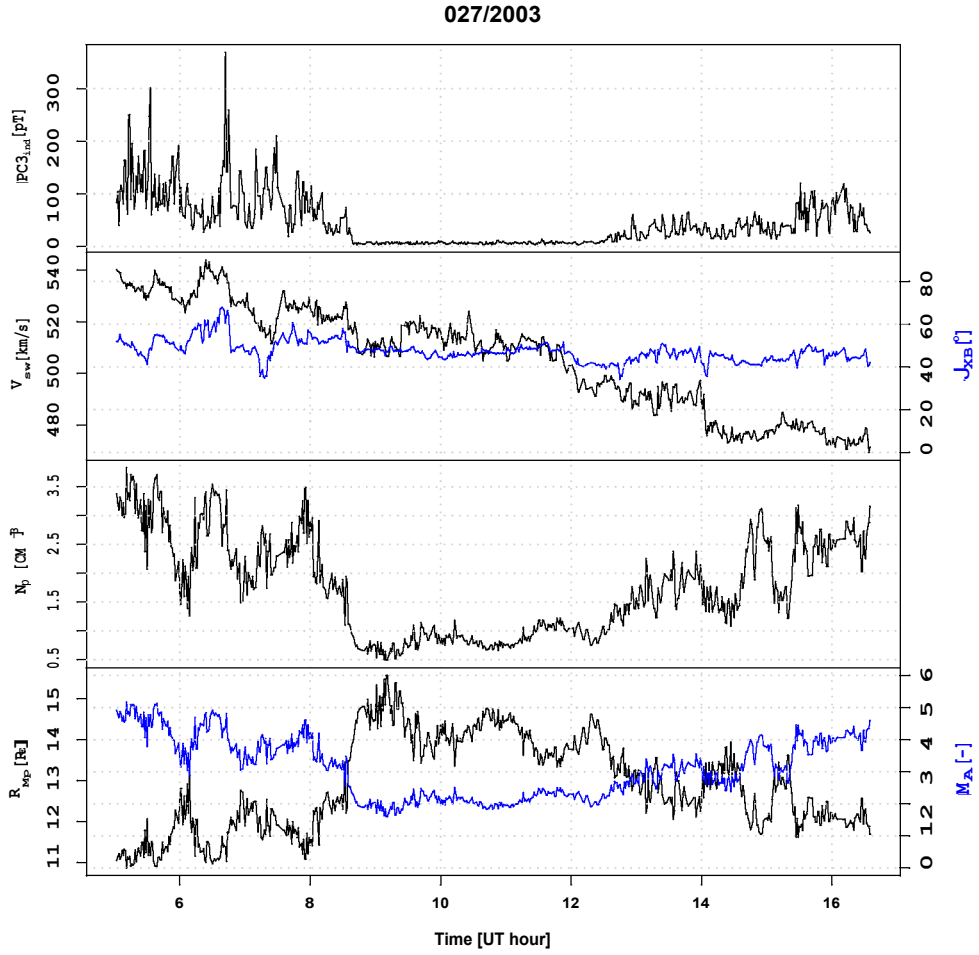

Figure 6.1: Low density event on day 27 of 2003. The pulsation index ($Pc3_{ind}$) is plotted in the top panel, V_{SW} (black) and ϑ_{Bx} (blue) are plotted in the second panel. Density (N_p) is plotted in the third panel, and in the fourth panel the Alfvénic Mach number (M_A) and the magnetopause stand-off distance (Rmp) are plotted. The decrease in density between 08:39 and 12:34 UT results in decreased M_A, increased R_{mp}, and a cessation of Pc3 activity.

6.2 Distribution of Data

In this chapter a large data set of solar wind parameters and $Pc3_{ind}$ is employed. All solar wind data are 1-minute averages (and not the 5 minute running means used in the previous chapter) from the HRO (High Resolution OMNI) data set. The correction for propagation time from the bow shock, described in Chapter 5.2, is applied to data from 2002 to 2007. Furthermore, the criteria described in Chapter 5.3 are applied so that only day time ($\chi < 90^{\circ}$) and quiet time ($K_p < 4_0$) data are considered.

Sets of pulsation index ($Pc3_{ind}$), solar wind proton density (N_p), bulk solar wind speed (V_{sw}) and cone angle (V_{Bx}) data are employed in this chapter. The four sets of measurements are summarised in Table 6.1. The minimum, mean and maximum values of each parameter are calculated and the 25th, 50th (i.e. median) and 75th percentiles are also listed in the table. In the last two columns the estimated skewness (A) and kurtosis (x) of each set are listed. Skewness is a measure of a distribution's asymmetry, indicating either an extended tail to the left (A < 0) or to the right (A > 0). A Gaussian distribution has A = 0 (see Spiegel et al. [2000], for example). Kurtosis indicates the "peakedness" of a distribution – a normal distribution has x = 3, and x < 3 indicates a distribution that is flatter than the Gaussian. A distribution with x > 3 has a larger peak around the mean, but is heavier near the tails, meaning occurrences of (large or small) extreme values are more probable than if it were normally distributed. A higher kurtosis means that more of the variance is due to infrequent extreme values, rather than due to commonly occurring moderate deviations from the mean [e.g. Spiegel et al., 2000]. Solar wind speed and cone angle both exhibit near-Gaussian skewness (A ≈ 0 for V_{sw} and V_{Bx}) and kurtosis (x ≈ 3 for both). Solar wind proton density has positive A and x, indicating a non-Gaussian distribution that is skewed to the right with heavy tails. The pulsation index shows an even more dramatic deviation from the Gaussian, with positive A and large kurtosis. The positive x values for $Pc3_{ind}$ and N_p suggests that the number of (large or small) extreme values are not insignificant.

Table 6.1: Statistical summary of $Pc3_{ind}$, N_p, V_{sw} and V_{Bx}. Each set has 1118162 values.

X	Min	P_{25}	P_{50}	Mean	P_{75}	Max	A	x
$Pc3_{ind}$	1.73	15.47	32.37	58.77	71.67	4560.00	5.83	140.35
N_p	0.030	2.860	4.300	5.614	6.820	71.780	3.25	22.15
V_{sw}	180.7	371.2	431.6	450.4	516.0	962.0	0.66	2.89
V_{Bx}	0.00	36.52	54.08	53.18	71.10	90.00	-0.18	2.08

The distributions of V_{sw}, V_{Bx}, N_p, and $Pc3_{ind}$ are plotted in Figure 6.2 and the probability density function (PDF) of each set is estimated. A number of probability density functions are fitted to each distribution of data by adapting the parameters a and b to maximise the log-likelihood (Y) of the fit. The software employed to accomplish the PDF fitting is the `fitdistr()` function in the MASS library of the R statistical software package (http://cran.r-project.org/). The PDF's that best fit the distribution of $Pc3_{ind}$ are the normal (Gaussian), log-normal, Weibull, and F density functions. The normal distribution of

a continuous random variable x is defined by

$$f_N(x) = \frac{1}{\sqrt{2\pi b^2}} \exp\left(-\frac{(x-a)^2}{2b^2}\right) \tag{6.1}$$

with a the mean and b the standard deviation of the distribution. A random variable X is log-normal distributed if $\log(X)$ is normally distributed. The probability density function of this distribution is

$$f_{LN}(x) = \frac{1}{x\sqrt{2\pi b^2}} \exp\left(-\frac{(\log x - a)^2}{2b^2}\right) \tag{6.2}$$

with a is mean, and b the standard deviation. The Weibull distribution function is

$$f_W(x) = \begin{cases} \frac{b}{a}\left(\frac{x}{a}\right)^{b-1} \exp\left[-(x/a)^b\right], & x > 0 \\ 0, & x < 0 \end{cases} \tag{6.3}$$

with the shape and scale of f_W given by a and b, respectively. The F-distribution function is defined by

$$f_F(x) = \frac{\sqrt{(ax)^a b^b}}{(ax+b)^{a+b}} \frac{}{xP\left(\frac{a}{2}, \frac{b}{2}\right)}. \tag{6.4}$$

Here a and b are the first and second degrees of freedom and $P(x,y)$ is the beta function

$$P(x,y) = \int_0^1 t^{x-1}(1-t)^{y-1} dt \tag{6.5}$$

defined for $x \in \mathbb{R}$, $y \in \mathbb{R}$, $y > 0$. Tables 6.2(a) – (d) list the parameters (a and b) of the optimally fitted PDF of each type, with the corresponding log-likelihood value (Υ). According to this method both $Pc3_{ind}$ and N_p are distributed with a log-normal density function (see Tables 6.2(a) and (b)). A quantity that is log-normally distributed is created by a multiplicative process applied to a number of normally distributed random variables. Limpert et al. [2001] briefly reviews the log-normal distribution and its role in processes in various fields of research (e.g. medicine, geology and economics). The distribution of $Pc3_{ind}$ alludes to the generation of Pc3 pulsations by mechanisms dependent on a number of independent physical quantities. Solar wind speed (Table 6.2(c)) is best represented by a log-normal distribution, although the normal distribution also fits the distribution reasonably well (compare Υ for normal and log-normal). Figure 6.2 shows the distribution of each parameter with the optimal fits of the four density functions tested. None of the distributions fit the cone angle (see Table 6.2(d) and Figure 6.2(d)).

Table 6.2: Parameters a and b of the PDF's optimally fitting the distribution of $Pc3_{ind}$, N_p, V_{sw} and t_{Bx} between 2002 and 2007. Log-likelihood ($\mathcal{Y}$) determines the accuracy of the fitted function (higher $\mathcal{Y}$ is more accurate).

(a) $Pc3_{ind}$

PDF	a	b	$\mathcal{Y}$ x 10^6
Log-normal	**3.541**	**1.010**	**-5.55**
Weibull	**57.886**	**0.971**	**-5.67**
Normal	**58.769**	**76.377**	**-6.43**
F	**885.626**	**0.541**	**-6.78**

(b) N_p

Function	a	b	$\mathcal{Y}$ x 10^6
Log-normal	**1.492**	**0.674**	**-2.81**
Weibull	**6.243**	**1.431**	**-2.92**
Normal	**5.613**	**4.543**	**-3.27**
F	**394.362**	**1.530**	**-3.63**

(c) V_{sw}

Function	a	b	$\mathcal{Y}$ x 10^6
Log-normal	**6.084**	**0.2242**	**-6.71**
Weibull	**492.116**	**4.494**	**-6.81**
Normal	**450.385**	**103.66**	**-6.77**
F	**652.435**	**0.301**	**-10.18**

(d) t_{Bx}

Function	a	b	$\mathcal{Y}$ x 10^6
Log-normal	**3.870**	**0.532**	**-5.20**
Weibull	**60.288**	**2.729**	**-5.020**
Normal	**53.679**	**21.597**	**-5.022**
F	**31.042**	**0.488**	**-7.25**

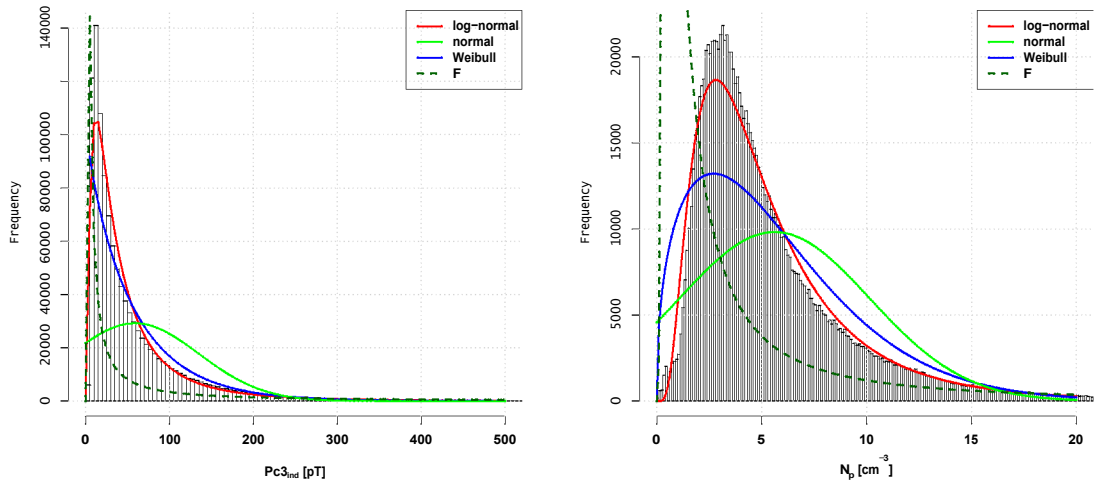

(a) $Pc3_{ind}$ **(b)** N_p

(c) V_{sw} **(d)** t_{Bx}

Figure 6.2: Various PDF's fitted to the distributions of $Pc3_{ind}$, N_p, V_{sw} and t_{Bx}. The log-normal PDF best fits the distributions of $Pc3_{ind}$, N_p and V_{sw}; t_{Bx} is best represented by a Weibull distribution.

6.3 Analysis

The influence of solar wind speed and cone angle on Pc3 activity is well known and widely published [e.g. Saito, 1964; Kovner et al., 1976; Troitskaya, 1994; Heilig et al., 2007]. Using the large data set employed in this chapter (1 minute measurements from 2002 – 2007), the combined influence of $_{Vsu,}$ and ϑ_{Bx} on $_{Pc3_{ind}}$ is clearly illustrated in Figure 6.3. This figure is essentially a three dimensional scatter plot with $_{Vsu,}$ on the horizontal axis, ϑ_{Bx} on the vertical axis and the colour scale indicating $_{\log10(Pc3_{ind})}$. Observed values of $_{Vsu,}$ and ϑ_{Bx} are arranged in a 64 × 64 grid and the average of all $_{\log10(Pc3_{ind})}$ observed within each cell is represented by the colour scale indicated by the legend. The base-10 logarithm of $Pc3_{ind}$ is used for clarity of the colour scale. The three-dimensional colour plots employed in this chapter are created by the `quilt.plot()` function, from the `fields` library (see `http://www.image.ucar.edu/Software/Fields/`) of the `R` statistical software package.

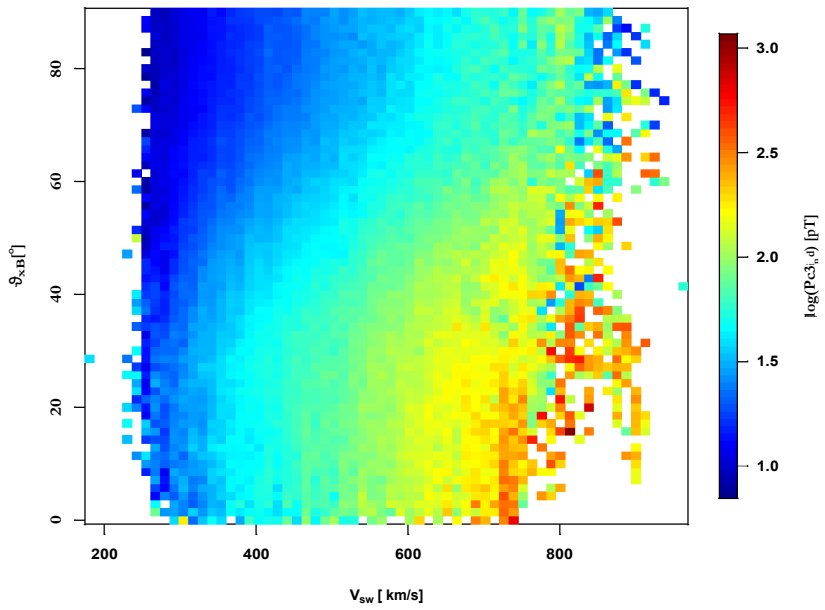

Figure 6.3: Pulsation intensity (colour scale) plotted against solar wind speed (horizontal axis) and cone angle (vertical axis). Each coloured pixel in the 64 × 64 grid denotes the average $\log_{10}(Pc3_{ind})$. The dependence of $_{Pc3_{ind}}$ on $_{Vsu,}$ and ϑ_{Bx} is clear: small cone angle and high solar wind speed is favourable to Pc3 activity, and large ϑ_{Bx} and small $_{Vsu,}$ is not.

The highest $_{Pc3_{ind}}$ is observed when the cone angle is low and the solar wind speed is high, allowing the magnetosheath to be flooded by upstream ULF waves that are convected

downstream by the solar wind. Pulsation intensity decreases smoothly from ~ 1000 pT towards ~ 10 pT with increasing ϑ_{Bx} and decreasing V_{sw}. The dependence of $Pc3_{ind}$ on both V_{sw} and ϑ_{Bx} is made clear by the variation in the colour scale across regions of constant V_{sw} or ϑ_{Bx}. High V_{sw} will produce moderate pulsation activity, even with moderately large ϑ_{Bx} – see the $V_{sw} > 700$ km.s^{-1}, $\vartheta_{Bx} > 70^0$ range; and pulsations occur, even with very low solar wind speed, given that the IMF is favourably directed ($\vartheta_{Bx} \geq 20^0$).

The high resolution model developed in Chapter 5 ranked V_{sw}, ϑ_{Bx}, and N_p as the three most important solar wind-based input parameters. These three parameters are compared with pulsation intensity using the three dimensional grid plotting method described above (Figure 6.3). In Figure 6.4 $Pc3_{ind}$ is plotted versus N_p and V_{sw}, and in Figure 6.5 $Pc3_{ind}$ is plotted against N_p and ϑ_{Bx}. In Figure 6.4(a) the entire range of observed N_p is plotted and in Figure 6.4(b) only the low N_p range (< 5 cm^{-3}) is shown. The layout of the coinciding data points reveals the anti-correlation between V_{sw} and N_p observed in Table 5.2: high V_{sw} is only observed at fairly low levels of N_p, and no observations are made in the high V_{sw}, large N_p ($V_{sw} > 600$ km.s^{-1} and $N_p > 30$ cm^{-3}) range. The $Pc3_{ind}$ level increases with V_{sw} as expected, but the influence of N_p on $Pc3_{ind}$ is less clear. A weak dependence on N_p is observed (Figure 6.4(a)) as $Pc3_{ind}$ grows with N_p increasing from near 0 to 10 cm^{-3}. High levels of pulsation activity occur throughout the range of densities, as long as $V_{sw} \geq 400$ km.s^{-1}. In the lowest range of observed N_p, $Pc3_{ind}$ remains low even while high solar wind speed is observed. While $N_p < 1$ cm^{-3} (Figure 6.4(b)), $Pc3_{ind}$ remains near 10 pT throughout the range of solar wind speed (250 $\leq V_{sw} \leq$ 1000 km.s^{-1}). Above 1 cm^{-3}, $Pc3_{ind} \geq$ 100 pT is observed and the expected dependence on V_{sw} is observed.

The expected increase in $Pc3_{ind}$ with decreasing cone angle is observed in Figure 6.5, and the pause in pulsation activity while $N_p < 1$ cm^{-3} is observed, even at very low (near 0^0) ϑ_{Bx} (see Fig. 6.5(b)). Throughout the $N_p \geq 2$ cm^{-3} range of observations no clear dependence on N_p is visible – it is only when $N_p < 2$ cm^{-3} that the dependence of $Pc3_{ind}$ on N_p is observed. As density decreases below $N_p = 2$ cm^{-3}, $Pc3_{ind} \sim 10$ pT is observed at decreasing levels of ϑ_{Bx}; and when $N_p \approx 0.8$ cm^{-3}, $Pc3_{ind} \sim 10$ pT throughout the range of observed ϑ_{Bx}. This may suggest that a threshold exists near $N_p = 1$ cm^{-3}, below which the generation or propagation of upstream waves are inhibited.

The decrease in N_p lowers the dynamic pressure applied to the geomagnetic field by the

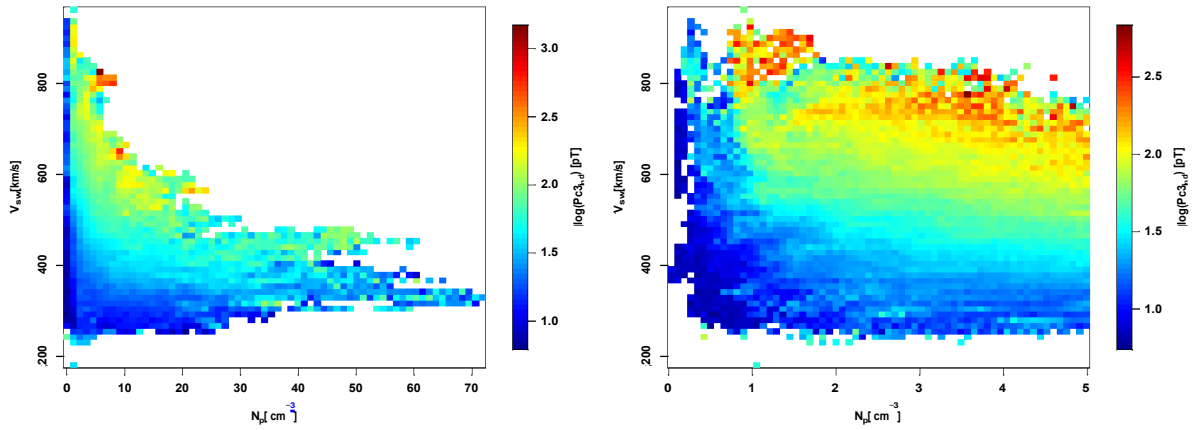

(a) (b)

Figure 6.4: Pulsation intensity (log($Pc3_{ind}$), colour scale) plotted against N_p (x-axis) and V_{sw} (y-axis), for the (a) entire range of N_p and (b) for $N_p < 5$ cm^{-3}.

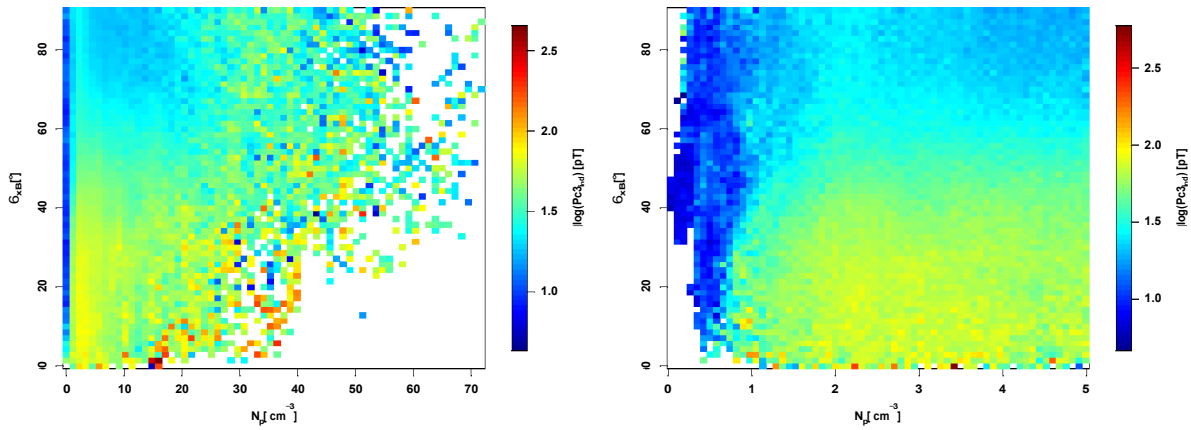

(a) (b)

Figure 6.5: Pulsation intensity (log($Pc3_{ind}$), colour scale) plotted against N_p (x-axis) and ϑ_{Bx} (y-axis), for (a) the entire range of N_p and (b) for $N_p < 5$ cm^{-3}.

solar wind and as a result the size of the magnetospheric cavity increases. The larger cavity means that upstream generated ULF waves have to propagate further to reach the inner magnetosphere and the ionosphere to couple with field line resonances or ionospheric currents. Compressional mode waves in the magnetosphere will undergo geometric attenuation dependent on the size of the cavity, and hence it is expected that Pc3 activity will decrease with decreasing N_p. The influence that N_p has on $Pc3_{ind}$ via the size of the magnetospheric cavity

(i.e. $_{R,np)}$ is illustrated in Figures 6.6 and 6.7 below. In Figure 6.6 pulsation intensity is directly compared with the magnetopause stand-off distance $_{(R,np)}$ in R_E. In the top panel the coinciding measurements of $_{Pc3_{ind}}$ and $_{R,np}$ are plotted. The dependence of pulsation intensity on the cavity size is clear. Maximum $_{Pc3_{ind}}$ is observed at about 11.5 R_E and $_{Pc3_{ind}}$ decreases exponentially with increasing stand-off distance. In the middle panel the 95% level of $Pc3_{ind}$ observed at successive 1% intervals of $_{R,np}$ is plotted with a step-like curve; the width of each step indicates the 1% interval. In the bottom panel the 50% level of $_{Pc3_{ind}}$ (i.e. the median), calculated at successive 1% intervals of $_{R,np}$, is plotted in black, and the mean of $_{Pc3_{ind}}$ for regular subsets of $_{R,np}$ (each 0.5 R_E wide) is plotted in red. Below about 10 R_E, the 95% level, mean and median $_{Pc3_{ind}}$ values remain nearly constant, suggesting that for such high levels of $_{Vsw}$ and N_p other factors may determine the amplitude of pulsations.

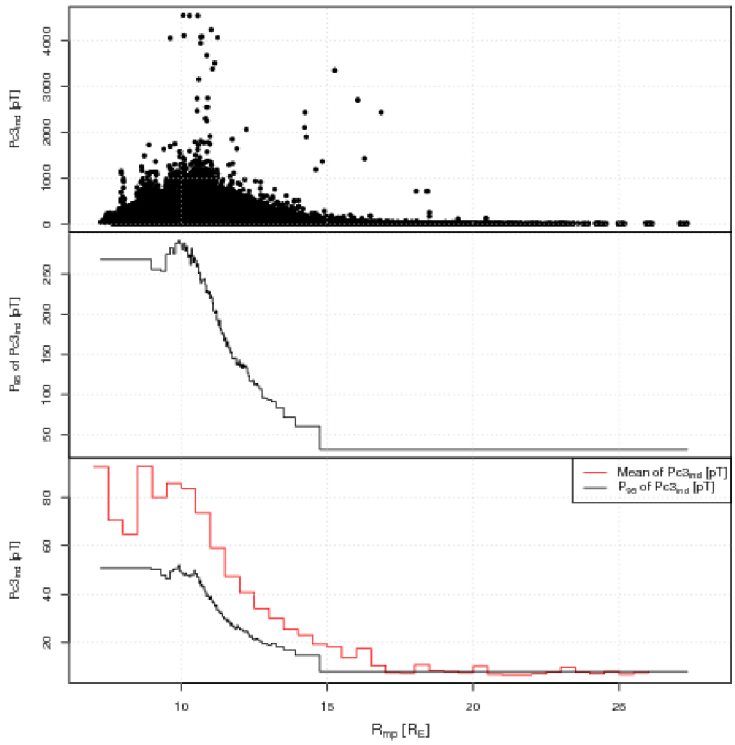

Figure 6.6: Pulsation intensity is plotted against the magnetopause stand-off distance in the top panel. In the second panel the 95th percentile level of $_{Pc3_{ind}}$ is plotted at successive percentile intervals of $_{R,np}$. The third panel shows the mean $_{Pc3_{ind}}$ calculated for successive 0.5 R_E intervals of $_{R,np}$ (red curve) and the 50th percentile of $_{Pc3_{ind}}$ (i.e. the median) at successive 1% levels of $_{R,np}$ (black curve).

The magnetopause stand-off distance is approximated by $R_{,np} \approx (110.2 N_p V_{sw}^2)^{-1/6}$ (equa-

tion 2.29). To separate the effect that N_p has on $Pc3_{ind}$ due to the size of the magnetosphere, $Pc3_{ind}$ is plotted versus $N_p^{-1/6}$ and $110.2 V_{sw}^{-1/3}$ using the `quilt.plot()` function described earlier (first used in Figure 6.7). The stand-off distance decreases linearly from the origin on this set of axes; black curves are contour lines indicating R_{mp} at 8, 12, 14 and 20 R_E. The pulsation index intensifies with decreasing R_{mp}. Near $R_{mp} = 20$ R_E the mean $Pc3_{ind}$ is about 10 pT, indicating very weak Pc3 activity, near the noise level of the instrument. Between 12 and 14 R_E moderate ($10^{1.3}$ pT) to high (100 pT) $Pc3_{ind}$ is observed, and mean $Pc3_{ind}$ for $12 < R_{mp} < 14$ is 36.85 pT. Pulsation activity intensifies further with the compression of the magnetosphere to $8 < R_{mp} < 12$ R_E; low, moderate and high $Pc3_{ind}$ is observed in this range of R_{mp}, with mean $Pc3_{ind} = 66$ pT. The dependence of $Pc3_{ind}$ on both V_{sw} and N_p is clear, even for $N_p < 1$ cm^{-3}. Between $N_p = 0.33$ cm^{-3} and $N_p = 1$ cm^{-3} $Pc3_{ind}$ increases from ~ 10 pT to ~ 100 pT with V_{sw}. The slopes of the contour lines are steeper than that of the similarly coloured regions of the plot. This may suggest that the dependence of $Pc3_{ind}$ is not on $N_p V_{sw}^2$ (as is the case with R_{mp}) but on $N_p V_{sw}^k$ with $k < 2$.

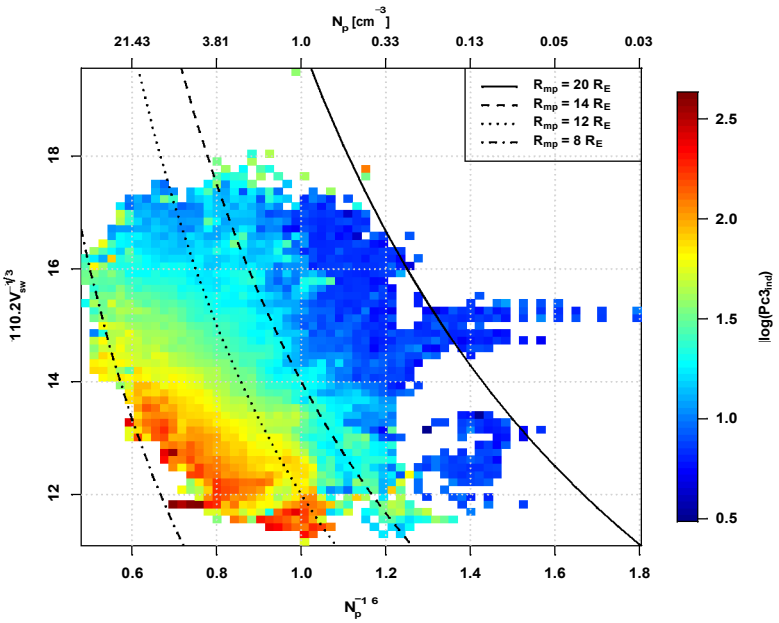

Figure 6.7: The influence of R_{mp} on $110.2(N_p V_{sw}^2)^{-1/6}$ on pulsation intensity is illustrated by plotting $Pc3_{ind}$ versus $N_p^{-1/6}$ (horizontal axis) and $110.2 V_{sw}^{-1/3}$. Black curves denote isolines of constant R_{mp}.

Low N_p decreases the Mach number of the bow shock ($M_A \propto V_{sw} \sim N_p/20 B_{IMF}$, see equation 4.3). Low Mach number inhibits the efficacy of particle reflection from the shock [Burgess,

1995]. In Figure 6.8 the influence that the Alfvén Mach number has on $Pc3_{ind}$ is demonstrated, in similar fashion to Figure 6.6, by a scatter plot (top panel), 95th percentile plot (middle panel), and the means and medians at percentile and regular (0.5) intervals of observed M_A (bottom panel). Only the $0 < M_A \leq 20$ range is plotted. The range of observed M_A stretches from 0.33 to 893.5, but 96% of observations fall in the $M_A < 20$ range. Maximum

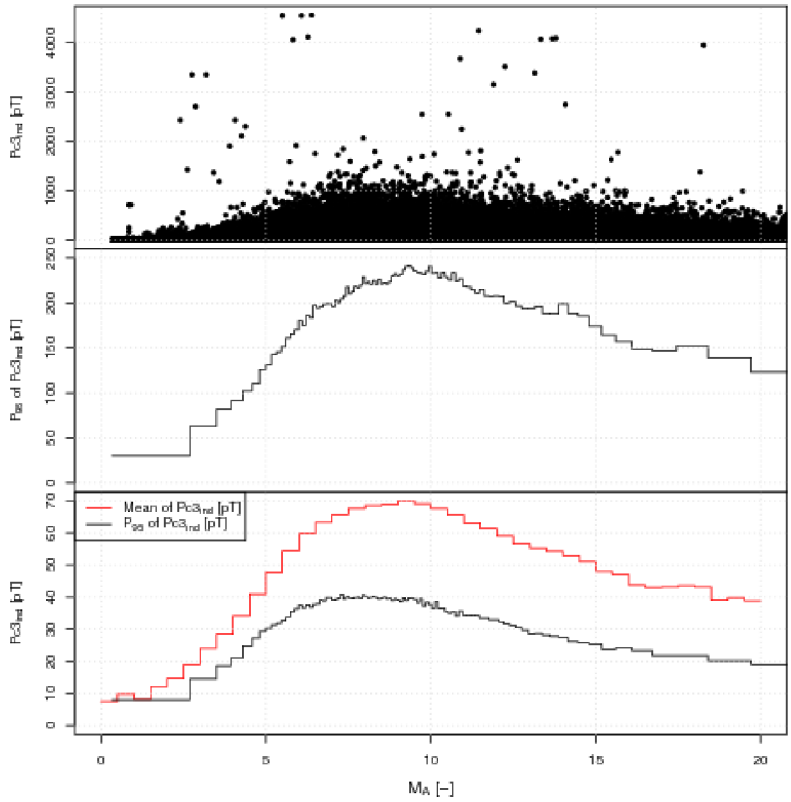

Figure 6.8: Pulsation intensity compared to Alfvénic Mach number. In the top panel $Pc3_{ind}$ is plotted against M_A. The second panel shows the 95th percentile (P_{95}) of $Pc3_{ind}$ for 1% intervals of M_A. In the third panel the median (P_{50}) of $Pc3_{ind}$ is computed at 1% intervals (black curve) and the mean of $Pc3_{ind}$ for regular (0.5 in width) intervals of M_A is plotted in red.

$Pc3_{ind}$ is observed near $M_A = 10$ and below 10 the 95th percentile, mean and median values of $Pc3_{ind}$ decreases to their respective minima at 30.27, 7.95, and 7.44 pT, respectively. In Figure 6.9 the control of $Pc3_{ind}$ by N_p through the Mach number is plotted by separating $M_A \approx N_p V_{sw}/20 B_{IMF}$ (equation 4.3) into N_p and $V_{sw}/20 B_{IMF}$, and plotting the mean of $\log_{10}(Pc3_{ind})$ (colour scale) versus N_p (horizontal axis) and $V_{sw}/20 B_{IMF}$ (vertical axis). Black curves indicate the contours at $M_A = 5$, 10 and 20. Above $M_A = 20$ mean $\log_{10}(Pc3_{ind})$

is erratic and no clear dependence of $Pc3_{ind}$ on M_A is visible. This is due to the relative rarity of $M_A > 20$ observations (only about 4% of the total data set), and hence the means of $\log_{10}(Pc3_{ind})$ in this range of M_A are calculated from relatively few observations. The peak values of $\log_{10}(Pc3_{ind})$ are observed near $M_A = 10$, rising from $M_A = 20$ to 10, and decreasing again as M_A --+ 0. Figure 6.10 shows the same plot as in Figure 6.9, but only for the $0 < M_A < 20$ range, and a 100 x 100 grid is used for the quilt plot. Between $M_A = 10$ and 20 the mean $Pc3_{ind}$ is 57 pT and average $Pc3_{ind}$ in the $5 < M_A < 10$ range is 64 pT. From $M_A = 5$ pulsation intensity is diminished with decreasing M_A. Average $Pc3_{ind}$ for $3 < M_A < 5$, $1 < M_A < 3$, and $0 < M_A < 1$ is 34 pT, 14 pT, and 9 pT, respectively.

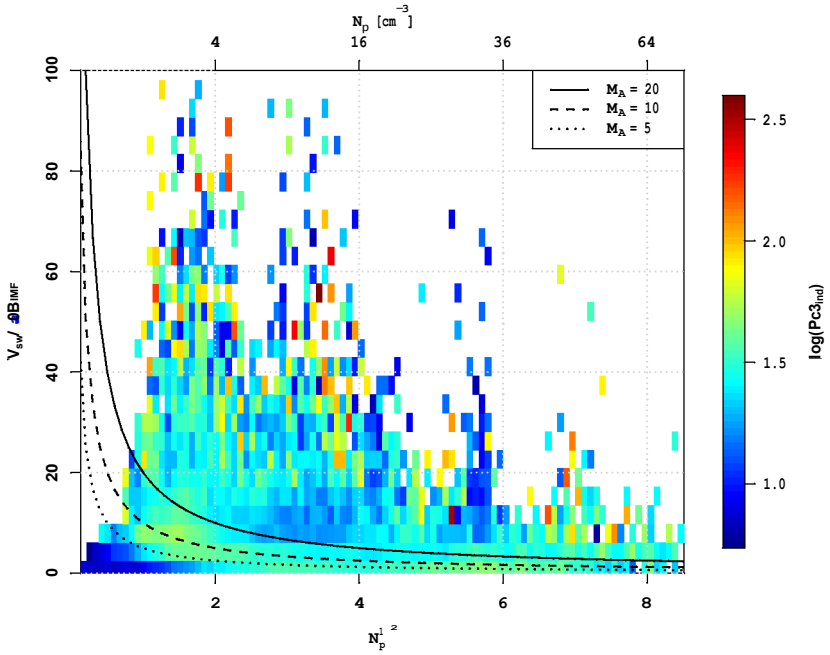

Figure 6.9: The influence of M_A V_{su}, $N_p/20B_{IMF}$ on pulsation intensity is illustrated by plotting $Pc3_{ind}$ versus N_p (horizontal axis) and $V_{su}/20B_{IMF}$. Black curves denote isolines of constant M_A.

ULF waves in the foreshock region are generated by an ion-cyclotron plasma instability that is excited when beams of ions reflected from the bow shock counter-stream with the incident solar wind [e.g. Treumann and Baumjohann, 1997a]. Barnes [1970], among others [e.g. Gary, 1991], showed that the wave activity generated by the beam instability is limited by the speed (V_b) and density (N_b) of the upstream directed ion beam, and that beam density and speed are proportional to the density and speed of the solar wind. Ions reflected off the bow shock wave form beams of ions that propagate in the upstream direction approximately along

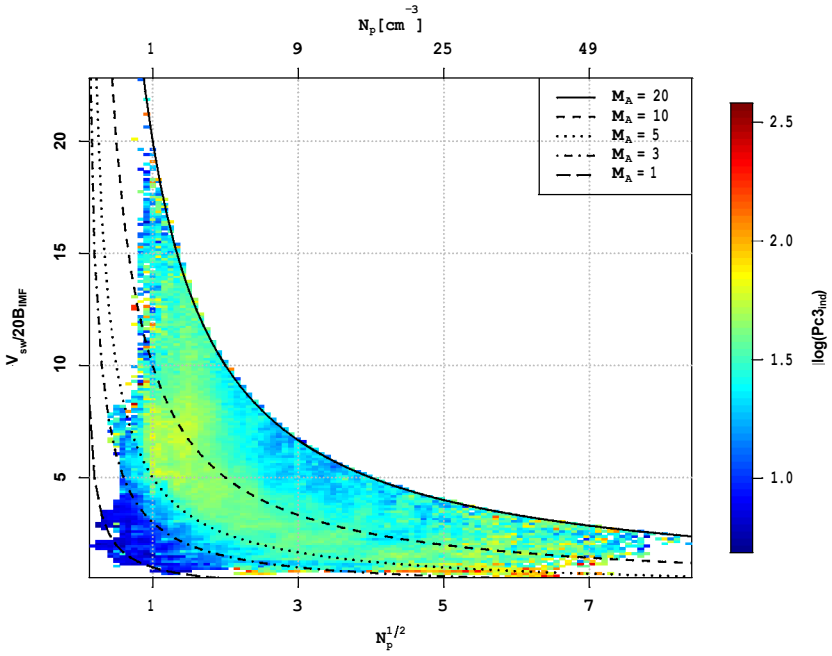

Figure 6.10: The pulsation index (colour scale) is plotted against $\sim N_p$ (horizontal axis) and $V_{su,}/20\,B_{IM\,F}$ (vertical axis) to illustrate the effect of M_A on Pc3 activity. This plot is similar to Figure 6.9 but here only the $M_A < 20$ range is shown. Black curves indicate constant M_A.

IMF lines with density $N_b - 0.01 N_p$ and speed V_b sai $2 - 3_{Vsu,}$ [Gary, 1991]. The strength ($N_b V_b$) of the ion beam determines the amount of free energy available for transfer to the ULF waves that are excited by the relative motion between the upstream moving beam and the downstream propagating solar wind plasma and hence upstream wave power may be limited by the solar wind density [e.g. Treumann and Baumjohann, 1997a; Potapov and Mazur, 1994]. In Figure 6.11 a scatter plot of $_{Pc3_{ind}}$ versus $N_{p\ Vsu,}$ is made (top panel), the 95th percentile levels of $_{Pc3_{ind}}$ at 1% intervals of $N_{p\ Vsu,}$ are plotted in the second panel and in the third panel the median of $_{Pc3_{ind}}$ is plotted for each 1% subset and mean $_{Pc3_{ind}}$ is plotted for regular intervals of $N_{p\ Vsu,}$. Pulsation intensity does not vary much with $N_{p\ Vsu,}$ but decreases significantly as $N_{p\ Vsu,}$ decreases from 2000 km.s^{-1}.cm^{-3} toward 0. The decrease in $_{Pc3_{ind}}$ with decreasing $N_{p\ Vsu,}$ is visible in the quilt plot of $_{\log10(Pc3_{ind})}$ versus N_p and $_{Vsu,}$ (Figure 6.12). This is the same plot as in Figure 6.4(b), but limited to the $N_p < 10$ cm^{-3} range. Black contour lines indicate $N_{p\ Vsu,}$ at 200, 500, 1000, and 2000 km.s^{-1}.cm^{-3}. Pulsation intensity is clearly dependent on both N_p and $_{Vsu,}$, but does not follow the $N_{p\ Vsu,}$ contours as closely as with $_{Rmp}$ and M_A.

Figures 6.7, 6.9 and 6.12 illustrate the dependence of $_{Pc3_{ind}}$ on solar wind density due

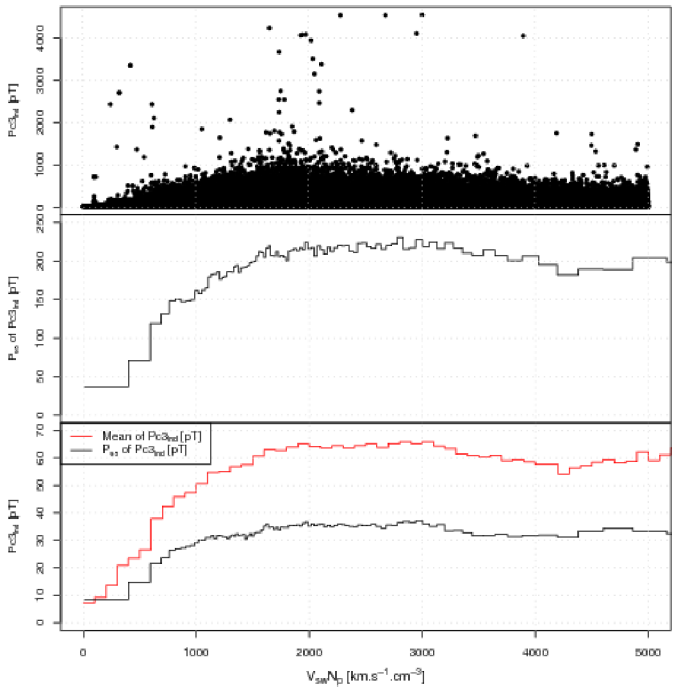

Figure 6.11: Pulsation activity is compared with beam density ($N_b V_b - N_{p\,Vsw}$) by plotting $Pc3_{ind}$ versus $_{VswNp}$. As in Figures 6.6 and 6.8 the first panel contains a scatter plot, the second panel is the 95th percentile of $_{Pc3_{ind}}$ and in the third panel the means (red curve) and medians (black curve) of $_{Pc3_{ind}}$ are plotted.

to the size of the magnetosphere (through $_{Rmp}$), the reflection of ions and the downstream convection of waves (M_A), and the power of the upstream propagating waves excited by the plasma instability (via beam strength $N_b V_b - N_p V_{sw}$). The individual importance of each mechanism is not easily separable without a detailed analysis incorporating multiple points of observation inside and outside the magnetosphere. However, based on the chain of events that results in upstream waves driving pulsation activity on the ground, it is reasonable to suggest that the increased size of the magnetosphere is not the primary inhibitor of Pc3 intensity. Beam reflection (determined by the Mach number of the shock), wave excitation by the ion cyclotron instability, and downstream convection of upstream propagating waves has to occur before the size of the magnetosphere has an influence on the amplitude of Pc3's. This suggests that the pause in Pc3 activity during low N_p intervals is primarily due to three reasons: (i) a low Mach number bow shock (characterised by M_A in the upstream solar wind) results in less efficient reflection of ions from the shock, (ii) the weakened ($N_b V_b$ low) beam only generates weak upstream propagating waves, and (iii) the low Mach number solar wind

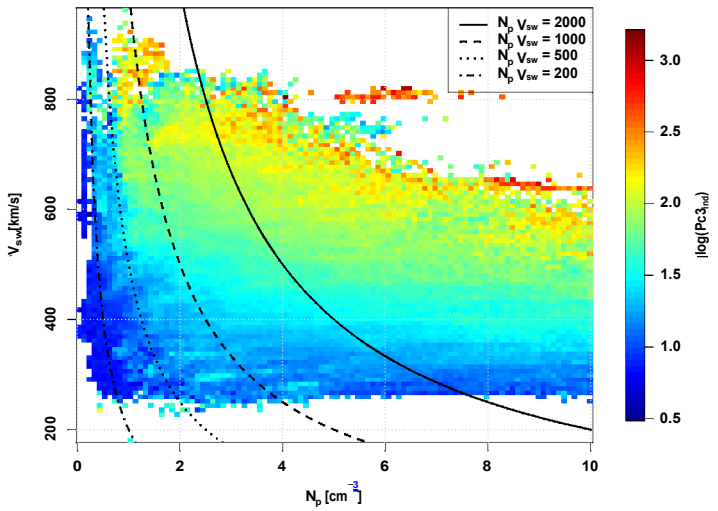

Figure 6.12: Pulsation index is compared with $_{Vsw}$ and N_p, with black curves indicating constant $N_{p\,Vsw}$. Only the $N_p \leq 10$ cm^{-3} range is shown.

is not able to convect the upstream waves downstream.

Low Mach number results in a weakened shock with decreased efficacy of particle reflection. Onsager et al. [1990] detected ion beams reflected off the bow shock for a wide range of Mach numbers (2 ≤ M_A ≤ 15), and Krauss-Varban and Omidi [1991] confirmed the observation of ion beams at $M_A \geq 2$. In their investigation of upstream wave activity on day 131 of 1999, when $N_p < 1$ cm^{-3} for most of the day, Le et al. [2000a] observed upstream wave activity at very low (≤ 1) magnetosonic Mach number. Figure 6.1 shows that the pulsations cease while $M_A > 1$ – while beam reflection off the shock is possible. Furthermore, Figure 6.9 shows that average $_{Pc3_{ind}}$ is near 10 pT for $M_A < 3$. Since particles are still reflected near $M_A = 2$, while the pause in Pc3's are observed, the non-reflection of particles from the shock may not be the primary cause of the pause in Pc3's while N_p is low.

Krauss-Varban and Omidi [1991] used a hybrid simulation of the foreshock wave activity for 1.5 < M_A < 3.2 and found that dominant wave structures shift from phase-standing whistlers to magnetosonic waves with downstream directed group velocity.

Furthermore, the group velocity of the whistler waves in the shock frame are only Doppler-shifted to the downstream direction for $M_A \geq 2.3$ [Krauss-Varban and Omidi, 1991]. This figure agrees with the observations of $_{Pc3_{ind}}$ at low M_A – mean and median $_{Pc3_{ind}}$ observed

while $M_A < 2.3$ is 10.83 pT and 7.42 pT, respectively. Although no clear threshold in the level of $_{Pc3_{ind}}$ near $M_A = 2.3$ is observed, a significant decrease in mean $_{\log10(Pc3_{ind})}$ is visible just below $M_A = 3$ in Figure 6.9. This may indicate that solar wind plasma with $M_A > 3$ is a necessary condition for the downstream convection of ULF waves.

6.4 Growth Rate Derivation

The beams of reflected ions counter-streaming with the incident solar wind plasma excites ion-cyclotron waves, with wave growth driven by the free energy made available by the motion of the ions. The rate of wave growth is defined as the complex part (γ) of the wave frequency (ω_r is the real part):

$$\omega = \omega_r + i\gamma. \tag{6.6}$$

Barnes [1970] used stochastic acceleration theory to derive an order of magnitude approximation of the fluctuation intensity in magnetic field magnitude in the foreshock region and found that the root-mean-square of the fluctuating component of the field is determined by beam strength ($N_b V_b$) and the Alfvén speed. Gary [1991] calculated that the maximum growth rate (γ_m) is proportional to the 1/3-rd power of N_b, but assumed a high Mach number shock ($M_A \sim 1$). Under low density conditions the Mach number is near 1, so this approximation is not valid for this investigation. In this section the growth rate of the upstream propagating ion-cyclotron waves is calculated, using the general dispersion relation derived by Gary [1991].

A homogeneous foreshock plasma is assumed, and the z axis defined as the direction of the magnetic field (with magnitude B_0):

$$\mathbf{B_0} = B_0\hat{\mathbf{z}}. \tag{6.7}$$

The plasma has three components, each with a Maxwellian distribution: a background of cool electrons (e) and core ions (c), and a warm ion beam (b). The following quantities for components $j = e, c, b$ are derived: thermal velocity of component j is

$$v_{th,j} = \tilde{} \; k_B T_j / m_j \; \tilde{}^{1/2} \tag{6.8}$$

with k_B Boltzmann's number, T_j the temperature, and m_j the mass. The bulk velocity of each

component is $\mathbf{v}_{0j}$. The number density of population j is N_j, and the plasma frequency is

$$\omega_j = \sqrt{\frac{4\pi N_j e^2}{m_j}} \tag{6.9}$$

with e the elementary charge. The gyrofrequency is

$$\Omega_j = \frac{e B_0}{m_j c} \tag{6.10}$$

with c the speed of light.

A tenuous beam ($N_b \sim N_c$) of ions propagating upstream along the IMF against a background of solar wind electrons and ions is considered. Gary [1991] derived the linear electromagnetic dispersion relation for parallel propagation ($\mathbf{k} \times \mathbf{B}_0 = 0$). The growth rate of the right-hand ion beam instability is derived. Assuming all three components ($j = e, c, b$) are isotropic in their own frames:

$$\omega^2 - k^2 c^2 + k^2 c^2 \sum_j S^{\pm}(\mathbf{k}, \omega) = 0 \tag{6.11}$$

with

$$S^{\pm} = \frac{\omega_j^2}{k^2 c^2} \zeta_j Z(\zeta_j^{\pm}) \tag{6.12}$$

the (dimensionless) conductivity of component j. The plasma dispersion function [Fried and Conte, 1961] is

$$Z(\zeta) = \pi^{-\pi} \int_{-\infty}^{\infty} \frac{\exp(-t^2)}{t - \zeta} \, dt \tag{6.13}$$

with argument ζ the ratio of wave phase speed to thermal speed, defined for each component j:

$$\zeta_j = \frac{\omega - \mathbf{k} \cdot \mathbf{v}_{0j}}{\sqrt{2} |k_z| v_{th,j}} \tag{6.14}$$

$$\zeta_j^{\pm} = \frac{\omega - \mathbf{k} \cdot \mathbf{v}_{0j} \pm \Omega_j}{\sqrt{2} |k_z| v_{th,j}}, \tag{6.15}$$

and

$$v_{th,j} = \sqrt{\frac{k_B T_j}{m_j}} \tag{6.16}$$

the thermal speed. The $\pm$ denotes right (+) or left-handed (−) polarisation. Since a warm

beam population is assumed, $v_{th,b}$ is comparable to the phase speed and hence ζ_b is small. The cold electron and core ion populations have large ζ, and the warm beam component has small ζ:

$$\zeta_j^{\pm} \sim 1, \text{ for } j = e, c \tag{6.17}$$

$$\zeta_b^{\pm} \leq 1 \tag{6.18}$$

The series expansions of $Z(\zeta)$ for the large and small arguments are [Fried and Conte, 1961]

$$Z(\zeta) = \begin{cases} i\sqrt{\pi}\exp(-\zeta^2) - \zeta^{-1}(1 + 1/2\zeta^2 + \ldots) & \text{for } |\zeta| \sim 1 \\ i\sqrt{\pi}\exp(-\zeta^2) - 2\zeta(1 - 2\zeta^2/3 + \ldots) & \text{for } |\zeta| \leq 1 \end{cases} \tag{6.19}$$

Using the expansions for $\zeta_{e,c}^+ \sim 1$ and $\zeta_b^+ \leq 1$ the dispersion relation (6.11) becomes

$$\omega^2 - k^2c^2 + \omega_e^2\zeta_e\left[i\sqrt{\pi}\exp\left(-\zeta_e^{+2}\right) - 1/\zeta_e^+ + \ldots\right] + \omega_c^2\zeta_c\left[i\sqrt{\pi}\exp\left(-\zeta_c^{+2}\right) - 1/\zeta_c^+ + \ldots\right] + \omega_b^2\zeta_b\left[i\sqrt{\pi}\exp\left(-\zeta_b^{+2}\right) - 2\zeta_b^+ + \ldots\right] = 0 \tag{6.20}$$

The electron and core ion terms (subscripts e and c) may be approximated by noting that $\exp(-\zeta_{e,c}^{+2}) \approx 0$, since a cold background plasma is assumed. The electron terms $\omega_e^2\zeta_e/\zeta_e^+$ are expanded in ω around $\omega = 0$:

$$\begin{aligned} \omega_e^2\zeta_e\left[i\sqrt{\pi}\exp\left(-\zeta_e^{+2}\right) - 1/\zeta_e^+ + \ldots\right] &\approx -\omega_e^2\zeta_e/\zeta_e^+ \\ &= -\omega_e^2\frac{\omega - k_z v_{0e}}{\omega - k_z v_{0e} + \Omega_e} \\ &= -\omega_e^2\left[\frac{k_z v_{0e}}{k_z v_{0e} - \Omega_e} + \ldots\right] \end{aligned} \tag{6.21}$$

and the same expansion of the c terms are made about $\omega = 0$:

$$\omega_c^2\zeta_c\left[i\sqrt{\pi}\exp\left(-\zeta_c^{+2}\right) - 1/\zeta_c^+ + \ldots\right] \approx -\omega_c^2\left[\frac{k_z v_{0e}}{k_z v_{0c} - \Omega_c} + \ldots\right] \tag{6.22}$$

The beam (b) terms in (6.11) are expanded similarly, and the approximation $\exp(-\zeta_b^{+2}) = 1$

is made since the small argument is assumed (equation 6.18):

$$\omega_b^2\zeta_b\left[i\sqrt{\pi}\exp\left(-\zeta_b^2\right)-2\zeta_b+\ldots\right] = \omega_b^2\frac{\omega-k_z v_{0b}}{\sqrt{\pi}2|k_z|v_b}\left[i\sqrt{\pi}-\frac{1}{2}\left(\frac{\omega-k_z v_{0b}+\Omega_b}{\sqrt{\pi}2|k_z|v_b}\right)^2+\ldots\right] \quad (6.23)$$

Higher order terms in equations 6.21, 6.22 and 6.23 are neglected, yielding the dispersion relation

$$\omega^2-k^2c^2-\omega_e^2\frac{k_z v_{0e}}{k_z v_{0e}-\Omega_e}-\omega_c^2\frac{k_z v_{0c}}{k_z v_{0c}-\Omega_c} +\omega_b^2\frac{\omega-k_z v_{0b}}{\sqrt{\pi}2|k_z|v_b}\left[i\sqrt{\pi}-2\frac{\omega-k_z v_{0b}+\Omega_b}{\sqrt{\pi}2|k_z|v_b}\right]=0 \quad (6.24)$$

The real and imaginary parts of the frequency ω is substituted into equation 6.24 by $\omega \rightarrow w_r + i\gamma$. Solving the imaginary part of (6.24) for γ yields the growth rate

$$\gamma=\frac{\sqrt{\frac{\pi}{2}}k_z v_b\omega_b^2(k_z v_{0b}-\omega_r)}{2v_b^2k_z^2\omega_r-2\omega_b^2(\omega_r-k_z v_{0b}+\Omega_p)+\omega_b^2\Omega_p}. \quad (6.25)$$

Measured solar wind parameters may be used to calculate the growth rate for different solar wind conditions. Solar wind speed (V_{sw}), temperature (T) and proton density (N_p) measured in the upstream solar wind are used as the core ion parameters and beam speed ($V_b = 2V_{sw}$), density ($N_b = 0.01N_p$) and temperature ($T_b = 10T$, since a warm beam and a cool background of ions is assumed) are calculated from these measurements. The measured solar wind parameters and the corresponding beam parameters (in cgs units) are listed in Table 6.3. In Figure 6.13 the growth rate is plotted against wave number k_z, for solar wind parameters measured during intervals of low and moderate density. The solid curve indicates growth rate calculated with solar wind parameters measured at 07:16 UT on day 27 of 2003 (see Figure 6.1), before the pause in Pc3 activity due to low N_p; the dashed curve indicates growth rate at 10:42 UT, during the low density interval. Solar wind measurements of IMF magnitude, speed, density and temperature at the two instances are listed in the figure.

Clearly the decrease in density from $N_p = 2.82$ cm^{-3} to $N_p = 0.67$ cm^{-3} is detrimental to the growth rate of the wave. The solar wind speed remains approximately constant (516 km.s^{-1} to 508 km.s^{-1}) and a large increase in temperature is observed. Increased beam temperature is conducive to wave growth [Treumann and Baumjohann, 1997a], but even with the increase in

beam temperature from 07:16 UT to 10:42 UT wave growth is inhibited by low beam density. This result agrees with work by Gary [1991] and Potapov and Mazur [1994], who showed that lowering the beam density results in decreasing γ (for $M_A >> 1$).

Table 6.3: Solar wind parameters at 07:16 and 10:42 UT on day 27 of 2003.

Par	07:16	10:42	Units
B_{IMF}	10.4	11.3	nT
V_{sw}	516	508	$km.s^{-1}$
T	20152	37954	°K
N_p	2.82	0.67	cm^{-3}
Par	**07:16**	**10:42**	**Units (cgs)**
B	1.04×10^{-4}	1.13×10^{-4}	G
V_{0b} $(3V_{sw})$	1.548×10^{8}	1.526×10^{8}	$cm.s^{-1}$
T_b $(10T)$	17.36	32.70	eV
N_b $(0.01N_p)$	0.0282	0.0067	cm^{-3}

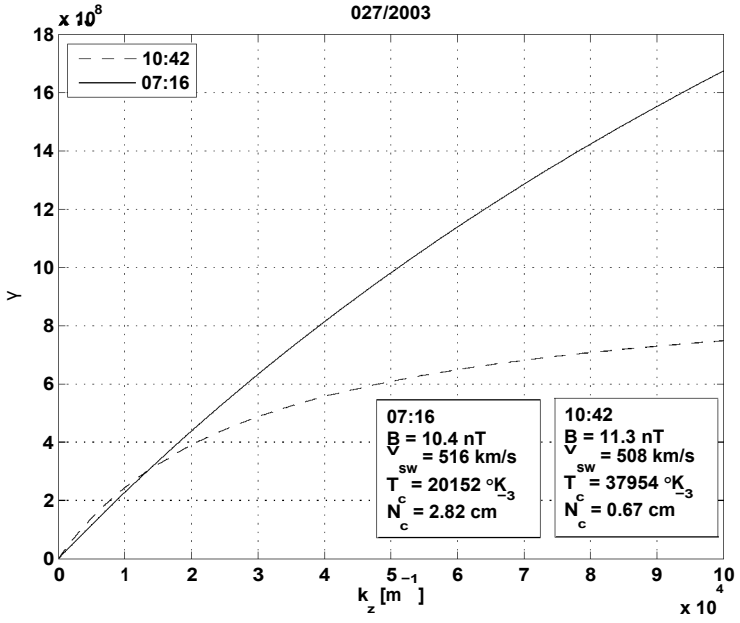

Figure 6.13: Growth rate γ (equation 6.25) plotted against wavenumber k_z with arguments specified using solar wind conditions at two times during day 27 of 2003 (07:16 and 10:42 UT).

6.5 Conclusions

In an attempt to identify the mechanism(s) responsible for the pause in pulsation activity at low density intervals, the pulsation index $Pc3_{ind}$ is plotted against M_A, $_{R,np}$, and $N_{p\ Vsu,}$. It is suggested that increased $_{R,np}$ may not be the primary inhibitor of Pc3 because the effect of low M_A and a weak reflected ion beam affects the upstream wave growth and downstream convection before wave propagation in the magnetosphere takes place. The influence that N_p and $_{Vsu,}$ has on Pc3 activity through M_A is clearly illustrated by the three dimensional quilt plot (Figure 6.10). Pc3 intensity decreases with M_A and the level of M_A below which mean $Pc3_{ind}$ is near 10 pT ($M_A \approx 3$) corresponds well to the figure ($M_A = 2.3$) calculated by Krauss-Varban and Omidi [1991], below which upstream travelling waves are not Doppler-shifted into the downstream direction by the solar wind. In the last section of this chapter the growth rate of the right-handed ion beam mode wave is calculated analytically. Solar wind measurements at a low (0.67 cm^{-3}) and average (2.82 cm^{-3}) density are used as arguments to the growth rate expression and it is shown that γ is significantly lower under low density than under average conditions. The work in this chapter suggests that low solar wind density results in a pause in pulsation activity because a weak beam causes weakly growing upstream waves, and the downstream convection of these waves is inhibited by a low Mach number solar wind plasma.

Chapter 7

Summary and Conclusions

The goal of this thesis was to investigate the solar wind control of Pc3 pulsation activity on the Earth. To accomplish this, two empirical models were developed to predict Pc3 activity from solar wind plasma, IMF, and UT-derived input parameters. For the first time artificial neural networks were employed to predict Pc3 activity from solar wind data. The intensity of Pc3 activity was measured by the pulsation index ($Pc3_{ind}$). All input parameters, except the two pairs of time-derived variables ([hrs, hrc] used in Chapter 4 and [χ, χ'] used in Chapter 5) are derived from measurements of the solar wind plasma and the IMF taken upstream of the bow shock. These measurements are shifted in time to account for downstream propagation up to the bow shock nose. Finally, the influence of solar wind density on $Pc3_{ind}$ was analysed.

7.1 Summary of the Work

In Chapter 4 an ANN based model was developed to predict 1-hour averages of the pulsation index measured at THY, from solar wind and time-derived input parameters. The model utilised hourly averaged data from day 76 to 105 of 2002, and day 1 to 365 of 2003. The correlation between the solar wind and IMF parameters, and the pulsation index was calculated and confirmed the dependence of pulsation amplitude on V_{sw} [Saito, 1964] and cone angle [Kovner et al., 1976; Greenstadt and Olson, 1976]. Since a number of solar wind parameters were measured, it was necessary to identify which of these parameters would optimally reproduce the desired output ($Pc3_{ind}$). To this end an iterative input parameter selection process was employed to select a subset of inputs from a set of 8 candidate input parameters. The input parameters of this model are, ranked in order of emergence from the modelling process,

solar wind speed (V_{sw}), sine and cosine of UT hour of the day (hrs, hrc), dynamic solar wind pressure (P_d), and cone angle (V_{B_x}). This results in a fully connected feed forward ANN with 5 input nodes, 11 hidden nodes in a single hidden layer, and one output node. The output of the low resolution model correlates well with the measured output, but much of the variability in $Pc3_{ind}$ is lost in the averaging to 1-hour resolution.

A second ANN based model of the solar wind influence on Pc3 activity was developed. This model utilised 5-minute running averages of 1-minute solar wind and Pc3 data. The use of the higher resolution datasets enabled this model to account for short term variations in Pc3 intensity. It is known that no significant Pc3 activity occurs on the night side of the Earth, and the low resolution model confirmed the expected dependence of $Pc3_{ind}$ on the time of the day. Thus, only data measured during local day time were employed in the development of this model. The reduction in data due to the exclusion of night side measurements concentrates the modelling effort on day side phenomena, i.e. night time data does not interfere with the modelling process. Due to the high time resolution the propagation time of perturbations through the magnetosheath and the magnetosphere was calculated and the $Pc3_{ind}$ measurements were shifted in time with respect to the solar wind data. The correlation between pairs of parameters was calculated and confirmed the known relationships between Pc3 activity and V_{sw} and V_{Bx}. The same iterative input parameter selection process employed in the development of the low resolution model was used to identify the set of inputs that optimally predicts $Pc3_{ind}$. Four input parameters were identified as the optimal set. In order of emergence from the iterative selection process, they are V_{sw}, V_{Bx}, N_p and the time derived pair [X, $\dot{X}$]. In the low resolution model cone angle was the last input to emerge from the set of candidates, but in the high resolution model the cone angle was identified as the second most influential input parameter. This difference is due to the shorter time resolution utilised in the second ANN model. For the first time the time scale at which these parameters influence Pc3 activity was identified. It was observed that solar wind speed and density determines the Pc3 intensity over long (multiple hour) intervals, while over short time intervals (sub-1 hour) cone angle largely determines the variations in $Pc3_{ind}$. This is due to the difference in the typical time scales of variation of these parameters. To demonstrate this the average rise and fall times of V_{sw}, N_p, and V_{Bx} were calculated. Cone angle was found to vary between its 10th and 90th percentile levels over about 40 minutes, while N_p and V_{sw} took much longer ($\sim$ 1000 minutes) to achieve the same variation.

During intervals of anomalously low solar wind density (below about 1 cm^{-3}) it was observed that Pc3 activity ceases almost completely, resulting in observations of $Pc3_{ind}$ that are near the noise level of the instrument used to measure the field. This pause in activity was observed in coincidence with high solar wind speed and small cone angle – conditions which are usually favourable to the generation of Pc3's. In the sixth chapter of this thesis the influence of solar wind proton density N_p on pulsation intensity was studied by analysing a large set of solar wind and Pc3 data, measured at one minute intervals between 2002 and 2005. The dataset of pulsation index measurements is log-normally distributed indicating that multiplicative processes, rather than additive processes are involved in the generation of Pc3's. The influence that N_p has on pulsation activity through (i) the size of the magnetosphere (via $_{Rmp}$), (ii) the reflection of particles from the bow shock and the downstream convection of upstream propagating waves (via M_A), and (iii) the strength of the upstream propagating beam of ions, was analysed. All these effects could be understood through Pc3's generated by the upstream wave mechanism. The chain of events that lead to Pc3's suggests that the size of the magnetosphere does not play the primary role in the cessation of Pc3's under low N_p. The effect that M_A has on $Pc3_{ind}$ is clear, but only while M_A is low ($\lesssim 10$). This agrees with work by Krauss-Varban and Omidi [1991] who suggested that below $M_A = 2.3$ waves are not convected downstream. The effect that $N_{p\ Vsw}$ (beam strength) has on $Pc3_{ind}$ was demonstrated through the calculation of the growth rate of the upstream propagating waves generated by the ion beam instability at low and average values of N_p. The growth rate was found to be significantly lower for low N_p, indicating that decreased ULF power should be expected in the foreshock while the solar wind density is low. Furthermore, the observed dependence of $Pc3_{ind}$ on M_A suggested that ULF waves may not be convected back downstream, even if V_{sw} is high and ϑ_{Bx} is small.

7.2 Future Work

There are several possibilities for the future development of this work. Firstly, other extra-magnetospheric input parameters such as the F10.7 flux, which indicates MHD wave speeds in the ionosphere, may be included in future models. The high resolution model may be extended to many ground-based stations in order to study the latitudinal variation in the solar wind – Pc3 relationship. Data from the MM100 [Heilig et al., 2007] array may be employed to develop a separate prediction model for each station. In this way a regional Pc3 activity modelling framework may be set up. In the case of high latitude stations other input parameters

like the IMF clock angle, which determines the cusp position, maybe included in the analysis.

It may be insightful to calculate the pulsation index not only for the Pc3 band of frequencies, but to divide a wide frequency band into a number of narrow bands and calculate the pulsation index (i.e. intensity of pulsation activity) separately for each narrow band. For example, the Pc2 – Pc4 bands that span from 0.007 Hz to 0.2 Hz may be divided into 10 bands of about 0.02 Hz each, so that 10 pulsation indices are defined. Each of these indices may be used as the output of an ANN based model with solar wind parameters as input. In this way the solar wind influence on geomagnetic pulsations may be studied at various frequency bands that are not determined by the usual Pc classes.

In order to study the time scales at which certain solar wind parameters influence Pc3 activity, the following procedure is suggested. Using multi-resolution analysis [e.g. Rohwer, 2005] a time series of $Pc3_{ind}$ data (**P**) maybe divided into multiple sets of data that represents **P** at various levels of sensitivity so that

$$\mathbf{P} = \mathbf{P}_1 + \mathbf{P}_2 + \cdots + \mathbf{P}_N \tag{7.1}$$

with $\mathbf{P}_i$ representing **P** at sensitivity level i. Each sensitivity level is tied to a time scale, so that, for example, $i = 1$ represents the 60 minute scale, $i = 2$ the 30 minute scale, and so on, at increasing levels of sensitivity. Each variable $\mathbf{P}_i$ may be used as the output of an ANN model. If the same model development procedure as in Chapters 4 and 5 is used the most influential solar wind parameters controlling Pc3 activity at various time scales will be identified.

7.3 Concluding Remarks

The first goal of this study, listed in Chapter 1, was to "create a modelling framework capable of predicting pulsation activity from solar wind data". For the first time neural network based models capable of predicting Pc3 activity from solar wind data were developed. The low resolution model predicted $Pc3_{ind}$ from unseen solar wind parameter measurements with a $\rho = 0.87$ correlation between measured and predicted output at 1 hour time resolution. However, much of the finer variability in $Pc3_{ind}$, especially due to fluctuations in the cone angle, is lost due to the low resolution of the hourly averaged data utilised in this model; and the smoothness of the data contributes to the high accuracy achieved by the low resolution

model. The high resolution model achieved prediction accuracy of $\rho = 0.68$ when predicting $Pc3_{ind}$ from unseen solar wind data. Although the accuracy of this model is lower than the low resolution model, the high variability and the sensitivity of Pc3 activity to changes in the cone angle are captured.

The second goal was to "determine which solar wind parameters drive pulsation activity". The parameter selection process used to develop the ANN models utilised the predictive capacity of the neural networks to select a set of most influential parameters to the Pc3 index. Furthermore, the order in which the input parameters are selected may be used to rank the importance of each parameter. In the development of the low resolution model the input parameters are, in order: the solar wind speed, the sine and cosine of UT hour of the day, the solar wind dynamic pressure, and the cone angle. The high resolution model ranks solar wind speed, cone angle, solar wind density, and the out of phase solar zenith angle pair as the most influential input parameters.

The last goal listed in Chapter 1 was to "infer the preferred generation mechanism of Pc3 pulsation activity". The input parameters selected in the development of the ANN models all suggest that the upstream wave mechanism is responsible for day side Pc3 pulsations. Furthermore, the influence that N_p has on $Pc3_{ind}$ suggests that the generation and downstream convection of upstream waves are inhibited by very low N_p. This explains the pause in Pc3 activity while $N_p \mathrel{\mathsf{N}} 1\ \mathrm{cm}^{-3}$.

The work in this thesis showed the extent of solar wind influence on day side Pc3 activity. The development of the ANN models highlighted the solar wind parameters responsible for Pc3 generation and the time scales on which those parameters operate. For the first time the influence of N_p on Pc3 activity is explicitly investigated and it is found that low N_p causes Pc3's to cease because of a weakened instability and the inability of the solar wind to convect waves downstream.

Appendices

Appendix A

Correlation Tables

The correlation (Pearson's ρ) is computed for every pair of solar wind parameters, and between the pulsation index ($Pc3_{ind}$) and the solar wind parameters. Data sets defined by the selection criteria ($K_p < 4$, $\chi < 90^{\circ}$) in Chapter 5.3.3 are used.

Table A.1: Pearson correlation coefficient between parameters for 2002.

2002	χ	χ'	V_{sw}	N_p	E	B	ϑ_{Bx}	P_d	M_A	β	$Pc3_{ind}$
χ	1.0000	-1.0000	0.0594	-0.0283	-0.0174	0.0610	-0.0035	0.0082	-0.0573	-0.0399	-0.1770
χ'	-1.0000	1.0000	-0.0594	0.0283	0.0174	-0.0610	0.0035	-0.0082	0.0573	0.0399	0.1770
V_{sw}	0.0594	-0.0594	1.0000	-0.3803	-0.0659	0.0378	-0.0967	0.0472	-0.0316	-0.1394	0.4119
N_p	-0.0283	0.0283	-0.3803	1.0000	-0.0908	0.2353	0.1314	0.8530	0.3791	0.3611	-0.0140
E	-0.0174	0.0174	-0.0659	-0.0908	1.0000	-0.3411	-0.1369	-0.1406	0.1257	0.0502	0.0274
B	0.0610	-0.0610	0.0378	0.2353	-0.3411	1.0000	0.1183	0.3318	-0.5968	-0.3156	-0.0035
ϑ_{Bx}	-0.0035	0.0035	-0.0967	0.1314	-0.1369	0.1183	1.0000	0.1030	-0.0110	-0.0062	-0.3599
P_d	0.0082	-0.0082	0.0472	0.8530	-0.1406	0.3318	0.1030	1.0000	0.3502	0.2791	0.2002
M_A	-0.0573	0.0573	-0.0316	0.3791	0.1257	-0.5968	-0.0110	0.3502	1.0000	0.7982	0.1067
β	-0.0399	0.0399	-0.1394	0.3611	0.0502	-0.3156	-0.0062	0.2791	0.7982	1.0000	0.0068
$Pc3_{ind}$	-0.1770	0.1770	0.4119	-0.0140	0.0274	-0.0035	-0.3599	0.2002	0.1067	0.0068	1.0000

Table A.2: Pearson correlation coefficient between parameters for 2003.

2003	χ	χ'	V_{sw}	N_p	E	B	ϑ_{Bx}	P_d	M_A	β	$Pc3_{ind}$
χ	1.0000	-1.0000	-0.0690	0.0062	-0.0432	0.0178	-0.0065	-0.0652	-0.0461	0.0049	-0.2249
χ'	-1.0000	1.0000	0.0690	-0.0062	0.0432	-0.0178	0.0065	0.0652	0.0461	-0.0049	0.2249
V_{sw}	-0.0690	0.0690	1.0000	-0.5167	-0.1064	-0.1306	-0.0157	0.0530	0.0890	-0.0891	0.4176
N_p	0.0062	-0.0062	-0.5167	1.0000	0.0201	0.2381	0.1057	0.7415	0.2817	0.2815	-0.1189
E	-0.0432	0.0432	-0.1064	0.0201	1.0000	-0.2367	-0.1069	-0.0831	0.0954	0.0430	0.0219
B	0.0178	-0.0178	-0.1306	0.2381	-0.2367	1.0000	0.1417	0.2855	-0.5998	-0.2519	-0.0536
ϑ_{Bx}	-0.0065	0.0065	-0.0157	0.1057	-0.1069	0.1417	1.0000	0.1316	-0.0239	-0.0220	-0.3611
P_d	-0.0652	0.0652	0.0530	0.7415	-0.0831	0.2855	0.1316	1.0000	0.3603	0.2427	0.1707
M_A	-0.0461	0.0461	0.0890	0.2817	0.0954	-0.5998	-0.0239	0.3603	1.0000	0.7484	0.1022
β	0.0049	-0.0049	-0.0891	0.2815	0.0430	-0.2519	-0.0220	0.2427	0.7484	1.0000	-0.0025
$Pc3_{ind}$	-0.2249	0.2249	0.4176	-0.1189	0.0219	-0.0536	-0.3611	0.1707	0.1022	-0.0025	1.0000

Table A.3: Pearson correlation coefficient between parameters for 2004.

2004	χ	χ'	V_{sw}	N_p	E	B	ϑ_{Bx}	P_d	M_A	β	$Pc3_{ind}$
χ	1.000	-1.000	-0.061	0.069	-0.019	0.012	0.002	0.061	0.048	0.056	-0.116
χ^*	-1.000	1.000	0.061	-0.069	0.019	-0.012	-0.002	-0.061	-0.048	-0.056	0.116
V_{sw}	-0.061	0.061	1.000	-0.362	-0.087	0.050	-0.101	0.161	-0.012	-0.132	0.422
N_p	0.069	-0.069	-0.362	1.000	-0.102	0.352	0.172	0.798	0.263	0.233	0.003
E	-0.019	0.019	-0.087	-0.102	1.000	-0.285	-0.040	-0.195	0.058	0.029	-0.033
B	0.012	-0.012	0.050	0.352	-0.285	1.000	0.082	0.443	-0.527	-0.304	0.069
ϑ_{Bx}	0.002	-0.002	-0.101	0.172	-0.040	0.082	1.000	0.113	0.032	0.026	-0.360
P_d	0.061	-0.061	0.161	0.798	-0.195	0.443	0.113	1.000	0.277	0.161	0.275
M_A	0.048	-0.048	-0.012	0.263	0.058	-0.527	0.032	0.277	1.000	0.838	0.087
β	0.056	-0.056	-0.132	0.233	0.029	-0.304	0.026	0.161	0.838	1.000	0.013
$Pc3_{ind}$	-0.116	0.116	0.422	0.003	-0.033	0.069	-0.360	0.275	0.087	0.013	1.000

Table A.4: Pearson correlation coefficient between parameters for 2005.

2005	χ	χ'	V_{sw}	N_p	E	B	ϑ_{Bx}	P_d	M_A	β	$Pc3_{ind}$
χ	1.0000	-1.0000	-0.0402	-0.0149	0.0180	-0.0014	0.0177	-0.0402	-0.0216	0.0075	-0.1422
χ^*	-1.0000	1.0000	0.0402	0.0149	-0.0180	0.0014	-0.0177	0.0402	0.0216	-0.0075	0.1422
V_{sw}	-0.0402	0.0402	1.0000	-0.4305	-0.0624	0.0585	-0.0414	0.0783	-0.0446	-0.1830	0.4310
N_p	-0.0149	0.0149	-0.4305	1.0000	-0.0774	0.3065	0.1333	0.8037	0.2621	0.2924	-0.0740
E	0.0180	-0.0180	-0.0624	-0.0774	1.0000	-0.2661	-0.1149	-0.1540	0.0766	0.0440	-0.0313
B	-0.0014	0.0014	0.0585	0.3065	-0.2661	1.0000	0.0968	0.4447	-0.5737	-0.3367	0.1189
ϑ_{Bx}	0.0177	-0.0177	-0.0414	0.1333	-0.1149	0.0968	1.0000	0.1214	0.0326	0.0270	-0.3604
P_d	-0.0402	0.0402	0.0783	0.8037	-0.1540	0.4447	0.1214	1.0000	0.2433	0.1848	0.2132
M_A	-0.0216	0.0216	-0.0446	0.2621	0.0766	-0.5737	0.0326	0.2433	1.0000	0.8295	-0.0104
β	0.0075	-0.0075	-0.1830	0.2924	0.0440	-0.3367	0.0270	0.1848	0.8295	1.0000	-0.0709
$Pc3_{ind}$	-0.1422	0.1422	0.4310	-0.0740	-0.0313	0.1189	-0.3604	0.2132	-0.0104	-0.0709	1.0000

Table A.5: Pearson correlation coefficient between parameters for 2006.

2006	χ	χ'	V_{sw}	N_p	E	B	ϑ_{Bx}	P_d	M_A	β	$Pc3_{ind}$
χ	1.00000	-1.00000	-0.00034	-0.04032	-0.01395	0.01889	0.00008	-0.05120	-0.03561	-0.01409	-0.11632
χ^*	-1.00000	1.00000	0.00034	0.04032	0.01395	-0.01889	-0.00008	0.05120	0.03561	0.01409	0.11632
V_{sw}	-0.00034	0.00034	1.00000	-0.49451	0.01007	0.07712	-0.11334	0.03546	-0.13801	-0.16999	0.47286
N_p	-0.04032	0.04032	-0.49451	1.00000	0.01122	0.28014	0.17275	0.79350	0.27796	0.26057	-0.14850
E	-0.01395	0.01395	0.01007	0.01122	1.00000	-0.12975	-0.06746	0.00384	0.06763	0.02243	0.04338
B	0.01889	-0.01889	0.07712	0.28014	-0.12975	1.00000	0.12485	0.48975	-0.56027	-0.25073	0.13327
ϑ_{Bx}	0.00008	-0.00008	-0.11334	0.17275	-0.06746	0.12485	1.00000	0.13845	0.02566	0.02951	-0.32941
P_d	-0.05120	0.05120	0.03546	0.79350	0.00384	0.48975	0.13845	1.00000	0.14996	0.12932	0.14824
M_A	-0.03561	0.03561	-0.13801	0.27796	0.06763	-0.56027	0.02566	0.14996	1.00000	0.80110	-0.09003
β	-0.01409	0.01409	-0.16999	0.26057	0.02243	-0.25073	0.02951	0.12932	0.80110	1.00000	-0.07625
$Pc3_{ind}$	-0.11632	0.11632	0.47286	-0.14850	0.04338	0.13327	-0.32941	0.14824	-0.09003	-0.07625	1.00000

Table A.6: Pearson correlation coefficient between parameters for 2007.

2007	χ	χ'	V_{sw}	N_p	E	B	ϑ_{Bx}	P_d	M_A	β	$Pc3_{ind}$
χ	1.0000	-1.0000	0.0212	-0.0010	-0.0179	-0.0063	-0.0027	0.0075	-0.0049	-0.0185	-0.1049
χ^*	-1.0000	1.0000	-0.0212	0.0010	0.0179	0.0063	0.0027	-0.0075	0.0049	0.0185	0.1049
V_{sw}	0.0212	-0.0212	1.0000	-0.4465	-0.0437	0.0584	-0.0653	0.0691	-0.1203	-0.2089	0.5223
N_p	-0.0010	0.0010	-0.4465	1.0000	-0.0411	0.3150	0.1656	0.8125	0.1886	0.2071	-0.1384
E	-0.0179	0.0179	-0.0437	-0.0411	1.0000	-0.1362	-0.0877	-0.0986	0.0448	0.0218	0.0179
B	-0.0063	0.0063	0.0584	0.3150	-0.1362	1.0000	0.1219	0.4956	-0.5780	-0.2802	0.1409
ϑ_{Bx}	-0.0027	0.0027	-0.0653	0.1656	-0.0877	0.1219	1.0000	0.1522	0.0244	0.0336	-0.3013
P_d	0.0075	-0.0075	0.0691	0.8125	-0.0986	0.4956	0.1522	1.0000	0.0640	0.0570	0.1660
M_A	-0.0049	0.0049	-0.1203	0.1886	0.0448	-0.5780	0.0244	0.0640	1.0000	0.8259	-0.0978
β	-0.0185	0.0185	-0.2089	0.2071	0.0218	-0.2802	0.0336	0.0570	0.8259	1.0000	-0.1029
$Pc3_{ind}$	-0.1049	0.1049	0.5223	-0.1384	0.0179	0.1409	-0.3013	0.1660	-0.0978	-0.1029	1.0000

Appendix B

Network Weights and Biases

Two neural network-based models are developed in this thesis. In Chapter 4 each round of neural network training in the model development process yields a "winning" network that defines the candidate input parameter to be added to the set of optimal inputs. These networks are NN number 3, 15, 18 and 25 from Table 4.4, with input parameters and number of hidden nodes indicated in the table. The same process is applied in Chapter 5 to yield a winner after each round of training. The winning networks in the development of the high resolution model are networks number 2, 12, 15, and 19 (see Table 5.3).

The weight and bias matrices of these networks are listed below with the number of input (K), hidden (L) and output (M) nodes indicated. Weight matrices are $\mathbf{W}^{(1)} = \{w^{(1)}_{i,j}\}$, with $i = 1, 2, \ldots, K\}$ and $j = \{1, 2, \ldots, L\}$, consisting of the weights connecting input node i with hidden node j; $\mathbf{W}^{(2)} = \{w^{(2)}_{i,j}$ with $i = 1, 2, \ldots, M\}$ and $j = \{1, 2, \ldots, L\}$ are weights connecting hidden node i with output node j. The bias vectors of each network are $\mathbf{b}^{(1)} = \{b^{(1)}_1, \ldots, b^{(1)}_i, \ldots, b^{(1)}_L\}$ listing biases in the activation function of each hidden node i, and $\mathbf{b}^{(2)} = \{b^{(2)}_1, \ldots, b^{(2)}_i, \ldots, b^{(2)}_M\}$ denotes the bias in the activation of output node i. The weights and biases of each network serve as arguments to the network equations (3.6 and 3.5) in chapter 3 to yield the predicted output.

B.1 Low Resolution Model

Network 3 with $K = 1$, $L = 3$, $M = 1$:

$$\mathbf{W}^{(1)} = \begin{bmatrix} -6.6764 \\ -1.0127 \\ 3.7880 \end{bmatrix} \tag{B.1a}$$

$$\mathbf{W}^{(2)} = \begin{bmatrix} 0.7408 & -0.2225 & -0.2431 \end{bmatrix} \tag{B.1b}$$

$$\mathbf{b}^{(1)} = \begin{bmatrix} 6.4018, & 0.4569, & 5.4734 \end{bmatrix} \tag{B.1c}$$

$$\mathbf{b}^{(2)} = \begin{bmatrix} -1.2716 \end{bmatrix} \tag{B.1d}$$

Network 15 with $K = 3$, $L = 7$, $M = 1$:

$$\mathbf{W}^{(1)} = \begin{bmatrix} 1.2255 & 0.2482 & 0.2468 \\ 0.3718 & -3.5964 & -0.1126 \\ 5.1273 & -0.4809 & 3.6719 \\ -0.8467 & -0.4863 & 0.4436 \\ -4.5940 & 10.4763 & -4.4310 \\ 1.5106 & -0.2275 & -0.0871 \\ 0.6976 & -8.6398 & -8.4873 \end{bmatrix} \tag{B.2a}$$

$$\mathbf{W}^{(2)} = \begin{bmatrix} -0.5052 & -0.0847 & -0.0271 & -0.4376 & -0.0068 & 0.1140 & 0.0224 \end{bmatrix} \tag{B.2b}$$

$$\mathbf{b}^{(1)} = \begin{bmatrix} -1.9745, & -3.6990, & -2.1589, & 1.3381, & -0.1598, & -0.2304, & -5.8211 \end{bmatrix} \tag{B.2c}$$

$$\mathbf{b}^{(2)} = \begin{bmatrix} -1.0421 \end{bmatrix} \tag{B.2d}$$

Network 18 with $K = 4$, $L = 9$, $M = 1$:

$$\mathbf{W}^{(1)} = \begin{bmatrix} 1.1074 & 0.0271 & -0.5891 & -5.9031 \\ 1.2882 & 2.0023 & -7.3003 & 0.3899 \\ 0.5774 & 0.1544 & -0.5017 & 0.3713 \\ -1.5298 & 1.9596 & 2.4927 & -2.0623 \\ 7.0347 & -2.6870 & -5.0443 & 7.6186 \\ 0.6810 & 11.9903 & -15.5371 & 1.9739 \\ -1.9039 & -3.1635 & -1.2873 & 0.0364 \\ 1.4377 & -2.3462 & -2.6616 & 1.5134 \\ 2.3791 & -0.4009 & 7.0361 & 0.1724 \end{bmatrix} \tag{B.3a}$$

$$\mathbf{W}^{(2)} = \begin{bmatrix} -1.9163 & -0.0310 & 4.4845 & 0.2149 & \cdots & \\ \cdots & -0.3032 & 0.0240 & 0.0070 & 0.2360 & 0.0344 \end{bmatrix} \tag{B.3b}$$

$$\mathbf{b}^{(1)} = \begin{bmatrix} -7.5244, 4.1014, -1.7720, -0.0314, -5.3457, \ldots \\ 3.9459, 0.8822, -0.7002, 4.8377 \end{bmatrix} \tag{B.3c}$$

$$\mathbf{b}^{(2)} = \begin{bmatrix} 1.2366 \end{bmatrix} \tag{B.3d}$$

Network 25 with $K = 5$, $L = 11$, $M = 1$:

$$\mathbf{W}^{(1)} = \begin{bmatrix} 0.8081 & 0.0763 & -0.4857 & -0.0377 & -0.6143 \\ -0.7358 & 0.0668 & 0.4136 & 2.3735 & 0.6259 \\ 0.4250 & -1.3051 & -0.1122 & 1.4968 & 0.4711 \\ -0.7852 & 1.4164 & 1.3247 & 1.5852 & -0.4308 \\ 0.1704 & -1.1183 & -0.2825 & -0.2267 & -2.2300 \\ -0.5254 & -0.2201 & 1.9003 & 0.6147 & 1.6818 \\ -1.1208 & 0.2254 & 0.8758 & 1.1072 & -1.5812 \\ -0.2759 & -0.4068 & 1.8066 & -0.3535 & 0.2206 \\ -0.1335 & -0.0503 & -0.5831 & -1.0591 & -1.7419 \\ 0.4937 & -0.2024 & 1.5982 & 0.2440 & 0.1309 \\ 0.3867 & 0.5844 & 1.5639 & 1.8526 & 3.7785 \end{bmatrix} \tag{B.4a}$$

$$\mathbf{W}^{(2)} = \begin{bmatrix} 1.6485 & 0.9589 & 0.0528 & 0.0409 & -0.0311 & \cdots \\ \vdots & & 0.0437 & -0.0512 & -0.1984 & 0.1003 & 0.1927 \end{bmatrix} \tag{B.4b}$$

$$\mathbf{b}^{(1)} = [-1.8665,\ 3.5820,\ 1.7353,\ -0.2429,\ -0.3531,\ldots \\ 0.3311,\ -0.0364,\ 0.3264,\ -0.5184,\ 1.2171,\ 3.7085] \tag{B.4c}$$

$$\mathbf{B}^{(2)} = [-0.2660] \tag{B.4d}$$

B.2 High Resolution Model

Network 2 with $K = 1$, $L = 3$, $M = 1$:

$$\mathbf{W}^{(1)} = \begin{bmatrix} 0.20419 \\ -0.17021 \\ -2.27771 \end{bmatrix} \tag{B.5a}$$

$$\mathbf{W}^{(2)} = \begin{bmatrix} -2.69929 & -1.07872 & -0.79470 \end{bmatrix} \tag{B.5b}$$

$$\mathbf{b}^{(1)} = [-0.30468, 0.82592, -0.85267] \tag{B.5c}$$

$$\mathbf{b}^{(2)} = [-1.42946] \tag{B.5d}$$

Network 12 with $K = 2$, $L = 5$, $M = 1$:

$$\mathbf{W}^{(1)} = \begin{bmatrix} 0.88501 & 0.27587 \\ -0.61010 & -0.50033 \\ -1.51319 & -0.98987 \\ -0.44060 & 2.84285 \\ -2.14492 & -0.01499 \end{bmatrix} \tag{B.6a}$$

$$\mathbf{W}^{(2)} = \begin{bmatrix} 0.03933 & -1.05222 & -1.46100 & -1.83055 & -1.41226 \end{bmatrix} \tag{B.6b}$$

$$\mathbf{b}^{(1)} = \begin{bmatrix} 0.22229, & -0.81995, & -1.80919, & -0.79357, & -0.90051 \end{bmatrix} \quad \text{(B.6c)}$$

$$\mathbf{b}^{(2)} = \begin{bmatrix} -1.73750 \end{bmatrix} \quad \text{(B.6d)}$$

Network 15 with $K = 3$, $L = 7$, $M = 1$:

$$\mathbf{W}^{(1)} = \begin{bmatrix} 1.17172 & 0.01734 & 0.28980 \\ -0.12198 & 1.76197 & 2.56221 \\ 0.74044 & -0.04626 & 1.10082 \\ -2.07034 & -0.45589 & 0.32755 \\ 0.30596 & -0.25148 & 0.04201 \\ 0.92768 & -5.47925 & -0.03149 \\ -0.04529 & 0.23879 & -0.41917 \end{bmatrix} \quad \text{(B.7a)}$$

$$\mathbf{W}^{(2)} = \begin{bmatrix} 1.66782 & -1.98149 & 1.81594 & -3.64905 & 0.28102 & -5.39123 & -0.22113 \end{bmatrix} \quad \text{(B.7b)}$$

$$\mathbf{b}^{(1)} = \begin{bmatrix} -0.23986, & 0.90257, & 1.00375, & -0.44679, & 1.04155, & -6.12798, & -0.19914 \end{bmatrix} \quad \text{(B.7c)}$$

$$\mathbf{b}^{(2)} = \begin{bmatrix} -1.75891 \end{bmatrix} \quad \text{(B.7d)}$$

Network 19 with $K = 5$, $L = 11$, $M = 1$:

$$\mathbf{W}^{(1)} = \begin{bmatrix} 0.40683 & -0.27158 & -0.32960 & -0.51660 & -0.36814 \\ -0.86164 & 1.19094 & 0.66339 & -1.00748 & 0.69487 \\ -0.13343 & 0.20274 & 0.53920 & -1.27978 & -2.79658 \\ -0.12315 & -1.12322 & -0.45564 & -1.53164 & -0.07465 \\ 0.05439 & 0.03084 & -1.42435 & 2.63947 & -0.68636 \\ -0.92460 & -0.40471 & 1.02875 & 0.54576 & 0.52058 \\ -0.56368 & 0.32921 & 0.30635 & 1.49714 & -0.02703 \\ -0.86898 & -0.25694 & 0.01845 & -0.09486 & 0.75186 \\ -0.63670 & -0.42672 & 0.52031 & -5.45061 & -0.17466 \\ 0.16700 & -0.23594 & -1.60840 & -0.81791 & 0.32277 \\ -1.18104 & 1.04333 & -1.05388 & 0.89926 & 0.14550 \end{bmatrix} \tag{B.8a}$$

$$\mathbf{W}^{(2)} = \begin{bmatrix} -0.93659 & -1.45464 & 1.92997 & -2.15939 & -3.02896 & 0.89216 \\ 1.62312 & -0.03785 & -5.40140 & -1.99825 & -0.96530 & \end{bmatrix} \tag{B.8b}$$

$$\mathbf{b}^{(1)} = \begin{bmatrix} -0.18182, -0.98923, -0.30406, -1.13953, \\ 0.76961, -0.91128, 1.35926, -1.14520, -6.30560, -0.49912, -0.58319 \end{bmatrix} \tag{B.8c}$$

$$\mathbf{b}^{(2)} = \begin{bmatrix} -0.13701 \end{bmatrix} \tag{B.8d}$$

References

Asbridge, J. R., Bame, S. J., and Strong, I. B. (1968). Outward Flow of Protons from the Earth's Bow Shock. *Journal of Geophysical Research*, **73(17):5777 – 5782.**

Baker, K. B. and Wing, S. (1989). A New Magnetic Coordinate System for Conjugate Studies at High Latitudes. *Journal of Geophysical Research*, **94:9139 – 9143.**

Barnes, A. (1970). Theory of generation of bow-shock-associated hydromagnetic waves in the upstream interplanetary medium. *Cosmic Electrodynamics*, **1:90 – 114.**

Bishop, C. M. (1995). *Neural Networks for Pattern Recognition*. **Oxford University Press, Oxford.**

Bol'shakova, O. V. and Troitskaya, V. (1968). Relation of the IMF direction to the system of stable oscillations. *Doklady Akademii Nauk (Proceedings of the Russian Academy of Sciences)*, **180:343 – 346.**

Bonifazi, C. and Moreno, G. (1981a). Reflected and Diffuse Ions Backstreaming From the Earth's Bow Shock 1. Basic Properties. *Journal of Geophysical Research*, **86(A6):4397 – 4404.**

Bonifazi, C. and Moreno, G. (1981b). Reflected and Diffuse Ions Backstreaming From the Earth's Bow Shock 2. Origin. *Journal of Geophysical Research*, **86(A6):4405 – 4413.**

Burgess, D. (1995). Collisionless Shocks. In Kivelson, M. G. and Russell, C. T., editors, *Introduction to Space Physics*, **pages 129 – 163. Cambridge University Press, Cambridge.**

Burton, R. K., Russell, C. T., and Chappell, C. R. (1970). The Alfvén Velocity in the Magnetosphere and Its Relationship to ELF Emissions. *Journal of Geophysical Research*, **75(28):5582 – 5586.**

Cairns, I. H. and Lyon, J. G. (1995). MHD simulations of the Earth's bow shock at low Mach numbers: Standoff distances. *Journal of Geophysical Research*, **100(A9):17173 – 17180.**

Chapman, S. (1957). Notes on the Solar Corona and the Terrestrial Ionosphere. *Smithsonian Contributions to Astrophysics*, **2(1):1 – 11.**

Chi, P. J., Russell, C. T., Bloom, R. M., and Singer, H. J. (1998). Solar wind control of ultralow-frequency wave activity at L = 3. *Journal of Geophysical Research*, **103(A12):29467 – 29477.**

Chugunova, O. M., Pilipenko, V. A., Engebretson, M., and Rodger, A. (2007). Statistical Relations between the Probability of Occurrence of Pc3–4 Pulsations at High Latitudes in the Antarctic Regions and the Solar Wind and IMF Parameters. *Geomagnetism and Aeronomy*, **47:219 – 229.**

Clausen, L. B. N., Yeoman, T. K., Fear, R. C., Behlke, R., Lucek, E. A., and Engebretson, M. J. (2009). First simultaneous measurements of waves generated at the bow shock in the solar wind, the magnetosphere and on the ground. *Annales Geophsicae*, **27:357 – 371.**

Engebretson, M. J., Zanetti, L. J., Potemra, T. A., and Acuna, M. H. (1986). Harmonically structured ULF pulsations observed by the AMPTE CCE magnetic field experiment. *Geophysical Research Letters*, **13(9):905 – 908.**

Eriksson, P. T. I., Blomberg, L. G., Schaefer, S., and Glassmeier, K. H. (2006). On the excitation of ULF waves by solar wind pressure enhancements. *Annales Geophsicae*, **24:3161 – 3172.**

Fairfield, D. H. (1969). Bow Shock Associated Waves Observed in the Far Upstream Interplanetary Medium. *Journal of Geophysical Research*, **74(14):3541 – 3553.**

Fausett, L. V. (1994). *Fundamentals of Neural Networks: Architectures, Algorithms, and Applications.* **Prentice-Hall, New Jersey.**

Fraser, B. J., Mcpherron, R. L., and Russell, C. T. (1988). Radial Alfvén velocity profiles in the magnetosphere and their relation to ULF wave field-line resonances. *Advances in Space Research*, **8(8):49 – 52.**

Fried, B. D. and Conte, S. D. (1961). *The Plasma Dispersion Function.* **Academic Press, New York.**

Fuselier, S. A. (1994). Suprathermal Ions Upstream and Downstream From the Earth's Bow Shock. In Engebretson, M. J., Takahashi, K., and Scholer, M., editors, *Geophysical Monograph: Solar wind sources of magnetospheric ultra-low frequency waves*, **pages 107 – 117. American Geophysical Union, Washington.**

Gary, S. P. (1991). Electromagnetic Ion/Ion Instabilities and their Consequences in Space Plasmas: A Review. *Space Science Reviews*, **56:373 – 415.**

Glassmeier, K.-H. (1984). On the influence of ionospheres with non-uniform conductivity distribution on hydromagnetic waves. *Journal of Geophysics*, **54:125 – 137.**

Greenstadt, E. W. and Olson, J. V. (1976). Pc3,4 activity and interplanetary field orientation. *Journal of Geophysical Research*, **81:5911.**

Grocott, A., Badman, S. V., Cowley, S. W. H., Milan, S. E., Nichols, J. D., and Yeoman, T. K. (2009). Magnetosonic Mach number dependence of the efficiency of reconnection between planetary and interplanetary magnetic fields. *Journal of Geophysical Research*, **114(A7):1 – 9.**

Haykin, S. (1994). *Neural Networks: A Comprehensive Foundation*. **Pearson Education, New York, 1st edition.**

Heilig, B., Lotz, S., Verö, J., Sutcliffe, P., Reda, J., Pajunpaä, K., and Raita, T. (2010). Empirically modelled Pc3 activity based on solar wind parameters. *Annales Geophysicae*, **28:1703–1722.**

Heilig, B., Lühr, H., and Rother, M. (2007). Comprehensive study of ULF upstream waves observed in the topside ionosphere by CHAMP and on the ground. *Annales Geophysicae*, **25:737 – 754.**

Hoppe, M. M., Russell, C. T., Frank, L. A., Eastman, T. E., and Greenstadt, E. W. (1981). Upstream Hydromagnetic Waves and Their Association with Backstreaming Ion Populations: ISEE 1 and 2 Observations. *Journal of Geophysical Research*, **86(A6):4471 – 4492.**

Hughes, W. J. (1994). Magnetospheric ULF Waves: A Tutorial with a Historical Perspective. In Engebretson, M. J., Takahashi, K., and Scholer, M., editors, *Geophysical Monograph: Solar wind sources of magnetospheric ultra-low frequency waves*, **pages 1 – 11. American Geophysical Union, Washington.**

Hughes, W. J. (1995). The Magnetopause, Magnetotail, and Magnetic Reconnection. In Kivelson, M. G. and Russell, C. T., editors, *Introduction to Space Physics*, **pages 227 – 285. Cambridge University Press, Cambridge.**

Hundhausen, A. J. (1972). *Coronal Expansion and Solar Wind*. **Springer-Verlag, Berlin.**

Hundhausen, A. J. (1995). The Solar Wind. In Kivelson, M. G. and Russell, C. T., editors, *Introduction to Space Physics*, **pages 91 – 128. Cambridge University Press, Cambridge.**

Hundhausen, A. J., Bame, S. J., Asbridge, J. R., and Sydoriak, S. J. (1970). Solar Wind Proton Properties: Vela 3 Observations from July 1965 to June 1967. *Journal of Geophysical Research*, **75(25):4643 – 4657.**

Jacobs, J. A., Kato, Y., Matushita, S., and Troitskaya, V. A. (1964). Classification of Geomagnetic Micropulsations. *Journal of Geophysical Research*, **69(1):180 – 181.**

Kepko, L. (2002). ULF waves in the solar wind as direct drivers of magnetospheric pulsations. *Geophysical Research Letters*, **29(8):10–13.**

Khan, H. and Cowley, S. W. H. (1999). Observations of the response time of high-latitude ionospheric convection to variations in the interplanetary magnetic field using EISCAT and IMP-8 data. *Annales Geophysicae*, **17:1306 – 1335.**

Kim, Y., Street, W. N., Russell, G. J., and Menczer, F. (2005). Customer Targeting: A Neural Network Approach Guided by Genetic Algorithms. *Management Science*, **51(2):264 – 276.**

Kivelson, M. G. (1995a). Physics of space plasmas. In Kivelson, M. G. and Russell, C. T., editors, *Introduction to Space Physics*, **pages 27 – 55. Cambridge University Press, Cambridge.**

Kivelson, M. G. (1995b). Pulsations and Magnetohydrodynamic Waves. In Kivelson, M. G. and Russell, C. T., editors, *Introduction to Space Physics*, **pages 330 – 353. Cambridge University Press, Cambridge.**

Kivelson, M. G. and Southwood, D. J. (1985). Resonant ULF waves: A new interpretation. *Geophysical Research Letters*, **12:49 – 52.**

Kovner, M. S. and Feldstein, Y. I. (1973). On solar wind interaction with the earth's magnetosphere. *Planetary and Space Science*, **21(2):1191 – 1211.**

Kovner, M. S., Lebedev, V. V., Plyasova-Bakunina, T. A., and Troitskaya, V. A. (1976). On the generation of low frequency waves in the solar wind in front of the bow shock. *Planet. Space Sci.*, **24:261 – 267.**

Krauss-Varban, D. and Omidi, N. (1991). Structure of Medium Mach Number Quasi-Parallel Shocks: Upstream and Downstream Waves. *Journal of Geophysical Research*, **96(A10):17715 – 17731.**

Krauss-Varban, D. and Omidi, N. (1993). Propagation Characteristics of Waves Upstream and Downstream of Quasi-Parallel Shocks. *Geophysical Research Letters*, **20(11):1007 – 1010.**

Lang, K. R. (2001). *The Cambridge Encyclopedia of the Sun*. **Cambridge University Press, Cambridge.**

Le, G., Chi, P. J., Goedecke, W., Russell, C. T., Szabo, A., Petrinec, S. M., Reeves, G. D., and Chun, F. K. (2000a). Magnetosphere on May 11, 1999, the Day the Solar Wind Almost Disappeared: II. Magnetic Pulsations in Space and on the Ground. *Geophysical Research Letters*, **27(14):2165 – 2168.**

Le, G. and Russell, C. T. (1992). A study of ULF wave foreshock morphology - II: spatial variation of ULF waves. *Planetary and Space Science*, **40(9):1215 – 1225.**

Le, G. and Russell, C. T. (1994). The Morphology of ULF Waves in the Earth's Foreshock. In Engebretson, M. J., Takahashi, K., and Scholer, M., editors, *Geophysical Monograph: Solar wind sources of magnetospheric ultra-low frequency waves*, **pages 87 – 98. American Geophysical Union, Washington.**

Le, G., Russell, C. T., and Petrinec, S. M. (2000b). The magnetosphere on May 11, 1999, the day the solar wind almost disappeared: I. Current systems. *Geophysical Research Letters*, **27(13):1827 – 1830.**

Levine, W. S. (1996). *The Control Handbook*. **CRC Press, Boca Raton.**

Limpert, E., Stahel, W., and Abbt, M. (2001). Log-normal Distributions across the Sciences: Keys and Clues. *BioScience*, **51(5):341 – 352.**

Mayaud, P. N. (1980). Derivation, Meaning and Use of Geomagnetic Indices. In *Geophysical Monograph 22*. **American Geophysical Union, Washington.**

McPherron, R. L. (2005). Magnetic Pulsations: Their Sources and Relation to Solar Wind and Geomagnetic Activity. *Surveys in Geophysics*, **26(5):545 – 592.**

Menk, F. W., Waters, C. L., and Fraser, B. J. (2000). Field line resonances and waveguide modes at low latitudes 1. Observations. *Journal of Geophysical Research*, **105(A4):7747 – 7761.**

Müller, B. and Reinhardt, J. (1996). *Neural Networks: An Introduction*. **Springer-Verlag, Berlin.**

Narita, Y., Glassmeier, K.-H., Fornaçon, K.-H., Richter, I., Schäfer, S., Motschmann, U., Dandouras, I., Rème, H., and Georgescu, E. (2006). Low-frequency wave characteristics in the upstream and downstream regime of the terrestrial bow shock. *Journal of Geophysical Research*, **111(A1):1 – 14.**

Ndiitwani, D. C. and Sutcliffe, P. R. (2009). The structure of low-latitude Pc3 pulsations observed by CHAMP and on the ground. *Annales Geophsicae*, **27:1267 – 1277.**

Omidi, N., O'Farrell, A., and Krauss-Varban, D. (1994). Sources of magnetosheath waves and turbulence. *Advances in Space Research*, **14(7):45 – 54.**

Onsager, T. G., Thomsen, M. F., Gosling, J. T., and Bame, S. J. (1990). Survey of Coherent Ion Reflection at the Quasi-Parallel Bow Shock. *Journal of Geophysical Research*, **95(A3):2261 – 2271.**

Parker, E. N. (1958). Dynamics of the Interplanetary Gas and Magnetic Fields. *Astrophysical Journal*, **128:664 – 676.**

Paschmann, G., Sckopke, N., Asbridge, J. R., Bame, S. J., and Gosling, J. T. (1980). Energization of Solar Wind Ions by Reflection From the Earth's Bow Shock. *Journal of Geophysical Research*, **85(A9):4689 – 4693.**

Peddie, N. W. (1982). International geomagnetic reference field: the third generation. *Journal of Geomagnetism and Geoelectricity*, **34:309–326.**

Plaschke, F., Glassmeier, K.-H., Sibeck, D. G., Auster, H. U., Constantinescu, O. D., Angelopoulos, V., and Magnes, W. (2009). Magnetopause surface oscillation frequencies at different solar wind conditions. *Annales Geophysicae*, **27:4521 – 4532.**

Potapov, A. S. and Mazur, V. A. (1994). Pc3 Pulsations: From the Source in the Upstream Region to Alfvén Resonances in the Magnetosphere. Theory and observations. In Engebretson, M. J., Takahashi, K., and Scholer, M., editors, *Geophysical Monograph: Solar wind sources of magnetospheric ultra-low frequency waves*, **pages 135 – 145. American Geophysical Union, Washington.**

Quest, K. B. (1988). Theory and Simulation of Collisionless Parallel Shocks. *Journal of Geophysical Research*, **93(A9):9649 – 9680.**

Rohwer, C. (2005). *Nonlinear Smoothing and Multiresolution Analysis*, **volume 150 of** *International Series ofNumerical Mathematics*. **Birkhäuser Verlag, Basel.**

Ross, S. (2002). *A First Course in Probability.* **Prentice-Hall, 6 edition.**

Russell, C. T. and Hoppe, M. M. (1981). The dependence of upstream wave periods on the interplanetary magneic field strength. *Geophysical Research Letters*, **8:615 – 617.**

Russell, C. T. and Hoppe, M. M. (1983). Upstream waves and particles. *Space Science Reviews*, **34:155 – 172.**

Saito, T. (1964). A new index of geomagnetic pulsation and its relation to solar M-regions. *Ionosph. Space Res.*, **18:260 – 274.**

Samson, J. C., Harrold, B. G., Rouhoniemi, J. M., Greenwald, R. A., and Walker, A. D. M. (1992). Field line resonances associated with MHD waveguides in the Earth's magnetosphere. *Geophysical Research Letters*, **19:441 – 444.**

Samson, J. C., Waters, C. L., Menk, F. W., and Fraser, B. J. (1995). Fine structure in the spectra of low latitude field line resonances. *Geophysical Research Letters*, **22(16):2111 – 2114.**

Scarf, F. L., Fredericks, R. W., Frank, L. A., Russell, C. T., Coleman, P. J., and Neugebauer, M. (1970). Direct Correlations of Large-Amplitude Waves with Suprathermal Protons in the Upstream Solar Wind. *Journal of Geophysical Research*, **75(34):7316 – 7322.**

Sciffer, M. D., Waters, C. L., and Menk, F. W. (2004). Propagation of ULF waves through the ionosphere: Inductive effect for oblique magnetic fields. *Annales Geophysicae*, **22:1155 – 1169.**

Shoji, M., Omura, Y., Tsurutani, B. T., Verkhoglyadova, O. P., and Lembege, B. (2009). Mirror instability and L-mode electromagnetic ion cyclotron instability: Competition in the Earth's magnetosheath. *Journal of Geophysical Research*, **114(A10):1 – 13.**

Sonnerup, B. U. Ö. (1969). Acceleration of Particles Reflected at a Shock Front. *Journal of Geophysical Research*, **74(5):1301 – 1304.**

Spiegel, M. R., Schiller, J. J., and Srinivasan, R. A. (2000). *Theory and Problems of Probability and Statistics.* **Schaum's Outline Series. McGraw-Hill, New York, 2 edition.**

Spreiter, J. R., Summers, A. L., and Alksne, A. Y. (1966). Hydromagnetic Flow Around the Magnetosphere. *Planetary and Space Science*, **14:223 – 253.**

Stephenson, J. A. E. and Walker, A. D. M. (2010). Coherence between radar observations of magnetospheric field line resonances and discrete oscillations in the solar wind. *Annales Geophysicae*, **28(1):47 – 59.**

Stewart, B. (1861). On the Great Magnetic Disturbance Which Extended from August 28 to September 7, 1859, as Recorded by Photography at the Kew Observatory. *Philosophical Transactions of the Royal Society of London*, **151:423 – 430.**

Sutcliffe, P. R. (1997). Substorm onset identification using neural networks and Pi2 pulsations. *Annales Geophsicae*, **15:1257 – 1264.**

Treumann, R. A. and Baumjohann, W. (1997a). *Advanced Space Plasma Physics*. **Imperial College Press, London.**

Treumann, R. A. and Baumjohann, W. (1997b). *Basic Space Plasma Physics*. **Imperial College Press, London.**

Troitskaya, V. A. (1994). Discoveries of Sources of Pc2–4 Waves – A Review of Research in the Former USSR. In Engebretson, M. J., Takahashi, K., and Scholer, M., editors, *Geophysical Monograph: Solar wind sources of magnetospheric ultra-low frequency waves*, **pages 45 – 54. American Geophysical Union, Washington.**

Troitskaya, V. A., Plyasova, T. A., and Gul'elmi, A. V. (1971). Relationship between Pc2–4 pulsations and the interplanetary field. *Doklady Akademii Nauk (Proceedings of the Russian Academy of Sciences)*, **197:1312.**

Usmanov, A. V. (2005). Low-density anomalies and sub-Alfvénic solar wind. *Journal of Geophysical Research*, **110(A1):1 – 11.**

Vellante, M., Lühr, H., Zhang, T., Wesztergom, V., Villante, U., De Lauretis, M., Piancatelli, A., Rother, M., Schwingenschuh, K., Koren, W., and Magnes, W. (2004). Ground/satellite signatures of field line resonance: A test of theoretical predictions. *Journal of Geophysical Research*, **109(A6):1 – 13.**

Walker, A. D. M. (2005). *Magnetohydrodynamic waves in geospace: The theory of ULF waves and their interaction with energetic particles in the solar-terrestrial environment*. **Institute of Physics publishing, Bristol.**

Walker, R. J. and Russell, C. T. (1995). Solar-Wind Interactions with Magnetized Planets. In Kivelson, M. G. and Russell, C. T., editors, *Introduction to Space Physics***, pages 164 – 181. Cambridge University Press, Cambridge.**

Waters, C. L., Menk, F. W., and Fraser, B. J. (1991). The resonance structure of low latitude Pc3 geomagnetic pulsations. *Geophysical Research Letters***, 18(12):2293–2296.**

Werbos, P. J. (1974). *Beyond Regression: New Tools for Prediction and Analysis in the Behavioural Sciences***. PhD thesis, Harvard University, Boston.**

Wolfe, A., Lanzerotti, L. J., and MacLennan, C. G. (1980). Dependence of Hydromagnetic Energy Spectra on Solar Wind Velocity and Interplanetary Magnetic Field Direction. *Journal of Geophysical Research***, 85(A1):114 – 118.**

Yumoto, K. (1985). Low Frequency Upstream Waves as a Probable Source of Low Latitude Pc3–4 Magnetic Pulsations. *Planetary and Space Science***, 33(2):239 – 249.**

Yumoto, K., Saito, T., Tsurutani, B. T., Smith, E. J., and Akasofu, S.-I. (1984). Relationship between the IMF Magnitude and Pc3 Magnetic Pulsations in the Magnetosphere. *Journal of Geophysical Research***, 89:9731 – 9740.**

Zell, A., Mamier, G. M., Vogt, M., Mache, N., Hübner, R., Döring, S., Herrmann, K.-U., Soyez, T., Schmalzl, M., Sommer, T., Hatzigeorgiou, A., Posselt, D., Schreiner, T., Kett, B., Clemente, G., Wieland, J., and Gatter, J. (1998). *Stuttgart Neural Network Simulator User Manual, Version 4.2.* **University of Stuttgart, University of Tübingen.** http://www.nada.kth.se/-orre/snns-manual/.